

High Frequency Sensing Mechanisms for Two-Dimensional Carrier Systems

Vom Promotionsausschuss der
Technischen Universität Hamburg
Zur Erlangung des akademischen Grades
Doktor-Ingenieur (Dr. -Ing.)
genehmigte Dissertation

von
Pai Zhao

aus
Liaoning, China

2020

- Vorsitz des Prüfungsausschuss: Prof. Matthias Kuhl
- 1. Gutacher: Prof. Hoc Khiem Trieu
- 2. Gutacher: Prof. Robert H. Blick
- Tag der mündlichen Prüfung: 14.02.2020

吾生也有涯，而知也无涯。以有涯随无涯，殆已！

庄周（约前 369 年至前 286 年）

Translation:

My life is limited, but knowledge is endless.

It will be dangerous to pursue endless knowledge within my limited life!

Zhuang Zhou (c. 369 BC – c. 286 BC)

My own little understanding....

The life is short, what I can do is limited,

Instead of being appealed by all events around,

I should focus on what I really like.

Abstract

Two-dimensional carrier systems, as found in III-V semiconductor heterostructures or monolayer graphene, are the ideal test bed for novel high-frequency sensing systems due to their high carrier mobility and sensitivity. The scope of this thesis is the study of microwave-induced excitation techniques such as electron spin or nuclear spin resonance methods (ESR, NMR), a mechanical excitation by surface acoustic waves (SAWs) or a combination of these methods.

Spin resonance techniques are based on a fundamental quantum mechanical property, i.e., the precession of the spin magnetic moment in an external magnetic field. When irradiated with microwaves of the frequency that matches the moment's energy, the spin can absorb the microwaves and performs a spin flip transition. This resonant absorption of microwave photons in the quantum world can be observed in the macroscopic world as changes in the longitudinal resistivity/conductivity of two-dimensional systems. This method is dubbed resistively detected electron (or nuclear) spin resonance (RD-ESR, RD-NMR).

The concept of mechanical excitation by surface acoustic waves (SAWs) is based on the piezoelectric properties of certain materials such as gallium arsenide (GaAs) or lithium niobate (LiNbO_3). Here, high frequencies are applied to metallic finger structures (interdigitated transducers, IDTs) that generate a periodic mechanical deformation that travels along the surface and drags along electrons. The resulting periodic strain and acoustoelectric current is seen in the sample's magnetoresistance, i.e., the resistance versus an external magnetic field. By combining SAWs magnetoresistance measurements with ESR/NMR, the system's sensory capabilities are tested.

For magnetotransport measurements on GaAs/AlGaAs heterostructures, multiple photolithography, etching and deposition steps are used to fabricate Hall bar mesas. The generation of SAWs requires complementary electron beam lithography to obtain IDTs. By releasing/suspending the thin layer of the GaAs that holds the two-dimensional carrier system in an etching process, the SAWs amplitudes increase along with its sensing sensitivity. In addition to conventional III-V semiconductor materials, a Hall bar consisting of monolayer graphene is constructed on a plain semi-insulating GaAs substrate with IDTs. The crucial steps for this material include transferring CVD-grown graphene sheets, lithography for the Hall bars, Ohmic contacts, and thermal annealing.

The proximity of electrons and nuclei that make up the semiconductor ensues interactions on a quantum mechanical scale. Electron spins are thus sensitive to both microwave radiation and the nuclear effects, here specifically to the magnetic moments of the nuclei. This electron-spin nuclear-spin hyperfine interaction is seen in the Overhauser shift as a large change in the ESR frequency due to dynamically polarized nuclear spins in the ESR process. In graphene, the electron spins are not exposed to such a nuclear field and the

resonant frequencies precisely follow a g -factor of 1.95 under a constant ac current. When SAWs are used to substitute the ac current by an acoustoelectric current, additional oscillating features in magnetotransport appear and a small shift in the ESR frequency is observable resulting from the periodic strain.

New solutions for mass sensing are proposed based on the fundamental studies of two-dimensional carrier systems.

Zusammenfassung

Zweidimensionale Ladungsträgersysteme, die u.a. in III/V Halbleiter-Heterostrukturen oder Graphen zu finden sind, sind infolge ihrer hohen Ladungsträgerbeweglichkeit und Sensitivität ideale Kandidaten zur Realisierung neuartiger Hochfrequenzmessmethoden. Diese Arbeit befasst sich mit der Untersuchung von Mikrowellenanregungstechniken wie der Elektronspinresonanz (ESR) oder Kernspinresonanz (NMR) sowie mechanischer Anregung mittels akustischer Oberflächenwellen (SAW) bzw. einer Kombination dieser Methoden.

Spinresonanzmethoden basieren auf einer elementaren quantenmechanischen Eigenschaft: der Präzession des magnetischen Spins in einem externen Magnetfeld. Durch Mikrowelleneinstrahlung mit einer Frequenz, die der Energie des magnetischen Moments im Magnetfeld entspricht, kann eine Spinumkehr erzeugt werden. Die resonante Absorption eines Mikrowellenphotons in der Quantenwelt lässt sich in der makroskopischen Welt als Änderung des elektrischen Widerstandes eines zweidimensionalen Ladungsträgersystems beobachten. Dieses Verfahren wird als widerstandsdetektierte Elektronspin (Kernspin-) Resonanz bezeichnet (RD-ESR, RD-NMR).

Mechanische Anregungen können durch akustische Oberflächenwellen (SAWs) erfolgen, deren Erzeugung auf den piezoelektrischen Eigenschaften bestimmter Materialien wie Galliumarsenid (GaAs) oder Lithiumniobat (LiNbO_3) basiert. Hierzu wird ein hochfrequentes Wechselfeld an metallische Fingerstrukturen (IDTs) angelegt, wodurch eine periodische, mechanische Deformation erzeugt wird, die sich wellenförmig entlang der Oberfläche ausbreitet. Die Oberflächenwellen transportieren Elektronen und der daraus resultierende akustische Strom ist beobachtbar im Magnetowiderstand der Probe, d.h. im Widerstandsverhalten bei Anwesenheit magnetischer Felder. Durch Kombination von SAW und ESR/NMR wird in dieser Arbeit die Einsatzmöglichkeit zweidimensionaler Ladungsträgersysteme für neuartige Hochfrequenzmessmethoden untersucht.

Um Magnetowiderstandsmessungen an GaAs/AlGaAs Heterostrukturen vorzunehmen, wurden zur Herstellung von Hall Bars diverse Fotolithographie-, Ätz- und Metallabscheidungsschritte verwendet. Ergänzend wurde Elektronenstrahllithographie eingesetzt, um IDTs anzufertigen, die für die Erzeugung von SAWs nötig sind. Mittels eines chemischen Ätzprozesses wurden dünne GaAs-Schichten abgelöst, die das zweidimensionale Ladungsträgersystem beherbergen. Die Ablösung dient zur Erhöhung der Amplitude und Messempfindlichkeit der akustischen Oberflächenwellen. Neben konventionellen III/V-Halbleitermaterialien wurde ebenfalls CVD-Graphen auf planarem, isolierenden GaAs Substraten mit IDTs untersucht. Die kritischen Prozessschritte sind hier der Transfer des Graphens, die darauffolgende Lithographie zur Erzeugung einer Hall Bar, der Ohm'schen Kontakte und das Tempern.

Der quantenmechanische Überlapp zwischen Elektronenwellenfunktionen und Kernen, die den Halbleiterkristall bilden, hat Wechselwirkungseffekte zur Folge. Der Elektronspin reagiert daher nicht nur auf Mikrowellenstrahlung, sondern auch auf das magnetische Moment der Kernspins. Diese Elektronspin-Kernspin-Hyperfein Wechselwirkung lässt sich bei tiefen Temperaturen als Verschiebung der ESR Frequenz (Overhauser Shift) beobachten. Die Verschiebung entsteht z.B. durch Polarisierung der Kerne während der resonanten Absorption während der ESR.

In Graphen ist der Elektronenspin diesen Wechselwirkungen mit den Kernen nicht ausgesetzt, und die Resonanzfrequenz folgt exakt einem g -Faktor vom 1.95, wenn der Magnetowiderstand bei konstanten Wechselströmen gemessen wird. Werden SAW genutzt, um den Wechselstrom durch einen akustischen Strom zu ersetzen, treten zusätzliche Merkmale im Magnetowiderstand auf und eine minimale Verschiebung der ESR Frequenz ist beobachtbar, die vermutlich auf die mechanische Deformation zurückzuführen ist.

Basierend auf den Untersuchungen zweidimensionaler Ladungsträgersystemen in dieser Arbeit, werden neuartige Ansätze zur Massenspektroskopie vorgeschlagen.

Contents

Abstract	i
Zusammenfassung	iii
Abbreviations.....	vii
Chapter 1 Introduction	1
Chapter 2 Physics of Two-Dimensional Electron Systems Excited by Surface Acoustic Waves in the Quantum Hall Regime.....	5
2.1 Two-Dimensional Systems	6
2.2 Quantum Well	8
2.3 Classical Magnetotransport	11
2.4 Integer Quantum Hall Effect	13
2.5 Electron Spin Resonance and Nuclear Spin Resonance	21
2.6 Monolayer Graphene Two-Dimensional Systems.....	28
2.7 Suspended 2D Nano-Electromechanical Systems.....	35
2.8 Surface Acoustic Waves and Two-Dimensional Electron Systems.....	39
Chapter 3 Sample Fabrication	47
3.1 Hall Bar Structures in GaAs/AlGaAs Heterostructures.....	47
3.2 Hall Bar Structures in Monolayer Graphene	53
3.3 Interdigitated Transducers (IDTs).....	56
Chapter 4 Measurement Infrastructure.....	59
4.1 Experimental Setup	59
4.2 Cryogenic Systems.....	67
4.3 Probe Design	70
Chapter 5 Sample Characterization and Measurements	73
5.1 Characterization of GaAs/AlGaAs Heterostructures	73
5.2 Electron Spin Resonance in GaAs/AlGaAs Heterostructures	77

5.3 Surface Acoustic Wave Induced Currents in a Two-Dimensional Electron System	91
5.4 Characterization of Graphene on a GaAs Substrate	94
5.5 Electron Spin Resonance in Monolayer Graphene	97
5.6 Surface Acoustic Wave Interaction with Graphene	100
Chapter 6 Conclusion and Outlook	111
6.1 Summary	111
6.2 Outlook	112
Appendix.....	115
Bibliography	125
Publication	135
Acknowledgement	137

Abbreviations:

2DES	two-dimensional electron system
AC	alternating current
AFM	atomic force microscopy
CVD	chemical vapor deposition
DI	deionized
DOS	density of states
EBL	electron beam lithography
ESR	electron spin resonance
GPIB	general purpose interface bus
HF	hydrofluoric acid
IDT	interdigitated transducer
MBE	molecular-beam epitaxy
MOCVD	metal-organic chemical vapor deposition
NMR	nuclear magnetic resonance
PMMA	poly(methyl methacrylate)
PTFE	polytetrafluoroethylene
PVD	physical vapor deposition
RIE	reactive ion etching
RD-ESR	resistively-detected electron spin resonance
RD-NMR	resistively-detected nuclear magnetic resonance
SEM	scanning electron microscopy

Chapter 1

Introduction

In 1879, Edwin Herbert Hall discovered the emergence of a voltage difference across an electrical conductor transversal to the current direction when a perpendicular magnetic field is applied [E.HAL1879]. Six years later, in 1885, Lord Rayleigh demonstrated the motion of an acoustic wave (also known Rayleigh wave) along the surface of a solid [L.RAY1885]. Almost to the centenary of the discovery of the ordinary Hall effect by Edwin H. Hall, the integer quantum Hall effect was discovered in a two-dimensional electron system in 1980 by Klaus von Klitzing [K.KLI1980]. The invention of interdigitated transducers, IDTs, in the 1960s [R.WHI1965] triggered a synergy between Hall effects and surface acoustic waves which has substantially contributed to understanding of the transport behavior of charged carriers in low-dimensional semiconductors. In 1986, also coincidentally to the centenary of the discovery of surface acoustic waves, Achim Wixforth published his work on the surface acoustic wave attenuation in the quantum Hall regime, demonstrating that electrons in a two dimensional systems can move with the speed of sound $\sim 10^3 \text{ms}^{-1}$ instead of the Fermi velocity [A.WIX1986].

When restricting the motional degree of freedom in one direction, the electron energies will be quantized to discrete levels in the direction of the confinement while a continuous energy spectrum in the other directions is preserved. This was an important prerequisite for the discovery of the quantum Hall effect. The motion of an electron that interacts with phonons, photons or other electrons determines the macroscopic behavior of the system, i.e., its resistance or conductance. In a strong perpendicular magnetic field, the kinetic energy of 2D electrons will further quantize into a set of discrete levels. These Landau levels are separated by the cyclotron energy and at sufficiently large fields additionally by the Zeeman energy which represents the two electron spin degrees of freedom.

Microwave excitations can be used control and study the spin state of a two-dimensional electron system in the quantum Hall regime when the microwave energy $h\nu$ matches the Zeeman splitting ΔE_Z . The resulting spin flips are detectable on a macroscopic scale as changes in longitudinal conductance of the sample. Similar to the example of microwave absorption, surface acoustic waves generated on piezoelectric materials in contact with the two-dimensional system can be used to control and study its electrical properties.

Surface acoustic waves have two main effects: *strain* through the surface deformation and the emergence of an *acoustoelectric current*. Contrary to a conventional current consisting of electrons moving with Fermi velocity, surface acoustic waves can manipulate electrons with the speed of sound, generating the *acoustoelectric current*. It is the result of an alternating electric field and the lattice acoustic phonon interaction with the electrons.

This work is dedicated to the study of various sensing mechanisms for two-dimensional carrier systems. I will begin by outlining the underlying physics, such as the band structure of a GaAs heterostructure or monolayer graphene, the integer quantum Hall effects, electron spin resonance and surface acoustic waves. I will introduce crucial processing steps as well as the measurement infrastructure. I will explain the sample structures, the cryostats' probe station and various measurement setups and methodologies.

The measurements on GaAs/AlGaAs heterostructures show a distinct hysteresis of the electron spin resonance, demonstrating the influence of the nuclear polarization. The study of surface acoustic waves of 2D carriers in graphene demonstrates the impact of strain and acoustoelectric current on the electron spin resonance.

Various novel applications can be envisioned by combining the sensing mechanisms studied in this thesis. A sensitive mass detection scheme using a freestanding membrane is proposed based on surface acoustic waves and electronic transport studies.

The framework of this thesis is organized as follows:

- Chapter 2, *Physics of two-dimensional electron systems excited by surface acoustic waves in the quantum Hall regime*, describes the physical concepts used in this work, i.e., two-dimensional electron systems (2DES) in conventional III-V semiconducting materials and monolayer graphene, integer quantum Hall effects, electron spin resonance (ESR), epitaxy liftoff (ELO) and surface acoustic waves (SAWs).
- Chapter 3, *Sample fabrication*, outlines the processing steps for various sample types. Starting with a normal Hall bar structure on a III-V semiconductor, I will describe all crucial standard processing steps, i.e., mask design, optical lithography and physical vapor deposition (PVD). I will implement electron beam lithography (EBL) to fabricate interdigitated transducers to generate acoustoelectric currents, which are used as an alternative to conventional currents in magnetotransport studies. I will explain the method of releasing a structure with hydrofluoric acid to fabricate freestanding membranes. Finally, I will introduce the processing steps for fabricating Graphene Hall bars on piezoelectric substrates that are excited by surface acoustic waves.
- Chapter 4, *Measurement infrastructure*, explains the low temperature facilities and the equipment to perform characterizations and measurements. I will discuss the cryogenic superconducting magnet system to cool down and measure the samples in strong perpendicular magnetic fields. I will present a home-build probe, installed with components for low and high frequency signal transmission.
- Chapter 5, *Sample characterization and measurements*, summarizes the most relevant measurements. This chapter is divided into two main parts, starting with the measurements on GaAs semiconductor heterostructures and followed by the studies of CVD monolayer Graphene. Both parts begin with sample test and characterization. Using standard magnetotransport, carrier density and mobility are

deduced that allow the determination of the magnetic field positions of the various filling factors. In GaAs heterostructures, the impact hyperfine interaction and nuclear polarization as well as the use of nuclear magnetic resonance (NMR) on ESR is studied. In Graphene, I will present the application of a current driven by SAWs to study electron spin resonance.

- Chapter 6, *Conclusion and Outlook*, gives a summary of the results on electron spin resonance in GaAs/AlGaAs heterostructures and SAW-ESR in monolayer graphene. In the second half, I will provide an outlook for potential applications using the results of my thesis: Molecular detection can be achieved by monitoring the shift of the resonance frequency of a freestanding membrane/resonator, excited by surface acoustic waves, or by studying the electric transport of a freestanding membrane under strain.
- The Appendix provides detailed information about all materials and samples processed in this work as well as sample processing parameters.

Chapter 2

Physics of Two-Dimensional Electron Systems Excited by Surface Acoustic Waves in the Quantum Hall Regime

In this chapter, an introduction to two-dimensional electron systems (2DES) is given, followed by an introduction to the physics of the integer quantum Hall effects, which arise in 2DESs at low temperatures and under strong perpendicular magnetic fields. The integer quantum Hall effects results from the quantization of the electron energies in a magnetic field and the lifting of the spin degeneracy due to the Zeeman energy [K.KLI1986].

The magnetoresistance of a 2DES is sensitive to electromagnetic wave radiation with frequencies that match the Zeeman splitting between electrons of opposite spins [D.STEI1983, D.STEI1984, M.DOB1988]. In semiconducting heterostructures, hyperfine interaction between electron spins and nuclear spins can modify these resonance frequencies. Thus, resonant absorption between spin split Landau levels (electron spin resonance, ESR) allows to study and control fundamental quantum properties.

Besides the conventional 2DES in quantum well heterostructures, transport in graphene—a two dimensional sheet of carbon atoms—is also discussed for its unique lattice and band structure. With the above understanding, I will make a comparison between effects observed in suspended Hall bars and in conventional non-suspended structures. Finally, I will discuss the basics about surface acoustic waves, SAWs, and how to make use of acoustoelectric current induced by SAWs.

2.1 Two-Dimensional Systems

GaAs/AlGaAs heterostructures can be grown with high quality to reduce electron scattering and to achieve record carrier mobilities. The lattice constant of $\text{Al}_x\text{Ga}_{1-x}\text{As}$ alloys is a function of the aluminum content x according to Vegards law [L.VEG1921] as shown in figure 2.1.1 with less than 0.15% deviation to allow pseudomorphic (relaxed) growth.

Epitaxial growth methods such as molecular-beam epitaxy (MBE) and metal-organic chemical vapor deposition (MOCVD) in general meet those particular high requirements for sample quality, i.e., the growth of materials with similar lattice constants, fewer contaminations and defects on the interface. In this thesis, sample materials were grown by MBE in the group of Prof. Wolfgang Hansen and Dr. Christian Heyn at the CHyN and Prof. Werner Wegscheider from the ETH in Zurich/Switzerland. In MBE, which operates under an ultra-high vacuum better than 10^{-11} mbar, the mean free path of molecules between collisions is larger than the width of chamber (Knudsen number $\text{Kn} > 0.5$, [PFEIFFER]). The elements composing the heterostructure materials in the K-cells furnaces are vaporized to form a molecular beam which travels in straight ballistic lines towards a heated substrate. The crystal growth can be controlled precisely within single atomic layer by shutters in front of the K-cells and the temperature of furnaces with the reflected high-energy electron diffraction (RHEED) measuring monolayer growth. N-Type doping can be achieved using silicon in additional cells. Disadvantages of MBE are high costs and slow process for large scale production. MOCVD is faster and scaled up for commercial production at the expense of lower sample quality like a stagnant boundary layer and poisonous group-V hydrides [J.DAV1998].

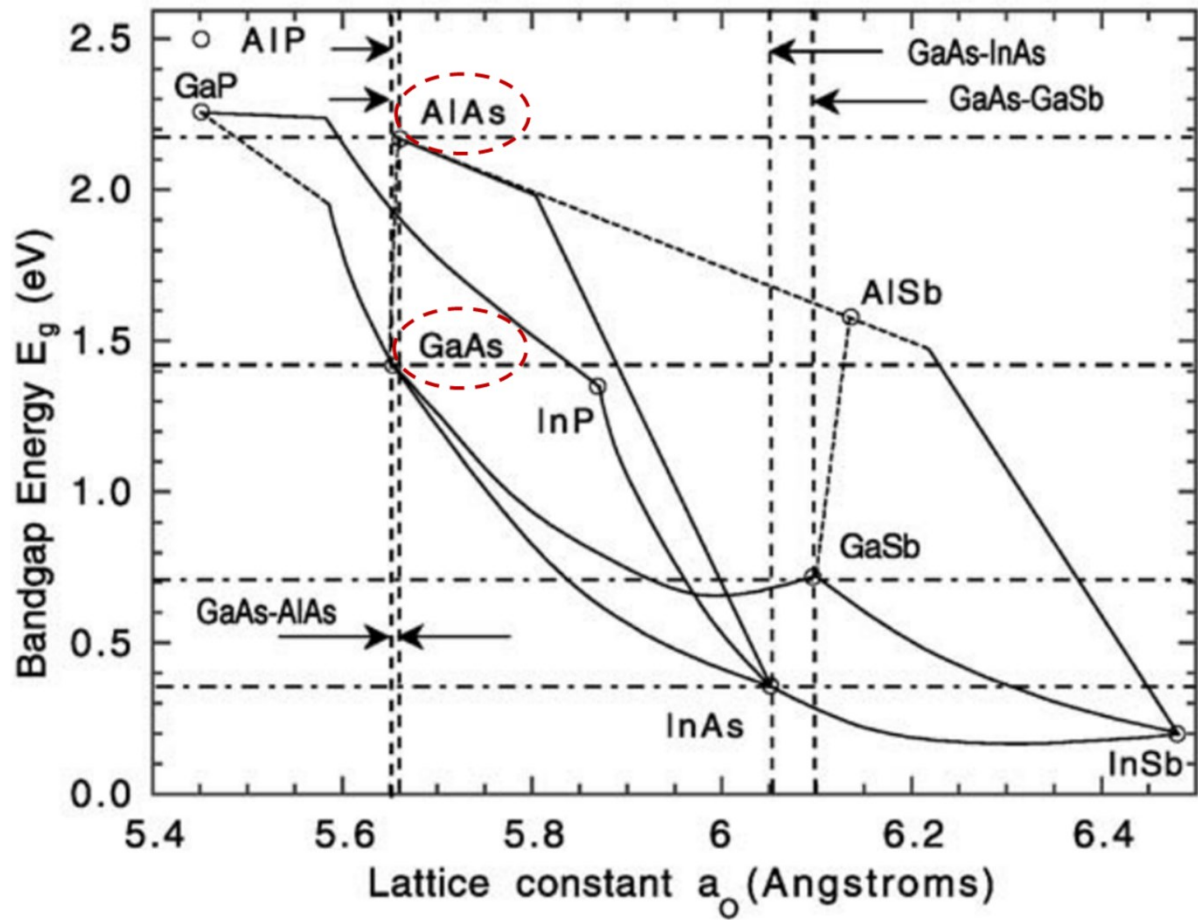


Figure 2.1.1 Plot of the bandgap energy E_g against lattice constant a_0 for several III-V semiconductor heterostructures at room temperature. The lattice constants for AlGaAs compounds are comparable [A.OWE2004].

2.2 Quantum Well

This thesis focuses on 2DESs formed in GaAs/AlGaAs heterostructures consisting of a thin layer of GaAs sandwiched between two AlGaAs barrier layers with higher conduction band energy than the well as seen in figure 2.2.1. The electrons are confined in the well layer perpendicular to the growth direction. Consequently, in the conduction band, the band energy is quantized to discrete levels [M.KEL1995, C.CO2005],

$$E_{z(i)} = E_0 + \frac{\pi^2 \hbar^2 i^2}{2m^* w^2} \quad i \in (1, 2, 3, \dots) \quad 2.2.1$$

with E_0 being the bottom of the conduction band energy in bulk GaAs, m^* being the effective electron mass in the conduction band, w being the quantum well width and i being an integer number. The spacing of the sub-bands with index i is determined by the thickness of the width of the well. When dealing with a realistic quantum well with a finite barrier height, the wave function partially penetrates into the barrier. In magnetotransport measurements, the occupation of lowest sub-band is preferred as inter-sub-band scattering can happen with higher sub-band occupation.

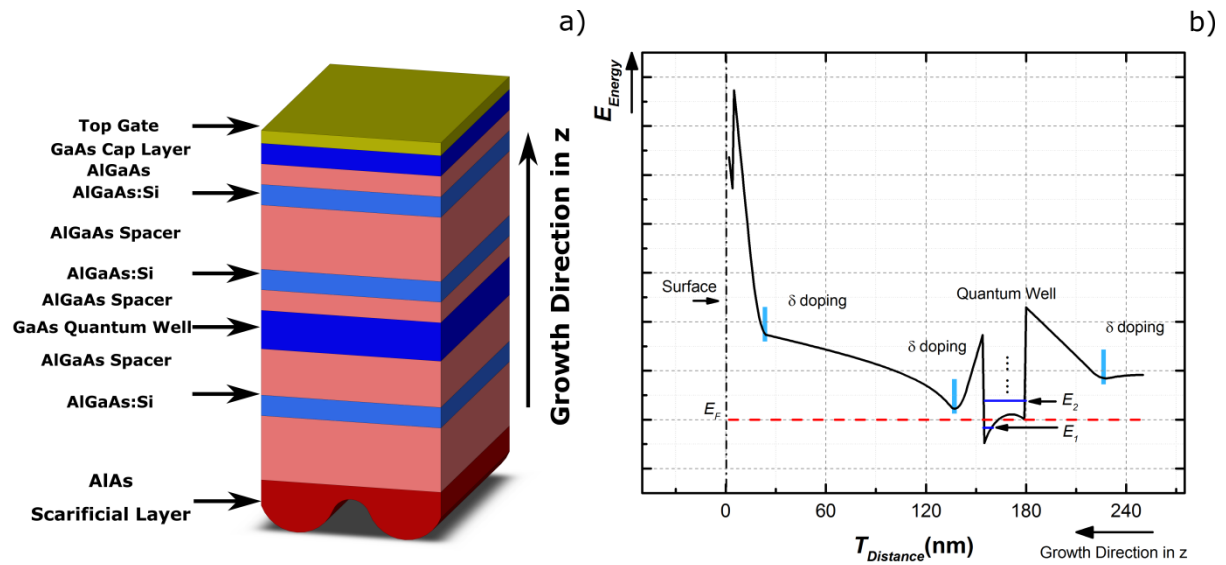


Figure 2.2.1 a) Schematics of a single quantum well with modulation doping, b) Conduction band of the quantum well in the direction of growth direction with the lowest sub-band occupied [GREGO.SNIDE].

Density of States

In a 2DES with parabolic energy dispersion in **K**-space as seen in figure 2.2.2 a), the density of states, DOS, i.e., the numbers of energy states per unit area per unit energy, can be calculated [M.KEL1995].

$$n_{2D}(E) = \frac{m^*}{\pi\hbar^2} \quad 2.2.2$$

We can see that it is dependent only on the effective mass of the electrons and particularly energy-independent. Together with the quantized energy level, the number of states in a given energy is a step function of energy

$$D_{2D}(E) = \frac{m^*}{\pi\hbar^2} \theta(E_{z(i)} - E_0) \quad 2.2.3$$

The hatched area in figure 2.2.2 b) shows the number of occupied states in the lowest sub-band up to the Fermi energy E_F . In a magnetic field, the DOS splits into a set of highly degenerate and discrete energy (Landau) levels.

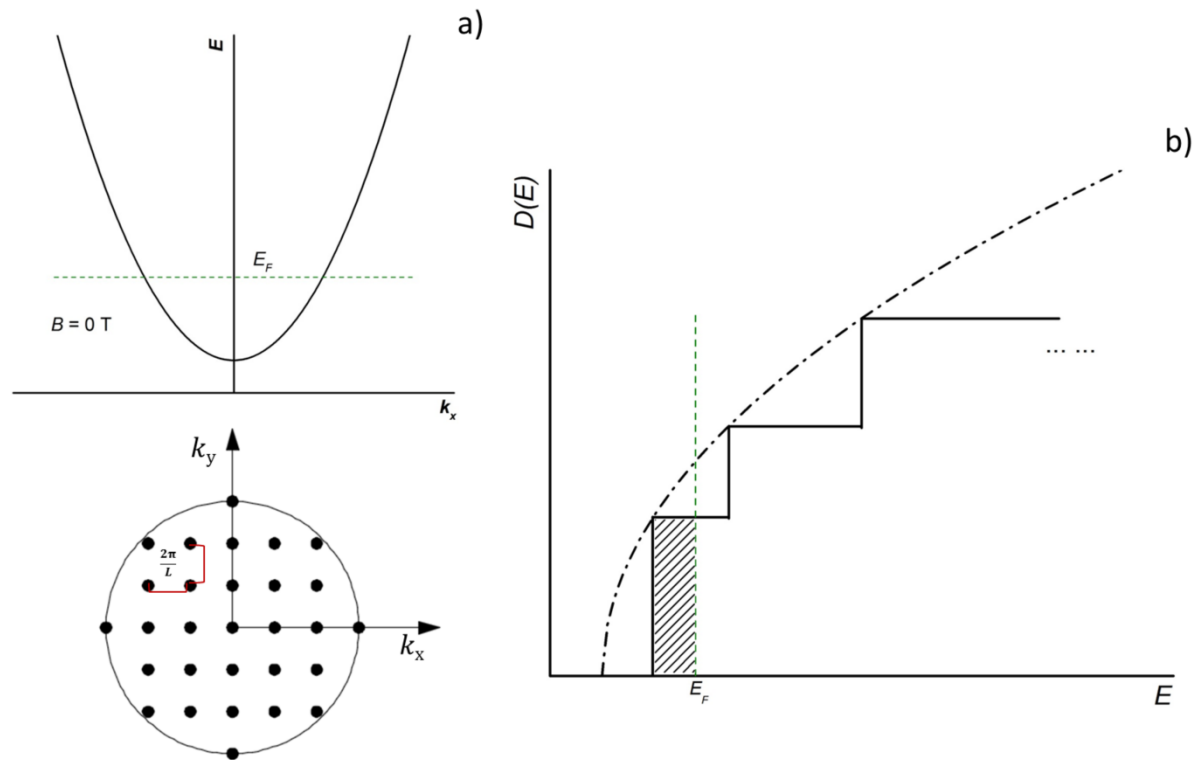


Figure 2.2.2 Magnetic field B is 0 Tesla. a) The parabolic distribution of energy spectrum in **K**-space with points (states) with (k_x, k_y) as axes, b) Density of States in 2DES (dot dash line shows the 3D case) with occupied states up to the Fermi energy E_F . Only the lowest sub-band of the quantum well is occupied.

Doping

Since at low temperature, pure GaAs becomes insulating, doping is used to achieve a finite conductivity even near absolute zero temperature. In modulation doping (invented and implemented at Bell laboratories by Willy Wiegmann, Art Gossard, Horst Stormer and Ray Dingle [H.STO1999]), the doping site is separated from the quantum well to reduce electron scattering on the ionized dopants and thus to achieve a higher carrier mobility. The electron density in modulation doping depends both on the doping concentration and the distance between doping layer and the quantum well (usually called spacer thickness). A higher carrier density can be achieved by increasing the doping concentration. However, strong doping can lead to a parasitic parallel conducting channel nearby the quantum well.

2.3 Classical Magnetotransport

We start discussing electron transport using a semi-classical approach. Figure 2.3.1 shows the commonly used Hall bar geometry. A magnetic field is applied in a perpendicular direction with respect to the plane coordinates x-y, a constant current I_{xx} is applied, flowing from the source contact (C1) to the drain contact (C2). A longitudinal voltage is measured between contacts C3 and C4 and a transverse Hall voltage can be measured between contacts C3 and C5.

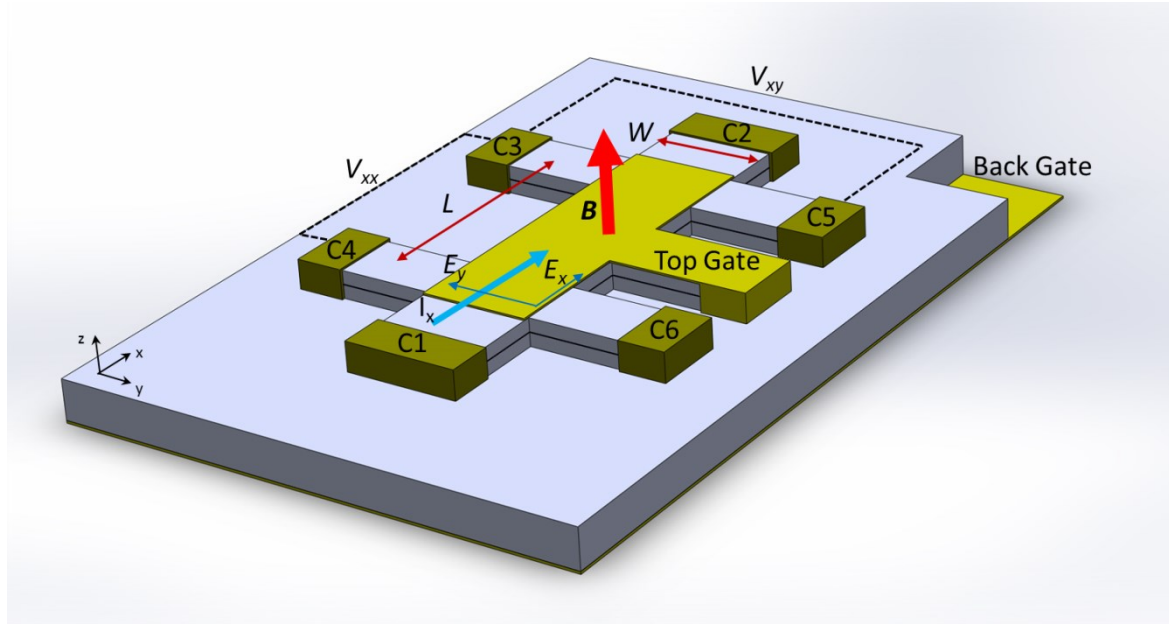


Figure 2.3.1 The Hall bar geometry used in the thesis. Contacts 1 and 2 act as source and drain (ground) contacts for the constant current. Voltages are measured in a four-point geometry, with different contacts than source and drain.

In the derivation of the Drude model [P.DRU1900I, P.DRU1900II], electrons are treated as point like particles with mass, which move under repeated scattering in an isotropic medium in a constant electric field E_x (no magnetic field). Electron-electron interactions are neglected. In a steady state with $dv/dt = 0$, the following balanced condition is achieved

$$\vec{v}_D = -\frac{e\tau}{m^*} \cdot \vec{E} = -\mu \cdot \vec{E} \quad 2.3.1$$

where v_D is the electron drift velocity. The electron mobility, $\mu \equiv e\tau/m^*$, is proportional to the scattering time τ and directly relates the drift velocity of charged carriers to the electric field. With modern epitaxy technologies, carriers mobilities up to $10^7 \text{ cm}^2\text{V}^{-1}\text{s}^{-1}$ can be achieved [V.UMA2009]. Using the previous definition for the drift velocity, the current density, \vec{j} , can be written as

$$\vec{j} = \frac{n_e e^2 \tau}{m^*} \vec{E} \quad 2.3.2$$

The factor $n_e e^2 \tau / m^*$ represents the Drude conductivity σ_0 . As shown below, electron mobility and carrier density can easily be obtained by measuring the longitudinal voltage at zero magnetic field and the Hall voltage at a finite magnetic field.

When a magnetic field is turned on, the Lorentz force adds a perpendicular component to the forwards movement of the carriers, which modifies equation 2.3.1 as follows

$$\frac{m^*}{\tau} \vec{v}_D = -e \left\{ \vec{E} + \underbrace{(\vec{v}_D \times \vec{B})}_{\text{magnetic force component}} \right\} \quad 2.3.3$$

As a result of the Lorentz force and the appearance of a Hall field, E_y , the conductivity cannot be treated as a simple factor that relates drift velocity to the electric field. When a magnetic field is applied, the current density, the electric field and the conductivity depend on the direction. The corresponding current density is thus expressed as

$$\begin{pmatrix} j_x \\ j_y \end{pmatrix} = \hat{\sigma} \begin{pmatrix} E_x \\ E_y \end{pmatrix} \quad 2.3.4$$

The first component, the conductivity, $\hat{\sigma}$, has the following form

$$\hat{\sigma} = \begin{pmatrix} \sigma_{xx} & \sigma_{xy} \\ -\sigma_{xy} & \sigma_{xx} \end{pmatrix} = \frac{\sigma_0^2}{1 + \omega_c^2 \tau_0^2} \begin{pmatrix} 1/\sigma_0 & -B/n_e e \\ B/n_e e & 1/\sigma_0 \end{pmatrix} \quad 2.3.5$$

where $\omega_c = eB/m^*$ is the cyclotron frequency. Its relationship with resistivity is

$$\hat{\sigma} = \frac{1}{\hat{\rho}} = \frac{1}{\rho_{xx}^2 + \rho_{xy}^2} \begin{pmatrix} \rho_{xx} & -\rho_{xy} \\ \rho_{xy} & \rho_{xx} \end{pmatrix} \quad 2.3.6$$

The resistivity components ρ_{xx} and ρ_{xy} can be obtained from the measured resistance R_{xx} and R_{xy}

$$R_{xx} = \frac{V_{xx}}{I_{SD}} = \frac{E_x L}{j_x W} = \frac{1}{ne\mu} \frac{L}{W} = \rho_{xx} \frac{L}{W} \quad 2.3.7$$

And

$$R_{xy} = \frac{V_{xy}}{I_{SD}} = \frac{E_y W}{j_x W} = \frac{B}{n_e e} = \rho_{xy} \quad 2.3.8$$

W denotes the width of the Hall bar, and L is the distance between the two contacts used for longitudinal measurements as seen in figure 2.3.1.

2.4 Integer Quantum Hall Effect

At very low temperatures, the Hall resistance at certain magnetic fields becomes a function of natural constants and is independent of geometry and materials [K.KLI1980]

$$R_{xy} = \frac{1}{\nu} \frac{h}{e^2} = \frac{1}{\nu} R_K \quad \nu \in \{1, 2, 3, \dots\} \quad 2.4.1$$

where ν is defined as the filling factor discussed later, and R_K the von-Klitzing constant. Since the relative accuracy of the measurement can reach up to 10^{-9} , the quantized Hall resistance can be used as a resistance standard. Figure 2.4.1 shows the longitudinal and Hall resistance as a function of an external magnetic field [M.CAG1985]. Above approximately 0.5 T, the longitudinal resistance deviates from the constant value as predicted by the classical Drude model and oscillations appear, which are called Shubnikov-de Haas (SdH) oscillations. At larger magnetic field, plateaus in the Hall curve become discernable.

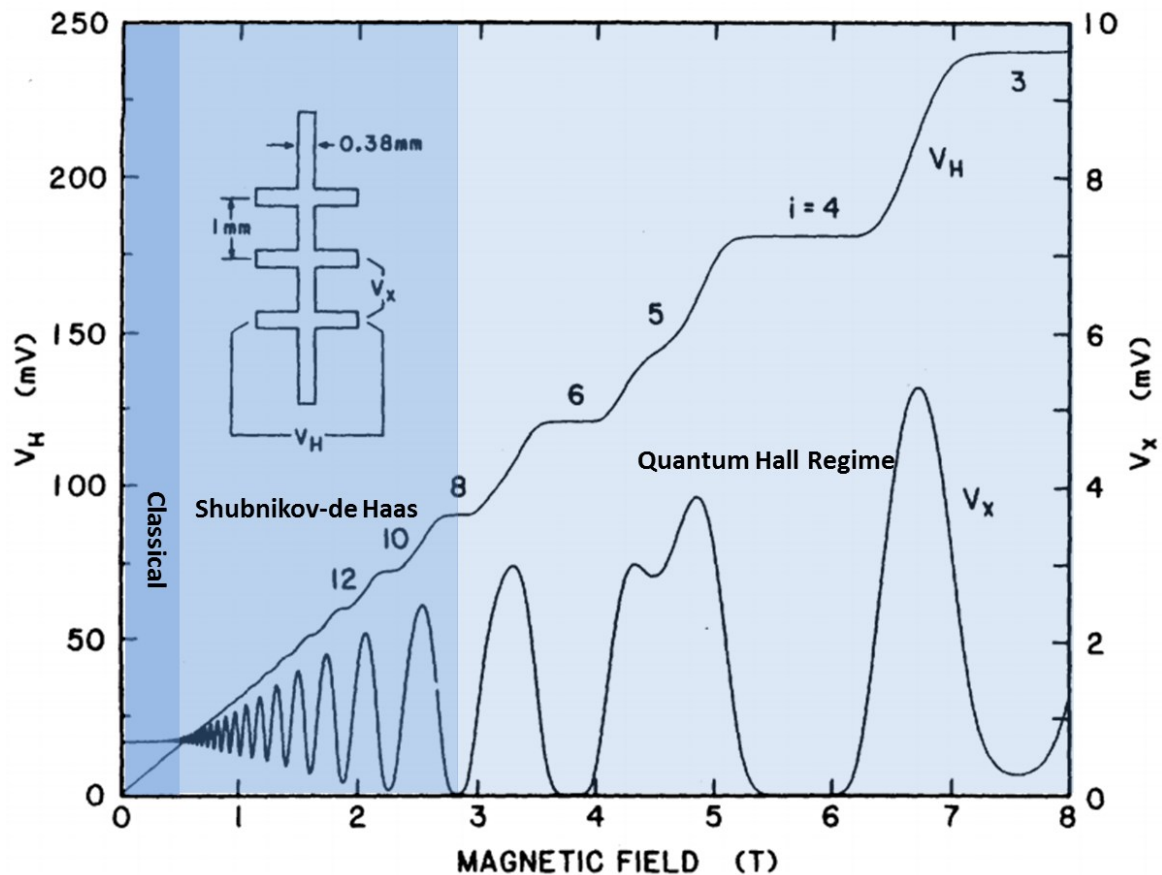


Figure 2.4.1 The integer quantum Hall effect. The longitudinal resistance shows the Shubnikov-de Haas oscillations with a $1/B$ period. In the quantum Hall regime, the vanished longitudinal resistance is accompanied by a plateau in the Hall resistance [M.CAG1985].

At low magnetic field with $\omega_c \tau \ll 1$, electrons scatter before they can complete an orbit. In this case, the system can be described by a semi-classical transport model. Once $\omega_c \tau \gg 1$ is fulfilled, the electrons are able to complete at least one full orbit before they scatter. In this regime, quantum effects begin to dominate because the electronic wave function can interface with itself. Here, a quantum mechanical model is required [C.CO2005, R.LAU1982].

Landau Quantization

Charged carriers in a magnetic field can be described by a time-independent Schrödinger equation [J.DAV1998, G.GIU2005], the magnetic field is expressed by a vector potential \mathbf{A}

$$\hat{H} \cdot \psi(x, y, z) = \left[\frac{1}{2m^*} (\hat{\mathbf{p}} - e\vec{A}(x, y, z))^2 + e\phi(x, y, z) \right] \psi(x, y, z) = \vec{E} \cdot \psi(x, y, z) \quad 2.4.2$$

with $\hat{\mathbf{p}}$ the momentum operator and ϕ the electrostatic confinement potential. Using the Landau gauge with vector potential $\mathbf{A} = (0, -B \cdot x, 0)$, the electrostatic potential will vanish under no external electric field. The Hamiltonian can be separated easily using a homogeneous magnetic field

$$H = \underbrace{\frac{p_z^2}{2m^*}}_{H_{//}(z)} + \underbrace{\frac{1}{2m^*} [p_x^2 + (p_y + eBx)^2]}_{H_{\perp}(z)} \quad 2.4.3$$

We can see that the motion of electrons can be separated into two components, i.e., one along z-direction and one in the x-y plane, respectively. In a quantum well, the motion of electrons is confined within its boundaries, giving rise to the energy quantization of Equation 2.2.1. The motion in the plane can be represented by a plane wave centered at $x_0 = l_B^2 k_m$ and extending in y-direction with the following eigenfunction

$$\psi_{n,m}(x, y) = \frac{1}{\sqrt{2^n n!} \sqrt{\pi} l_B} H_n \left(\frac{x - l_B^2 k_m}{l_B} \right) e^{-\frac{(x - l_B^2 k_m)^2}{2l_B^2}} e^{ik_m y} \quad 2.4.4$$

with $l_B = (\hbar/eB)^{1/2}$ the magnetic length, $k_m = 2\pi m/L_y$ with integer m and L_y the sample size in y direction. By solving the Schrödinger equation with these eigenfunctions, the electronic energy spectrum becomes quantized and is described by

$$E_j = \hbar \omega_c \left(j + \frac{1}{2} \right) \quad j \in (0, 1, 2, \dots) \quad 2.4.5$$

with the cyclotron frequency, ω_c , the energy spectrum is reduced to discrete values separated by $\Delta E_c = \hbar \omega_c$. These discrete energy values are referred to as Landau levels. In the previous definition, the energies are spin-degenerate because the electron spin is ignored.

Filling Factors

The Landau levels energies of equation 2.4.5 are deduced by assuming a center coordinate x_0 . However, since electrons at different coordinates can possess the same energy, we obtain a degeneracy by dividing the same length with the distance between two consecutive center coordinates

$$N_L = \frac{L_y}{\Delta x_0} = \frac{L_x L_y}{2\pi l_B^2} = L_x L_y B \frac{e}{h} = \frac{\Phi}{\Phi_0} \quad 2.4.6$$

The degeneracy of the Landau levels (or more precisely, the density of states, DOS) is equal to the number of flux quanta $\Phi_0 = h/e$ penetrating the 2DES as a function of magnetic field.

In a perpendicular magnetic field, the density of states, DOS, degenerates into delta function separated by $\hbar\omega_c$ as seen in figure 2.4.2

$$D_{2D}(E) = n_L \sum \delta(E - E_j) \quad 2.4.7$$

with n_L being $n_L/L_x L_y$, the number of states per unit area.

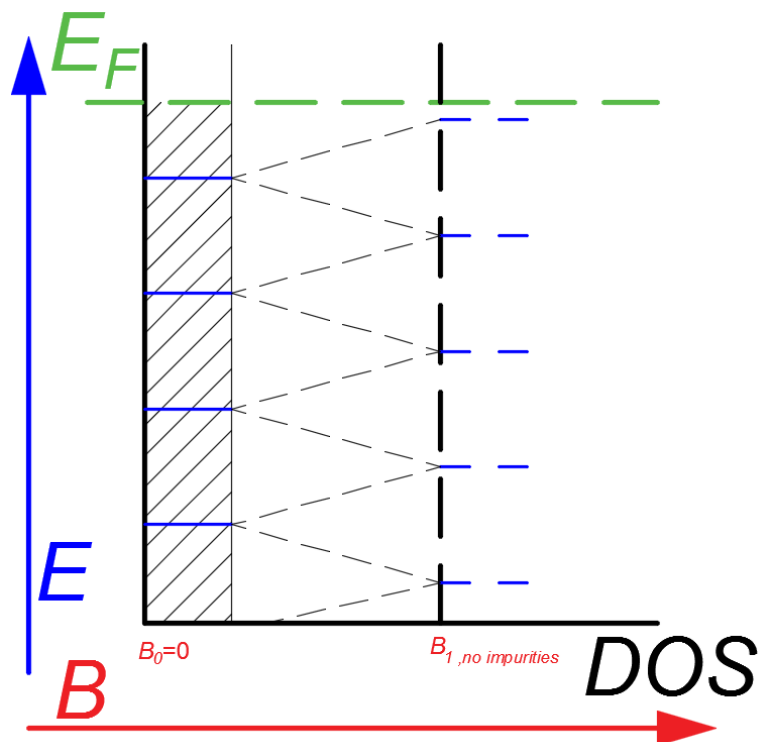


Figure 2.4.2 Density of states, DOS, changing under a magnetic field (without disorder broadening).

The filling factor ν is defined by the ratio of the number of electrons and the number of available states at a certain magnetic field B

$$\nu = \frac{N_e}{N_L} = \frac{\hbar n_e}{eB} \quad 2.4.8$$

In figure 2.4.3, the Landau level energies are shown as a function of magnetic field. The electrochemical potential increases following the Landau level until a lower level is emptied because of the increasing of Landau level degeneracy under an increasing magnetic field. After this point, the Fermi energy jumps to this empty lower level forming the saw-like pattern.

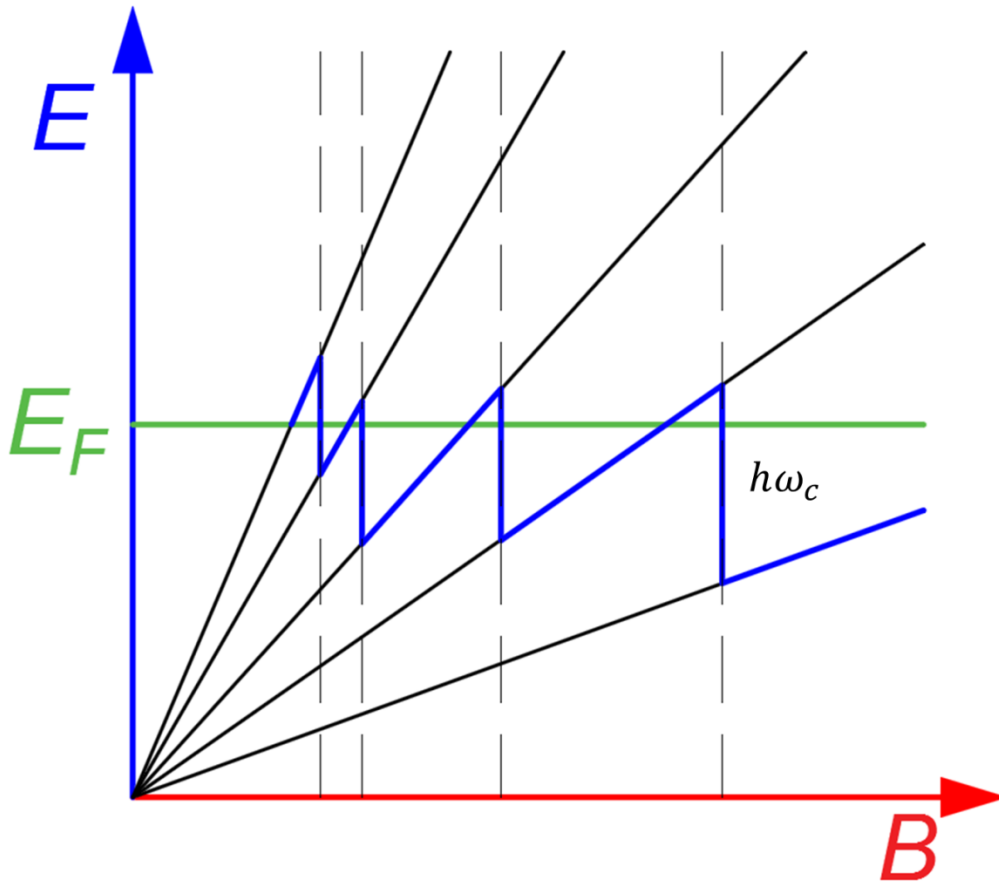


Figure 2.4.3 Landau level energy as a function of magnetic field. The chemical potential along the Landau level shows jumps of $\hbar\omega_c$ at all even filling factors (no broadening considered).

Disorder

Disorder, originating from impurities, crystalline defects and ionized remote-donors, produces a random impurity potential $U_{Disorder}(r) = \sum_i u_i(r - r_i)$, with u_i as the single potential. Thereby the Landau levels are broadened into a Gaussian-shaped energetic distribution [T.SMI1985] as a result of those potential fluctuations. Localized states, viewed as closed orbitals, are the consequence of disorder, where electrons are trapped around individual potential hills or valleys and cannot contribute to the sample conductance [S.ILA2004]. This is schematically shown in figure 2.4.4.

With the understanding of the disorder potential, we can empirically explain the integer quantum Hall effect. When the electrochemical potential drops inside the range of the mobility gap, the electron movement is parallel to equipotential lines, so that $\rho_{xx} = 0$. With B increasing, the fermi level shifts to the next (lower) Landau level, which eventually makes the localized states percolate to form an extended state covering the whole sample, $\rho_{xx} > 0$.

The Shubnikov-de Haas effect, measured in the longitudinal direction as shown in figure 2.4.1, is a result of Landau quantization and Landau level broadening, and shows oscillations as a function of the magnetic field with period of $1/B$.

$$\Delta\left(\frac{1}{B}\right) = \frac{2e}{\hbar n_e} \quad 2.4.9$$

To observe the Shubnikov-de Haas effect, the separation of the Landau level $\hbar\omega_c$ has to be bigger than the thermal excitations $k_B T$.

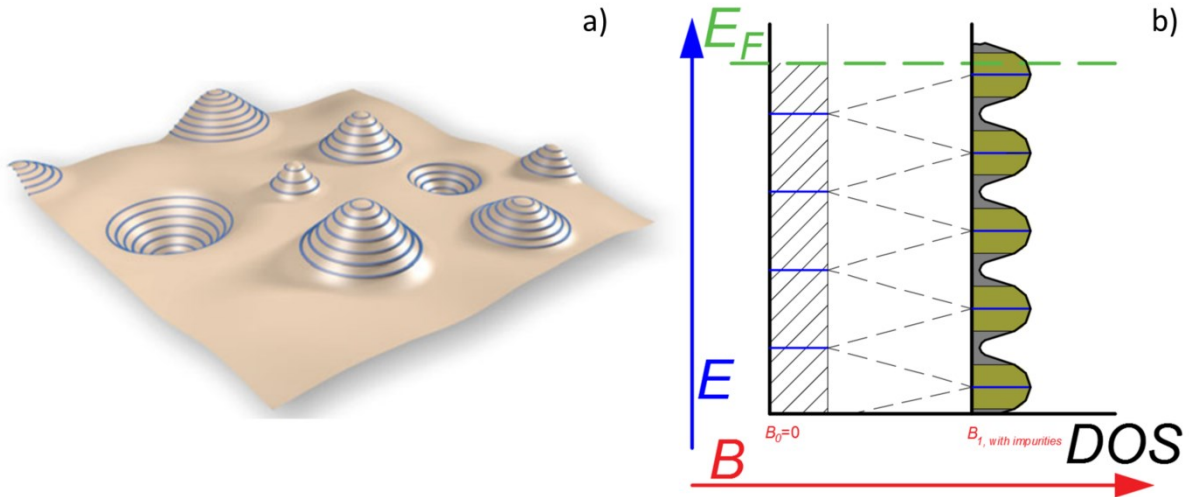


Figure 2.4.4 a) Illustration of localized states with electrons trapped around the spatially varying hills and valleys of electrostatic potentials in a disorder sample [B.FRI2014], b) Landau level broadening into extended and localized states due to disorder.

Boundary Conditions

When an integer number of Landau levels are filled, an infinite sample would be insulating, since all states are localized states. Due to the finite size of realistic samples, however, the Landau levels close to sample edges bend upwards and intersect with the Fermi energy as shown in figure 2.4.4 a). The Landau levels at the edges, which cross E_F , thus permit electrical transport parallel to the sample edges and form one dimensional edge channels (figure 2.4.4 b). The currents travel along opposite edges in opposite directions [S.DAT1995].

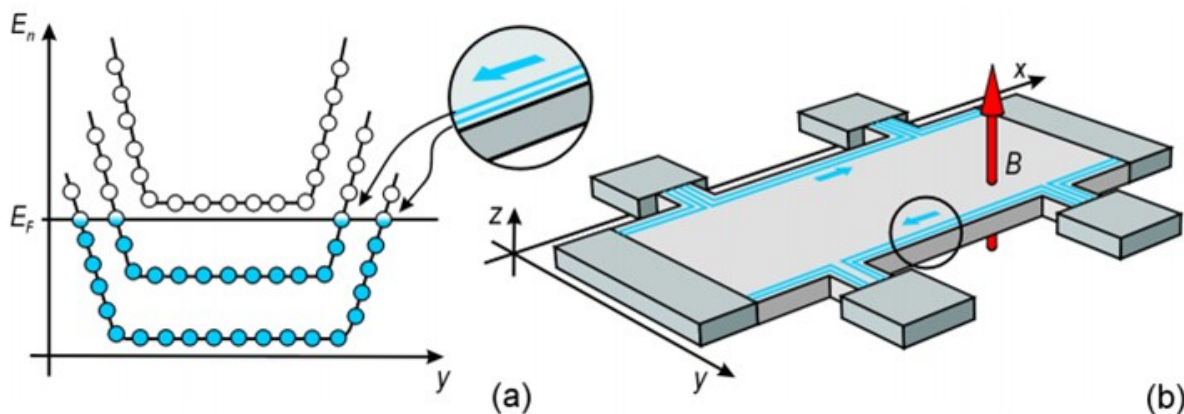


Figure 2.4.5 Demonstration of Landauer-Büttiker edge channel under filling factor of 2. A) The Landau levels close to the edge and cross the Fermi level, b) The Hall bar with two edge channels parallel to the sample boundary edges on both sides with counter propagating electrons [J.GOE2004T].

When one Landau level is completely filled, meaning the Fermi level lies in the mobility gap, dissipation through scattering for electrons moving along the edge channels is suppressed. Thus, the potential difference between two voltage probes located at the same sample edge is zero, i.e., the (longitudinal) voltage vanishes. The potential difference between edge channel of opposite edges, however, is finite and constant. The measured voltage across between two edges is given by natural constants of e^2/h . This behavior can be explained by the Landauer-Büttiker model [R.LAN1987, M.BUE1988]. The quantization of Hall resistance to R_H is a consequence of the potential difference across the sample resulted from the electrons moving in counter propagating directions along channels, determined by the potential gradient at the edges. The number of the channels occupied is equal to the filling factor.

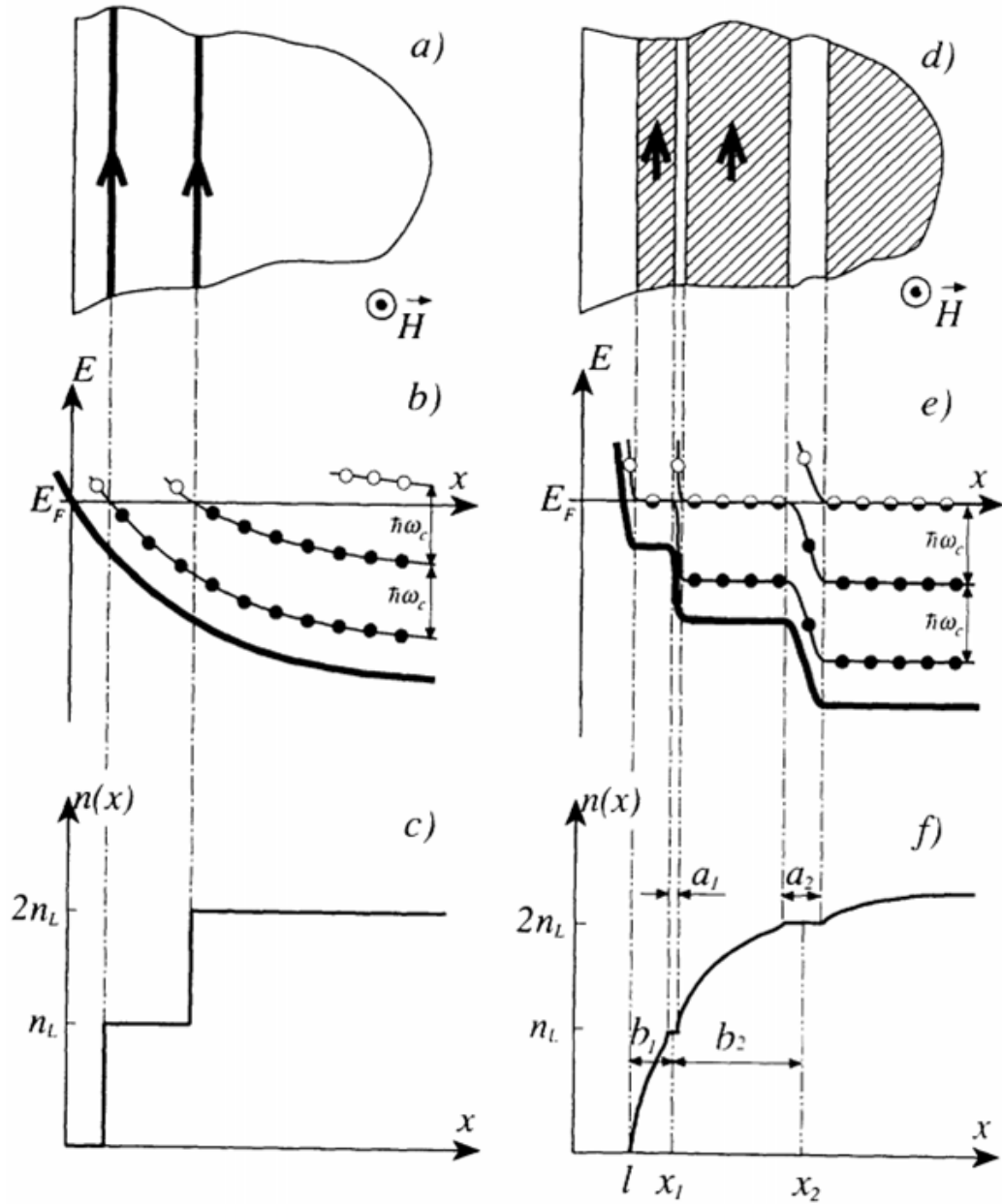


Figure 2.4.5 Edge state in integer quantum Hall effect regime without spin. a) to c) single electron condition without interaction. a) Edge channels resulted from the Landau level bending in b). c) The electron density changing as a function of distance to the edge. e) to f) self-consistent electrostatic condition. The compressed regions are shaded strips in d) near the edge, e) The electrostatic energy changing with distance close to the edge, f) Electron density versus the distance [D.CHK1992].

In the Landauer-Büttiker edge channel model, the density of states changes step like at each edge channel. However, according to the work by Chklovskii et al., [D.CHK1992, D.CHK1993, K.LIE1994] the electron density gradually varies into a depletion region between channels due to Coulomb repulsion between electrons. In self-consistent calculations using electrostatics and a chemical potential, the step-like manner is a consequence of the formation of alternating strip-regions: compressible and incompressible strips. Inside the compressible strips, the electron states are fixed at the Fermi energy level by adding electrons from bulk. In contrast, for the incompressible strips, the Fermi energy level lies in the mobility gap corresponding to fully occupied Landau levels and a related integer filling factor.

2.5 Electron Spin Resonance and Nuclear Spin Resonance

After discussing the origin of the Landau level formation in the previous section, I will now introduce the electron spin which adds an additional Zeeman splitting term to equation 2.4.5. The Zeeman splitting of the Landau level at large magnetic fields is the prerequisite for electron spin resonance (ESR), which allows to detect spin effects by measuring changes of the magneto-resistivity under electromagnetic wave radiation. Furthermore, I will show that hysteresis effects can arise due to hyperfine interaction between electron spin and nuclear spin.

Electron Spin Degree

The spin degree of freedom (denoted as s) is one of the four electron intrinsic quantum numbers used to determine how electrons are distributed in space around the nucleus according to Pauli Exclusion Principle [W.PAU1925]. Each electron can either be in a spin up state (\uparrow , or $+1/2$) or a spin down state (\downarrow , or $-1/2$) with energies $s g_e^* \mu_B B$ where s equals $\pm \frac{1}{2}$. When an external magnetic field is applied, the electron's Zeeman energy has two possible values corresponding to the two orientations of its magnetic dipole in the magnetic field. For electrons in a 2DES, this means that the Landau level split into two energy states with energy difference

$$E_z = g_e^* \mu_B B \quad 2.5.1$$

where g_e^* is the effective g factor and equals -0.44 in bulk GaAs [C.WEI1977], $\mu_B = e\hbar/2m_e$ is the Bohr magneton. The Zeeman energy increase linearly with the magnetic field as seen in figure 2.5.1 a). When the spin degeneracy is broken by the magnetic field, the density of states splits up in a spin up and a spin down Landau level and odd filling factors can be observed as shown in figure 2.5.1 b).

Typically, with $g_e^* = -0.44$ and $m^* = 0.067m$, the Zeeman energy is around $1/70^{\text{th}}$ of the cyclotron energy, which explains why the integer quantum Hall effect with even filling factors is dominant at low magnetic fields.

At sufficiently high magnetic fields, where the Zeeman energy is larger than the disorder broadening the spin-split Landau levels are fully separated and the spin polarization alternately varies between spin unpolarized at all even Landau level filling factor and maximum polarized at all odd Landau level filling factors

$$P_e = \frac{n_{e,\uparrow} - n_{e,\downarrow}}{n_{e,\uparrow} + n_{e,\downarrow}}$$

2.5.2

with $n_{e,\uparrow}$ and $n_{e,\downarrow}$ being the density of spin up and spin down electrons.

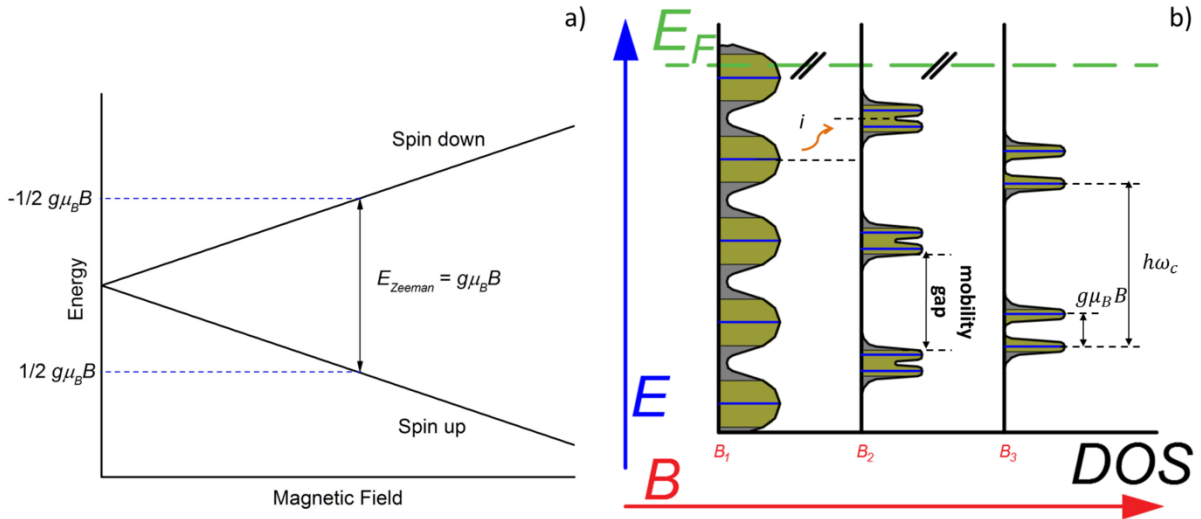


Figure 2.5.1 a) Zeeman splitting increases linearly with the magnetic field, b) Lifting of the spin degeneracy for the density of states in a magnetic field.

Electron Spin Resonance, ESR

Because of the small carrier density in a two dimensional electron gas, conventional ESR is not able to sensitively detect the spin resonance. However, the longitudinal resistivity is affected by ESR, which provides an indirect method to use the 2DES itself as a detector for electron spin resonance [D.STE1983, D.STE1984]. With this method, M. Dobers *et al.*, reports the magnetic field dependence of the effective g -factor in 1988 [M.DOB1988]. The sample in a Hall bar geometry was immersed in liquid helium. It was irradiated with microwaves up to 70 GHz between several mW to hundreds mW. When the photon energy from microwave matches the Zeeman energy,

$$E_{\text{phonon}} = \hbar\nu = g_e^* \mu_B B \quad 2.5.3$$

electrons in a spin-up Landau level will get excited to a spin-down state. Figure 2.5.2 a) shows the resistivity ρ_{xx} (dashed line) and its change $\Delta\rho_{xx}$ (solid line) under microwave radiation as a function of the magnetic field. While a static background resistivity change is caused by radiative heating, a sharp electron spin resonance peak appears at around 11.5 T, which shifts its magnetic field position when changing the microwave frequency. With a series of different microwave frequencies as shown in figure 2.5.2 b), the Zeeman splitting at each Landau level could be determined. The second Landau level Zeeman splitting for one of the samples (carrier density is $3.3 \times 10^{11} \text{cm}^{-2}$ and mobility is $300\,000 \text{cm}^2 \text{V}^{-1} \text{s}^{-1}$) was modeled as

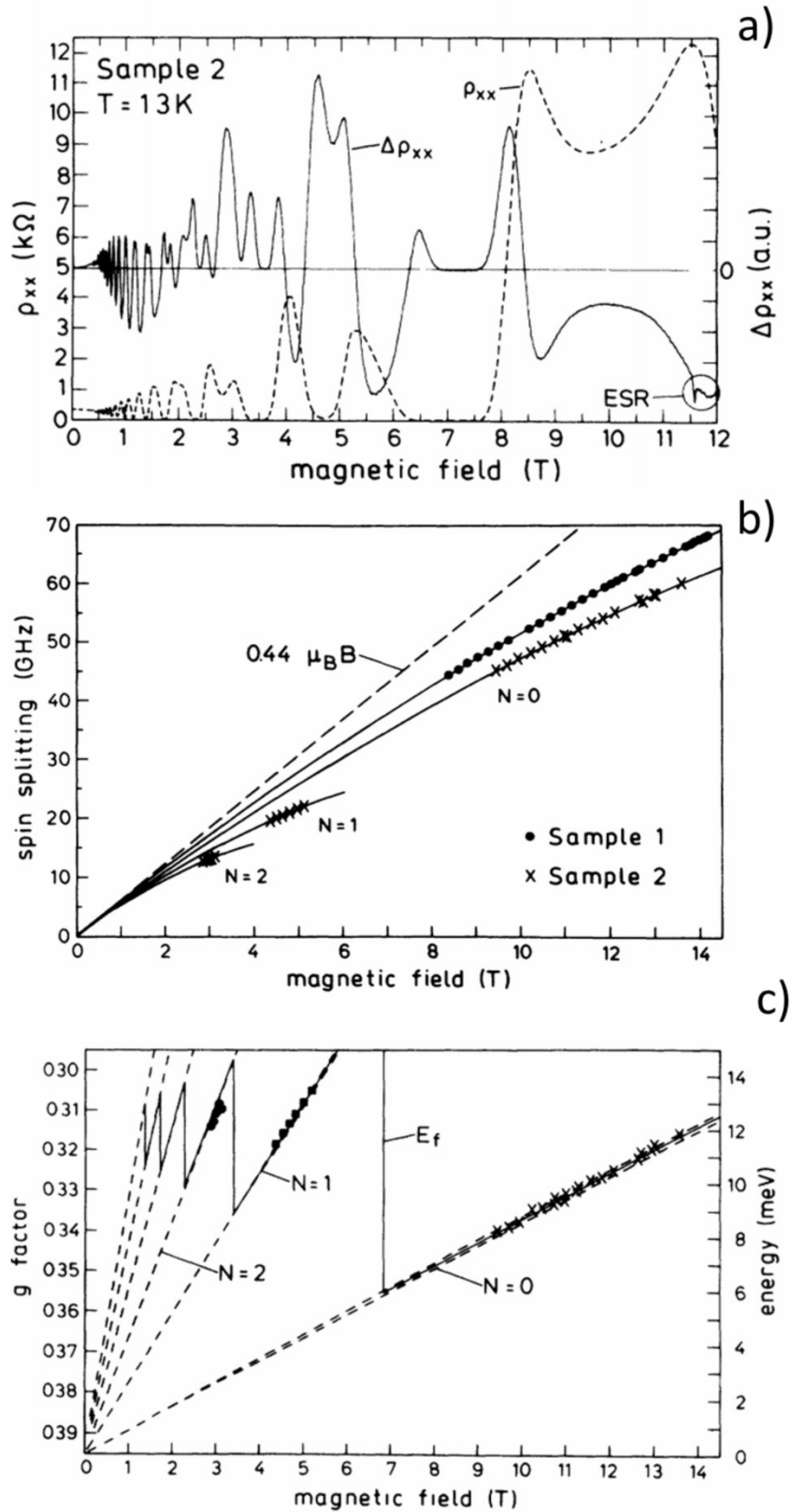


Figure 2.5.2 a) The dashed line represents the magnetoresistivity ρ_{xx} . The solid line shows the changes of $\Delta\rho_{xx}$ under microwave radiation. A spin resonance occurs at around 11.5 T, b) Measured spin splitting of the Landau levels with the dashed line representing the bulk-GaAs, c) effective g-factors for each Landau level vs. the magnetic field [M.DOB1988].

$$\Delta E = 0.15\text{GHz} + 0.40\mu_B B - [0.165 \left(N + \frac{1}{2}\right) \text{GHz}] \frac{B^2}{1\text{T}^2} \quad 2.5.4$$

Furthermore, the effective g -factor in the two dimensional system could be derived as a function of magnetic field and the Landau level

$$g(B, N) = g_0 - c \left(N + \frac{1}{2}\right) B \quad 2.5.5$$

with variables g_0 and c dependent on the samples. For this sample in Dobers report, g_0 is 0.40, and c is 0.0115 T^{-1} . The effective g -factor determined by the magnetic field and the Landau level is plotted in figure 2.5.2 c). The measured effective g -factor is different from the one in the bulk GaAs.

The magnetic field position of the electron spin resonance is also affected by the hyperfine coupling, i.e., an interaction between electron spin and nuclear spin, which results in small shifts of the electron spin resonance frequency.

Nuclear Magnetic Resonance

In a magnetic field, nuclei in semiconductor heterostructures can undergo a Zeeman splitting similar to the electrons. A GaAs quantum well consists of three stable nuclear isotopes (^{69}Ga with an abundance of 60%, ^{71}Ga with an abundance of 40% and ^{75}As with an abundance of 100%) that have a spin number I of 3/2 [Y.LI2008, K.LABY]. The Aluminum contribution from the confining AlGaAs barriers will not be considered, since the wave function is mostly located in the GaAs quantum well. In a magnetic field, the Ga and As nuclear magnetic moments have four possible orientations corresponding to four equally split Zeeman levels

$$E_{z,N} = -\vec{\mu}_M \cdot \vec{B} = -g_N \mu_N B \cdot \Delta m_I \quad m_j = -I, -I + 1, \dots, I - 1, I \quad 2.5.6$$

with g_N being the nuclear g -factor, $\mu_N = e\hbar/2m_p$ being nuclear Bohr magneton where m_p is the mass of proton. Because the proton mass m_p is much heavier than electrons mass m_e , the energy level splitting turns out to be much smaller than what electrons can experience at the same magnetic field.

Similarly to the previously discussed electron spin resonance, nuclear spins can be excited to higher energy levels by a specific radio frequency that matches the nuclear Zeeman splitting

$$E_{\text{phonon}} = h\nu = \frac{\gamma}{2\pi} B = E_{z,N} \quad 2.5.7$$

with $\gamma/2\pi$ being the gyromagnetic ratio as shown in table 2.5.1. The overall nuclear spin polarization is determined by the occupation of spins on the four energy levels

Table 2.5.1 The characteristics of the three nuclear isotopes in a GaAs quantum well [D.LID2008, M.DOB1988]

Isotope	⁶⁹ Ga	⁷¹ Ga	⁷⁵ As
Abundance (%)	60.1	39.9	100
Spin quantum number I	3/2	3/2	3/2
Reduced gyromagnetic ratio (MHz/T)	10.248	13.021	7.315
Overhauser shift (T)	-0.91⟨ I ⟩	-0.78⟨ I ⟩	-1.84⟨ I ⟩

$$P_n = \frac{\langle I \rangle}{I} = B_I(x) \quad 2.5.8$$

where $B_I(x)$ is Brillouin function with $x = g_N \mu_N IB / k_B T$. The nuclear spin system is unpolarized only when all the nuclei distribution among the four energy levels are identical, which easily occurs at elevated temperatures.

Hyperfine Interaction

When the nuclei in the GaAs quantum well are fully polarized, they can generate a few Tesla of an effective nuclear magnetic field, which acts on the electron spins via the *hyperfine interaction*. The hyperfine interaction, which is an interaction between electron and nuclear spins, can be expressed by the following Hamiltonian as

$$H = g\mu_B \mathbf{B} \cdot \mathbf{S} + A \mathbf{I} \cdot \mathbf{S} \quad 2.5.9$$

with \mathbf{S} and \mathbf{I} denoting the electron and nuclear spin, and A the hyperfine interaction constant. The first term on the right side of Equation 2.5.9 is the effect of an external magnetic field, the second term, i.e., the hyperfine interaction, is caused by the polarized nuclear spins. Nuclear polarization can occur due to relaxation at lowest temperatures, dynamical nuclear spin polarization using large currents or through ESR where electron spin flips are transferred to the nuclei due to the conservation of momentum

$$A \mathbf{I} \cdot \mathbf{S} = \frac{A}{2} (I_+ S_- + I_- S_+) + A I_z S_z \quad 2.6.0$$

with the first term on the right side being the electron-nuclear spin flip-flop term, describing spin relaxation. Dynamical polarization of nuclear results in a shift of the ESR position through the nuclear field B_N , called *Overhauser shift*. The nuclear field can be obtained by adding the overall contributions of the three types of nuclei in GaAs

$$\mathbf{B}_N = \sum_{i=1}^3 b_{N,i} \frac{\langle I_i \rangle}{I}, \quad b_{N,i} = \frac{A I x_{n,i}}{g_e^* \mu_B} \quad 2.6.1$$

with $x_{n,i}$ being the natural abundance as seen in table 2.5.1. The maximum shift could reach 5.3 T in bulk GaAs when all three nuclei are fully spin-polarized. The average of all nuclear spins results in the average of B_N

$$B_N = \frac{8}{3} \pi g_0 g_N \mu_N |\psi(0)|^2 \langle I \rangle / g_e^* \quad 2.6.2$$

with g_0 being the free electron g -factor. The Overhauser shift in a 2DES was firstly reported by M. Dobers in 1988 [M.DOB1988] with 0.2 T as shown in figure 2.5.3 a).

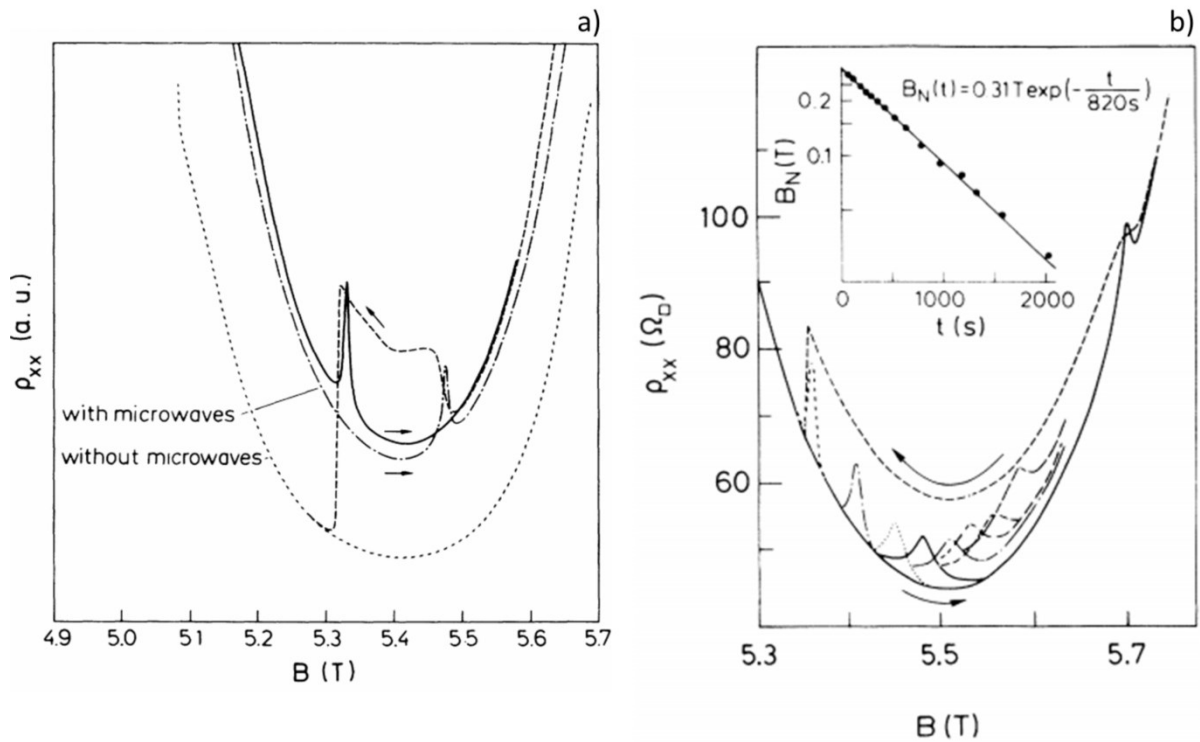


Figure 2.5.3 Hysteresis of the magneto resistivity due to the nuclear magnetic field. a) Under microwave irradiation with a frequency matching the electron Zeeman splitting, a hysteresis around filling factor 3 is seen. The bottom dashed trace is the background measurement without microwave radiation; the dash-dot trace is the first measurement with ESR with a resonance at around 5.5 T. The dashed trace with left pointing arrow is a magnet downsweep. Due to the finite nuclear spin polarization, the resonance starts at the same position but shifts down to around 5.3 T, where ρ_{xx} coincides with the background measurement. The solid line is the second measurement under microwave irradiation; here, the resonance appears at 5.3 T [M.DOB1988]. b) Overhauser shift for magnetic field up and down sweep. Inset: nuclear magnetic field, B_N as a function of time showing the nuclear spin relaxation [A.BER1990].

Nuclear Spin Relaxation

When nuclei have dynamically been polarized by ESR or by a large current, nuclear relaxation back to a thermal equilibrium can take between seconds and days, depending on the magnetic field, temperature and/or filling factor of the 2DES. In a two dimensional system, the energy conservation of the flip-flop processes during nuclear spin relaxation is affected by the degeneracy of the (spin-split) Landau levels and the large Zeeman energy mismatch between electrons spin and nuclear spins.

In 1990, A. Berg [A.BER1990] studied the nuclear relaxation time as seen in figure 2.5.3 b) with the same sample used by M. Dobers [M.DOB1988]. The nuclear magnetic field B_N is measured as a function of time shown in the inset, indicating relaxation time of the order of 10^3 seconds.

Various mechanisms can influence nuclear spin relaxation: 1) electron spin-orbit coupling [K.HAS2005], 2) phonon-assisted relaxation [R.COT1977, J.KIM1994] and 3) nuclear spin diffusion [D.PAG1982]. However, a detailed discussion would be beyond the scope of this thesis.

2.6 Monolayer Graphene Two Dimensional Systems

Monolayer graphene, consisting of a single layer of carbon atoms arranged in a “honeycomb” lattices, can be regarded as a “truly” two dimensional carrier systems. After the theoretical study of the two dimensional carbon atom band structures by Wallance in the 1940s [P.WAL1947], it took around 60 years to experimentally separate single graphene sheets from 3D graphite. In 2004, K. S. Novoselov and A. K. Geim [K.NOV2004] peeled off monolayer graphene with Scotch Tape and transferred it to a Si/SiO₂ substrate. Under an optical microscope, this method allowed visual discrimination between single layer and multiplayer graphene. For their important discovery, K. S. Novoselov and A. K. Geim were awarded Nobel Prize in Physics in 2010.

Lattice and Electronic Structure in Graphene

As summarized by A. H. Neto in a review of graphene electronic properties [A.NET2009], here we will briefly review fundamental aspects of graphene. As shown in figure 2.6.1, the carbon atoms in graphene in the hexagonal lattices are bond to three nearest neighbors in x-y plane, performing sp^2 -hybridized orbitals. This bond, which is called σ -bond, is formed from three out of four valence electrons around the carbon atom. The other remaining p -orbital forms the out of plane, anti-binding π -bond. The honeycomb lattice consists of two equivalent interleaving sublattices, represented by atoms A and B. The distance between two nearest neighboring carbon atoms is $a \approx 1.42 \text{ \AA}$. In each hexagonal unit cell, it has two basis atoms A and B.

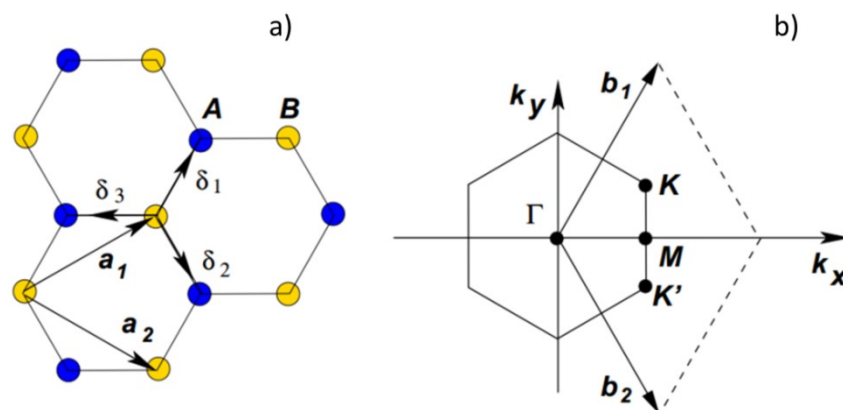


Figure 2.6.1 a) Graphene honeycomb lattice in real space, with two triangular sublattices **A** (blue dots) and **B** (yellow dots) and the unit vector **a** and the nearest neighbor vector δ , b) The corresponding reciprocal space of a unit cell lattice in Brillouin Zone with highly symmetric points **K** and **K'** [A.NET2009].

The real space vectors in figure 2.6.1 can be written as

$$\mathbf{a}_1 = \frac{a}{2}(3, \sqrt{3}), \quad \mathbf{a}_2 = \frac{a}{2}(3, -\sqrt{3}) \quad 2.6.1$$

With the corresponding reciprocal lattice vectors

$$\mathbf{b}_1 = \frac{2\pi}{3a}(1, \sqrt{3}), \quad \mathbf{b}_2 = \frac{2\pi}{3a}(1, -\sqrt{3}) \quad 2.6.2$$

With the two important points in graphene, i.e., the Dirac point K and K' , located at the corners of the Brillouin Zone represented by

$$\mathbf{K} = \left(\frac{2\pi}{3a}, \frac{2\pi}{3\sqrt{3}a}\right), \quad \mathbf{K}' = \left(\frac{2\pi}{3a}, -\frac{2\pi}{3\sqrt{3}a}\right) \quad 2.6.3$$

And the vector of the three nearest neighbors in real space

$$\boldsymbol{\delta}_1 = \frac{a}{2}(3, \sqrt{3}), \quad \boldsymbol{\delta}_2 = \frac{a}{2}(3, -\sqrt{3}), \quad \boldsymbol{\delta}_3 = -a(1, 0) \quad 2.6.4$$

And the vector of the second nearest neighbors in real space

$$\boldsymbol{\delta}_1 = \frac{a}{2}(3, \sqrt{3}), \quad \boldsymbol{\delta}_2 = \frac{a}{2}(3, -\sqrt{3}), \quad \boldsymbol{\delta}_3 = -a(1, 0) \quad 2.6.4$$

The electrons in graphene move through the lattice by hopping between the nearest and second nearest neighbors. The corresponding Hamiltonian can be written in tight-binding approach as

$$\hat{H} = -t \sum_{\langle i,j \rangle, \sigma} (a_{\sigma,i}^\dagger b_{\sigma,j} + H.c.) - t' \sum_{\langle i,j \rangle, \sigma} (a_{\sigma,i}^\dagger a_{\sigma,j} + b_{\sigma,i}^\dagger b_{\sigma,j} + H.c.) \quad 2.6.6$$

with operator $a_{i,\sigma}$ or $a_{i,\sigma}^\dagger$ annihilating or creating an electron on sublattice A on site \mathbf{R}_i with Spin σ (\uparrow, \downarrow), which also works for sublattice B, t (around 2.8 eV) and t' (between $0.02t \leq t' \leq 0.2t$) representing the nearest and second nearest neighbor hopping energy. From this Hamiltonian, the energy bands can be calculated in

$$E_{\pm}(k) = -t\sqrt{3 + f(k)} - t'f(k) \quad 2.6.7$$

$$f(k) = 2 \cos(\sqrt{3}k_y a) + 4 \cos\left(\frac{\sqrt{3}}{2}k_y a\right) \cos\left(\frac{\sqrt{3}}{2}k_x a\right)$$

with the upper π band and the lower π^* band being shown with plus and minus sign, respectively.

The corresponding energy in the linear region around Dirac points is

$$E_{\pm}(\mathbf{q}) \approx \pm \hbar v_F |\mathbf{q}| \quad 2.6.8$$

where v_F is the Fermi velocity, around $1 \times 10^6 \text{ms}^{-1}$.

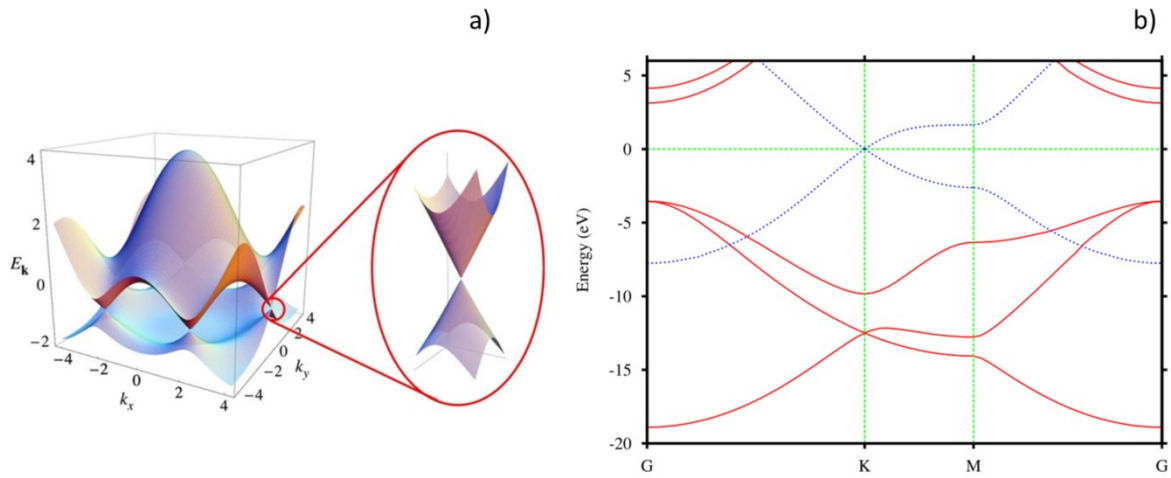


Figure 2.6.2 band structure of monolayer graphene [A.NET2009, D.BOU2008]. The conduction band and valence band touch at six equivalent Dirac points K and K' . At low energies near the Dirac points, the dispersion is linear (or conical in k_x - k_y space).

Transport in Graphene

The band structure of Graphene as shown in figure 2.6.2 converges at the Dirac points at K and K' with a vanishing density of states, i.e., it exists a “charge neutrality point”, CNP [S.WIE2011]. In real samples, however, the resistance does show a singularity at the Dirac points. Impurities, thermal activation and the existence of electron and hole puddles around the Dirac points lead to broadened peak with a finite resistance instead. Here, we define the charge neutrality point as the point of equal concentrations of electrons and holes where the mobility reaches a maximum (and the carrier density a minimum) as shown in figure 2.6.3 when a gate voltage is tuned [K.NOV2005].

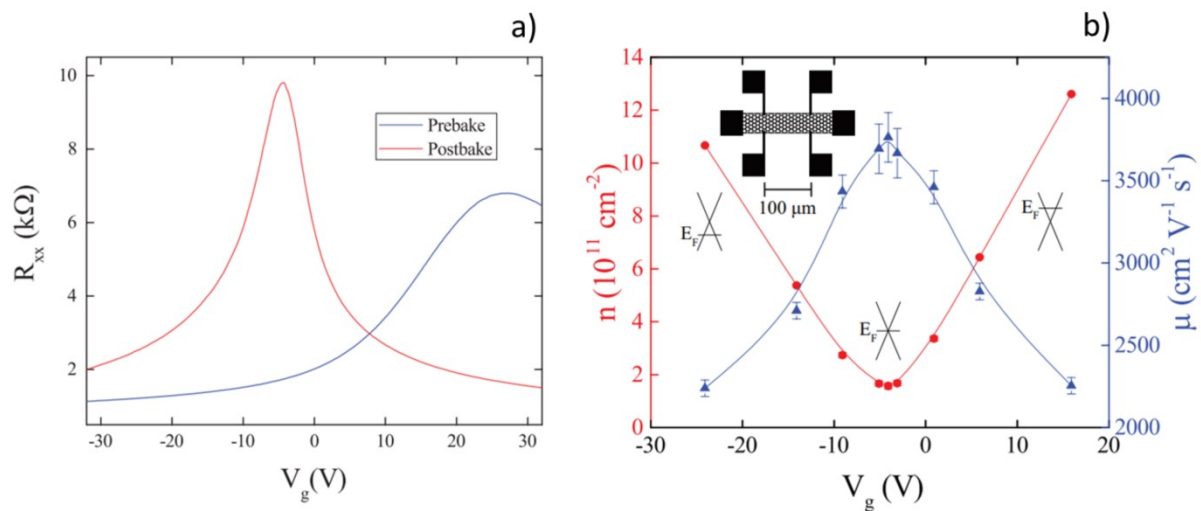


Figure 2.6.3 a) Longitudinal resistance of a Graphene Hall bar at 4.2 K. For a baked sample (red line), the CNP shifts to lower gate voltage because surface contaminants (doping) are removed. b) Charge carrier density and mobility as a function of gate, labeled with red and blue, respectively [T.LYON2017].

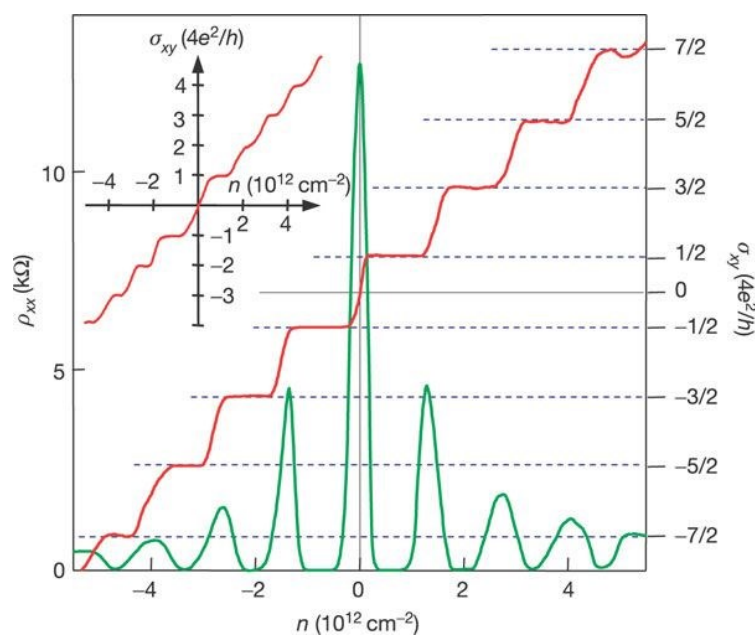


Figure 2.6.4 Hall conductivity and longitudinal resistivity of graphene as a function of carrier density at fixed magnetic field of 14 Tesla and 4.2 Kelvin [K.NOV2005]. The insert shows bilayer graphene with normal quantization sequence at integer filling factors.

The quantum Hall effects is a significant experimental feature of two-dimensional systems. However, the quantum Hall effects observed in graphene are different from those found in conventional 2D semiconducting materials because of graphene's band and lattice structure, resulting in a fourfold degeneracy for the charge carriers. The corresponding Landau level energies in Graphene become a function of square root of the magnetic field

$$E_n = \pm \sqrt{2e\hbar v_F^2 |n| B}, \quad |n| = 0, 1, 2, 3, \dots \quad 2.6.9$$

where n represents the Landau level index of electrons in the positive range and for holes in the negative range. This energy spectrum produces a half-integer sequence of energy levels, which further results in a $1/2$ shift in the quantum Hall conductivity, as shown in figure 2.6.4

$$\sigma_{xy} = \nu \frac{e^2}{h} = \frac{4e^2}{h} (n + 1/2) \quad 2.6.10$$

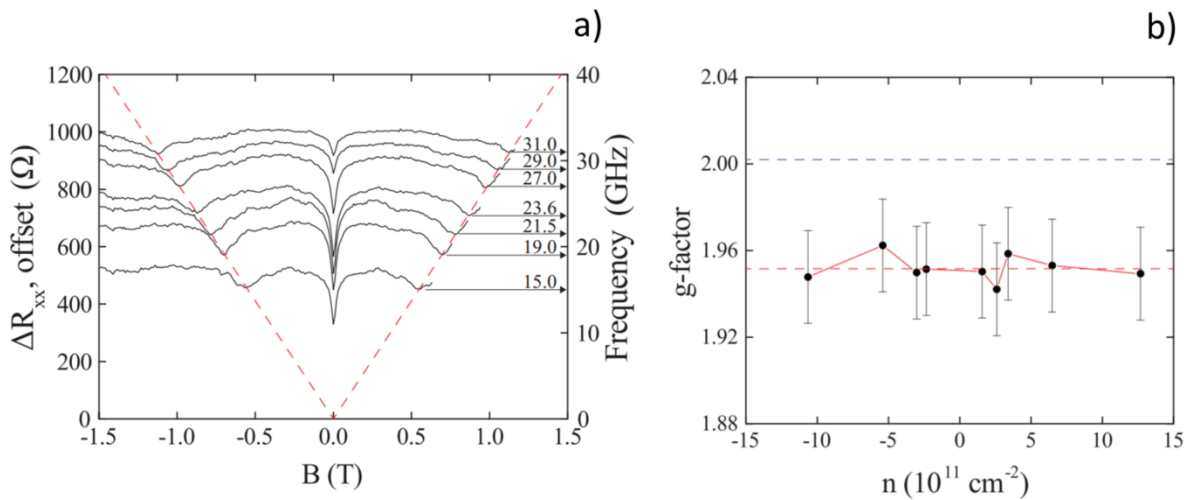


Figure 2.6.5 Electron spin resonance measurements on monolayer graphene by Timothy J. Lyon and Jonas Sichau *et al.*, in [T.LYO2017]. a) Frequency dependence of the magnetoresistance change as a function of magnetic field, the dashed line indicates the Zeeman splitting, with the slope representing the g -factor of 1.952, d) g -factor as a function of charge carrier density (negative for holes, positive for electrons).

***g* factor of Graphene**

Of all the spin-related aspects in graphene, the *g*-factor of charge carriers is always of fundamental interest. As mentioned in the previous sections, the *g*-factor can be deduced from resistively-detected electron spin resonance, ESR, measurements at different magnetic fields. Timothy J. Lyon and Jonas Sichau *et al.*, [T.LYO2017, T.LYO2017T] systematically studied monolayer graphene transferred to plain Si/SiO₂ substrates using ESR as shown in figure 2.6.5. According to Equation 2.5.3, the *g*-factor can be calculated as

$$g = h\nu/\mu_B B \quad 2.6.11$$

Using ESR, the *g*-factor of charge carriers in graphene was determined to be 1.952 ± 0.002 .

CVD Grown Graphene

All graphene samples studied in this thesis were grown by *Graphenea Inc* [GRAPHEN], using chemical vapor deposition, CVD, on copper foil. The CVD growth process is schematically shown in figure 2.6.6 [Z.YAN2012] with parameters in Table 2.6.1 [Z.YA2012S]. To avoid the formation of carbon islands, a pyrolysis method on a CH₄ precursor is used. By performing the growth on a metal substrate, the reaction temperature can be reduced to approximately 1000 °C. On the hot copper surface, the precursor break apart, releasing the Carbon atoms which diffusive (or desorb) and stick to impurities in the copper foil. Additional carbon atoms form bond to these nucleation sites, building larger islands, which percolate into a closed Graphene sheet. Due to the low solubility of carbon on a carbon substrate, only monolayers will form.

Table 2.6.1 Different parameters used in CVD grown graphene in Figure 2.6.5 b) to g) [Z.YA2012S].

sample	E1	E2	E3	E4	E5	E6
Temp (°C)	1060	1060	1060	1060	1070	1075
Growth-CH ₄ (sccm)	5	0.15	0.15	0.15	0.15	0.15
Growth-time(min)	1	15	70	80	110	120
Growth-pressure (Torr)	8.2	8.2	8.2	108	108	108
Growth-H ₂ (sccm)	500	70	70	70	70	70
Annealing time (h)	0.5	0.5	7	7	7	7
Annealing pressure (Torr)	8.2	8.2	1500	1500	1500	1500
Cu-polishing	No	No	Yes	Yes	Yes	Yes

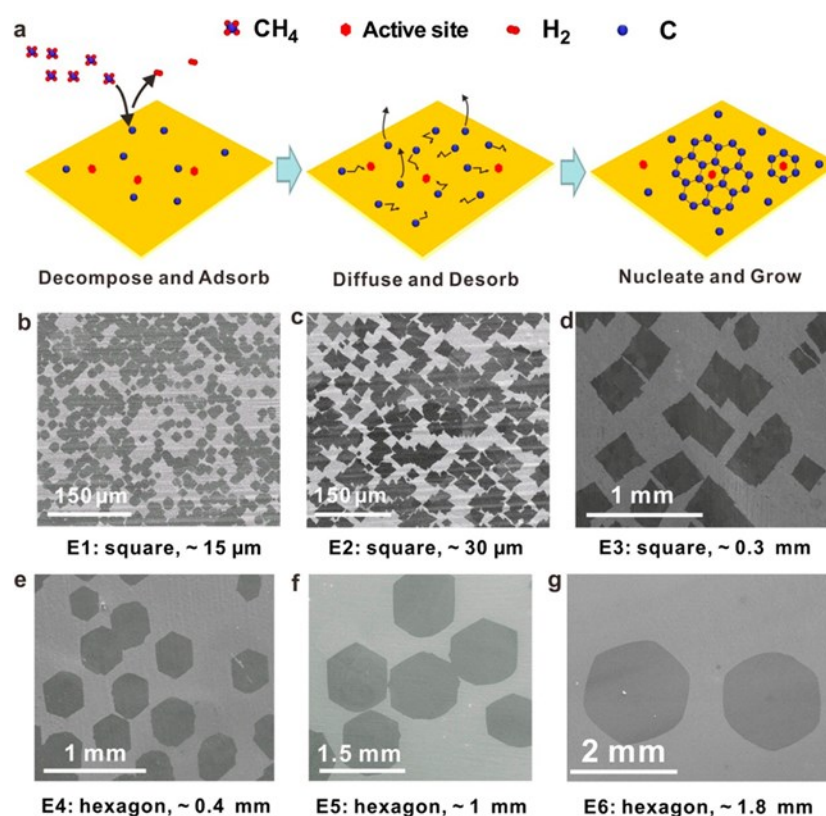


Figure 2.6.6 a) CVD of graphene on a copper foil. CH₄ is decomposed, the carbon atoms are adsorbed, diffuse (or desorb) and attach themselves to nucleation sites, b) to g) Scan electron microscope, SEM, profile of the graphene synthesized by CVD process under parameters shown in table 2.6.1 [Z.YAN2012].

2.7 Suspended 2D Nano-Electromechanical Systems

Freestanding nanoelectromechanical systems (NEMS) integrate electronics with mechanical actuators on a nanometer scale and operate as “nano-resonators”. This section will briefly review the advantages of nano-mechanical suspended system and methods of fabrication using 2DES embedded in GaAs/AlGaAs heterostructures. In combination with electrical transport in a 2DES, NEMS can be used in device applications for mass spectroscopy and molecule detection.

Integrating a two-dimensional system into a freestanding nanostructure (of tens to hundreds nanometer thickness), adds a mechanical degree of freedom and isolates the bulk/substrate phonons from the 2DES. In such a nano-mechanical system, both the electrons and phonons are confined, and the phonon density can be controlled to study electron-phonon interaction. Due to the confinement, some phonon modes are strongly suppressed, while others are enhanced, which allows enhancing or reducing the dissipation process in the electronic system.

The combination of a freely suspended nanostructure with a low-dimensional electron system opens up versatility in both fundamental physics and device applications. The physical mechanisms underlying the mechanical motions is utmost important for such a detached nanostructure for actuating and sensing of ultra-small masses [J.CHA2012], forces and displacement [M.RIE1999, A.CLE2002], or bio-molecule detecting [M.HAN2012].

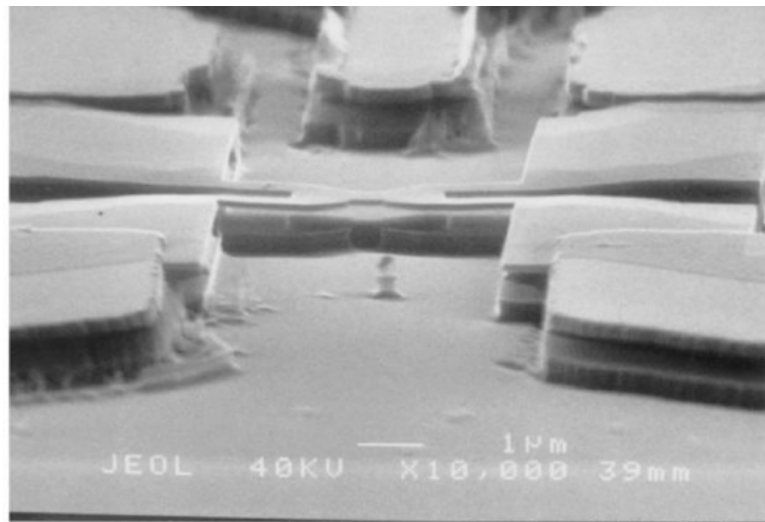


Figure 2.7.1 Scanning electron microscope side view image of a partially released Hall bar with $1 \times 2 \mu\text{m}^2$ size [R.BLI2000].

Realization of Suspended Nanostructures

In GaAs/AlGaAs heterostructures with a sacrificial layer of AlAs, the AlAs can be etched away by dilute Hydrofluoric acid, HF, with a high selectivity (above 10^5 [X.WU1985, M.VON2004]), releasing the upper semiconducting layers. Since the Al fraction in the $\text{Al}_x\text{Ga}_{1-x}\text{As}$ compound is usually below 0.5, the 2DES incorporated in the GaAs/AlGaAs interface remains intact.

One way to achieve freestanding nanostructures is to selectively undercut the AlAs sacrificial layer by 2% buffered HF after defining a mesa structure by patterning through multiple optical lithography steps, annealing of Ohmic contacts and subsequent ion-beam etching down to the sacrificial layer [R.BLI2000]. An example of a suspended $1 \times 2 \mu\text{m}^2$ Hall bar is shown in figure 2.7.1.

Another method to fabricate a freestanding system is based on epitaxial lift-off (ELO), in which the heterostructure is separated and transferred from GaAs substrate to a glass substrate with a pre-patterned cavity. E. Yablonovitch *et al.* [E.YAB1987, E.YAB1990] have demonstrated that the GaAs heterostructure can be bonded to arbitrary substrate as shown in figure 2.7.2 a). The heterostructure films were protected by wax during the HF undercutting and wafer-bonded (“van der Waals”) to a new substrate, such as LiNbO_3 , glass, silicon or sapphire substrate. ELO can be used to release entire wafers of GaAs as shown in figure 2.7.2 b) [G.BAU2014, J.SCH2005].

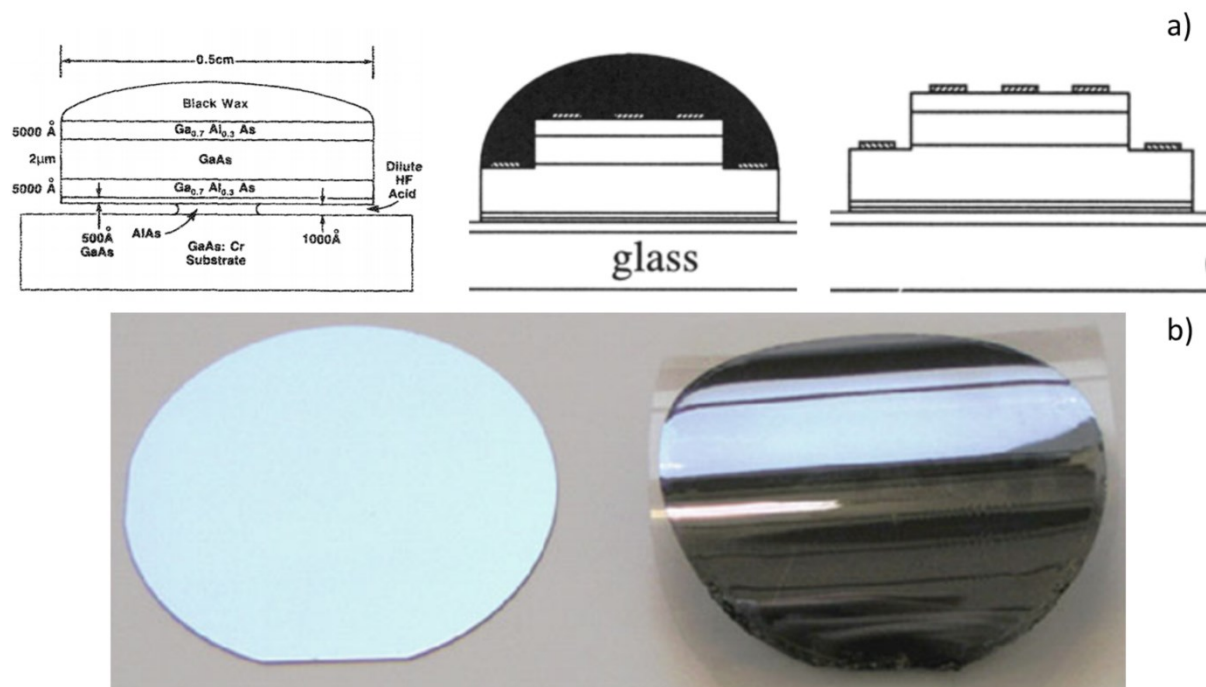


Figure 2.7.2 a) Basic process of ELO, left: undercutting of the heterostructures, the middle and right: the transfer process [E.YAB1987, X.LEE1997], b) ELO technology used on 2-inch GaAs wafers for $1 \mu\text{m}$ film transfer [J.SCH2005].

Magnetotransport Properties of Suspended 2D Systems

The magnetotransport of a suspended Hall bar structure was studied by E. M. Weig *et al.* [E.HOE2002, E.WEI2003T]. As shown in figure 2.7.3, the quantum Hall effects and Shubnikov-de Haas oscillations are preserved. The longitudinal resistance of a suspended structure close to zero magnetic field is enhanced with additional fine structures.

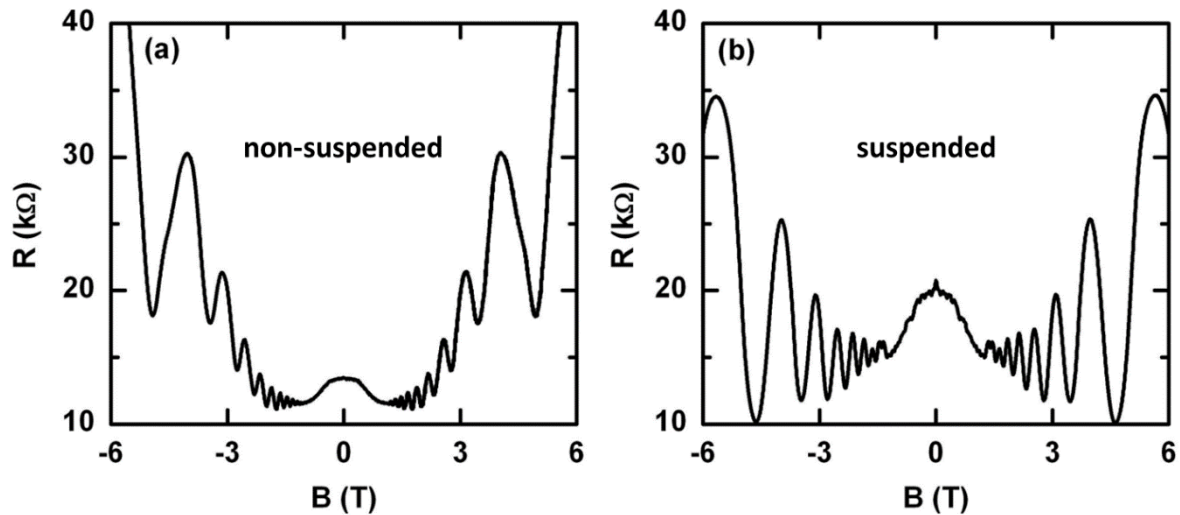


Figure 5.7.3 Magnetoresistance measurements a) before and b) after releasing the Hall bar structure [E.WEI2003T].

Additional studies by A. G. Pogosov *et al.* [A.POG2012] investigated the influence of the shape of the released 2DES on the magnetotransport. They found that the shape of the boundaries of the suspended regions affects the edge potential, which can enhance scattering between edge channels. Figure 2.7.4 illustrates how the shape can affect the quantum Hall effect, with non-vanishing longitudinal resistance at integer filling factors due to scattering between edge channels using the design of a) and b) with results in e), and the vanishing longitudinal resistance reappearance after modifying the released Hall bar structures to c) and d) with results in f).

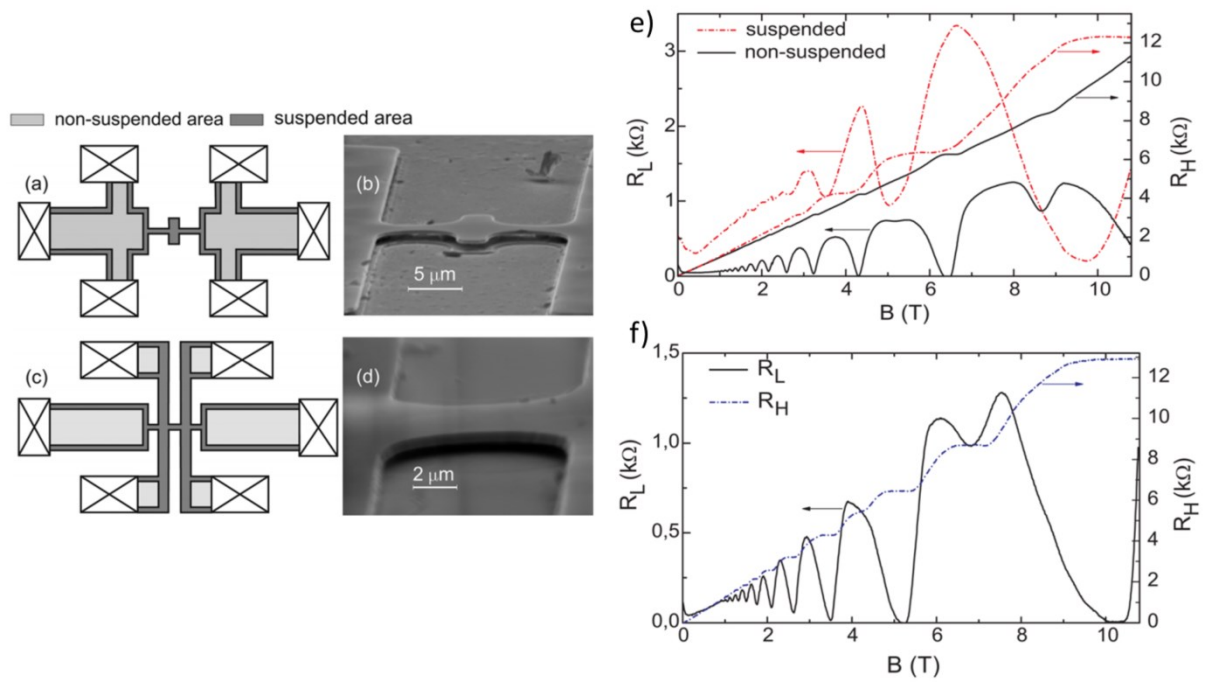


Figure 2.7.4 Comparison between two types of suspended Hall bars in a)/b) and c)/d). e) Results of design in a)/b): the red dashed line represents the longitudinal resistance, which does not vanish as compared to the black solid line representing a non-suspended structures, f) Results of modified design in c)/d): recovery of vanishing longitudinal resistance for integer filling factors in a suspended structure [A.POG2012].

2.8 Surface Acoustic Waves and Two-Dimensional Electron Systems

In 1885, John William Strutt, 3rd Lord Baron Rayleigh, demonstrated a wave [L.RAY1885] later named *Rayleigh wave*, which travels primarily along the surface of an elastic medium, also named surface acoustic waves, SAWs. This mechanical wave has a longitudinal and vertical shear component, corresponding to an elliptical surface particle motion. The elastic energy is mostly confined to a superficial layer so that the amplitude of displacement decreases exponentially into the substrate as illustrated in figure 2.8.1, i.e., typically vanishing at one to two wavelength [DAN.RUSS].

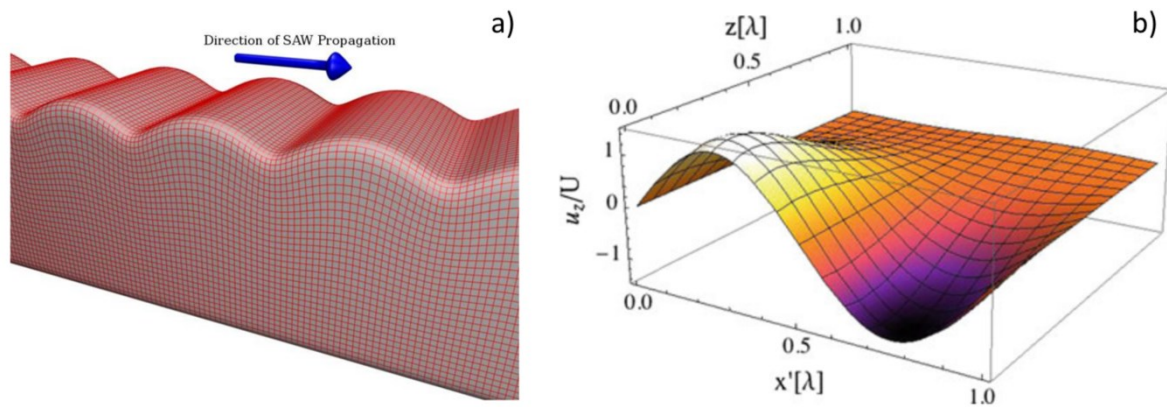


Figure 2.8.1 a) Illustration of surface acoustic waves propagating along a surface of the elastic medium with vertical displacement exaggerated. The grid lines represent the crystal lattice. The amplitude decreases in z -direction. b) Calculated acoustic amplitude in z -direction versus wavelength of SAWs. Figures from [M.AST2008, M.SCH2016].

Acoustic excitations of two-dimensional electron systems deliver complement information when compared with conventional magnetotransport. The interaction between SAWs and a 2DES leads to two main effects [J.SHI1995, J.SHI1996]: (1) damping of the SAW's velocity due to the conductivity of the 2DES, which was used to study geometric resonances of the cyclotron motion of composite Fermions; and (2) generation of acoustoelectric currents driven by varying electric potential in the 2DES, which are immune to impurities and are stable over changes in temperature.

In this thesis, I will use high frequency SAWs to generate acoustoelectric currents in a two-dimensional electron system and study the response to magnetic fields, low temperatures, microwaves.

With the advancement of modern lithography techniques, such as electron beam lithography, EBL, and nanoimprint lithography, SAWs can be integrated with microelectromechanical systems (MEMS) and nanoelectromechanical systems (NEMS), to control and exploit electron-phonon coupling. In SAW-driven NEMS, anomalous acoustoelectric current [L.SON2010], shock waves [F.BEI2008], and single electron transports [R.MCN2011] is possible.

SAW Generation and Propagation in Piezoelectric Materials

In piezoelectric materials, an applied electric field can produce an elastic deformation and vice versa, which is needed for the generation of SAWs [R.WHI1965]. The propagation of SAWs is related to both a mechanical (deformation) energy and an electric energy, together forming the elasto-electromagnetic waves. Table 2.8.1 lists the piezoelectric parameters of various substrates commonly used for the generation of SAW. This thesis focuses on GaAs since the two-dimensional electron systems are based on GaAs/AlGaAs heterostructures (related properties are shown in Table 2.8.2). Tests have also been done on lithium niobate LiNbO_3 crystals since it has a much larger effective piezoelectric coupling coefficient.

Table 2.8.1 parameters of some piezoelectric materials, K^2 is electromechanical coupling coefficient, defined by $K^2 = -2\Delta v/v$, where Δv and v are the velocity change and unperturbed velocity of SAWs [C.CAM1989].

Material	Crystal Cut	SAW Axis	Velocity(m/s)	$K^2(\%)$	Temperature Coefficient of the Decay (ppm/ $^{\circ}\text{C}$)
Quartz	ST	X	3158	0.11	0
LiNbO_3	Y	Z	3488	4.5	+94
LiNbO_3	128°	X	3992	5.3	+75
BiGeO_{20}	110	001	1681	1.4	+120
LiTaO_3	Y	Z	3230	0.72	+35
GaAs	<001>	(110)	<2841	<0.06	$\simeq -49$

Table 2.8.2 Typical parameters of GaAs/AlGaAs [S.ADA1985].

Parameter	GaAs	AlAs	$\text{Al}_x\text{Ga}_{1-x}\text{As}$
Static dielectric constants ϵ_s	13.18	10.16	13.18-3.12x
High-frequency dielectric constant	10.89	8.16	10.89-2.73x
Magnetic susceptibility $\chi_m(\times 10^{-5}\text{cm}^3/\text{mole})$	-3.33	-2.51	-3.33+0.82x
Piezoelectric constant $e_{14}(\text{C}/\text{m}^2)$	-0.16	-0.225	-0.16-0.065x
Piezoelectric constant $d_{14}(\times 10^{-12}\text{m}/\text{V})$	-2.69	-3.82	-2.69-1.13x
Electromechanical coupling constant K_{14}	0.0617	0.094	0.0617+0.323x

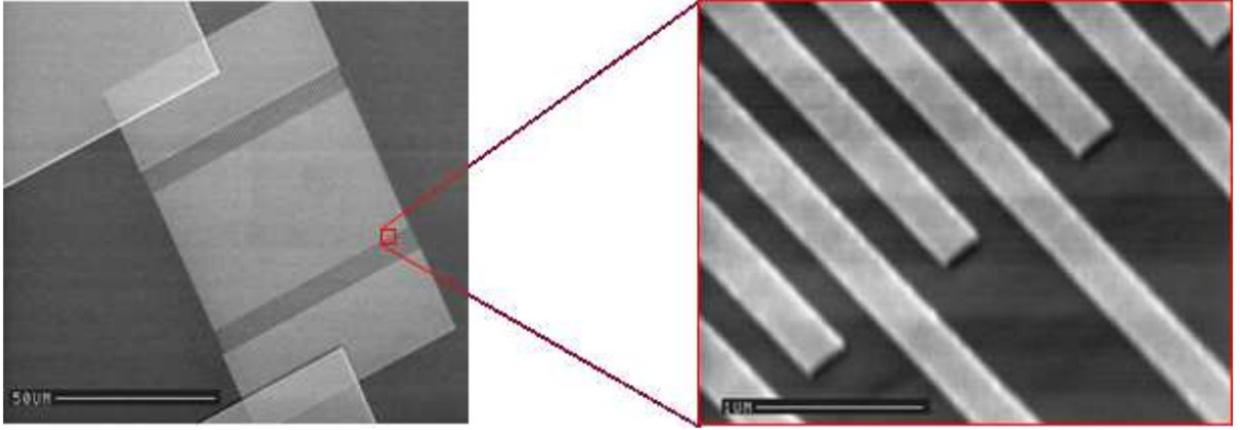


Figure 2.8.2 Example of interdigitated transducers with 70 pair of single fingers, separated by 1 μm [M.AST2008].

SAWs can be generated by applying an ac radio frequency of appropriate power to an interdigitated transducer, IDT, which consists of equally spaced metal fingers on top of a piezoelectric substrate as shown in figure 2.8.2. The required frequency to launch SAWs can be calculated by the pitch of IDTs, L , and the sound velocity in the piezoelectric materials

$$f = v/\lambda = v/L_{IDTs} \quad 2.8.1$$

with a narrow frequency range in $\delta f = f/N$, where N is the number of IDTs fingers pairs. When an alternating electric potential is applied to the metal fingers, the potential difference between the alternating finger electrodes gives rise to an alternating mechanical deformation of the piezoelectric substrate. The SAWs will propagate away from IDTs along the surface as shown in figure 2.8.3 [D.KRE2011, D.KRE2012T].

The alternating stress and strain displacement [D.KRE2011, G.FAR1978, A.HUT1962] which is induced by the piezoelectric coupling can be solved by Hooke's law and the Maxwell's equation

$$T_{ij} = c_{ijkl}S_{kl} + e_{nij}E_n \quad 2.8.2$$

And

$$S_{kl} = \frac{1}{2} \frac{\partial u_k}{\partial x_l} + \frac{\partial u_l}{\partial x_k} \quad 2.8.3$$

where $i, j, k, l = 1, 2, 3$. The wave propagation along the surface is described by

$$U = |U|e^{i(\omega t - kz)}e^{-k|y|} \quad 2.8.4$$

With ω being the angular frequency and k the phase constant.

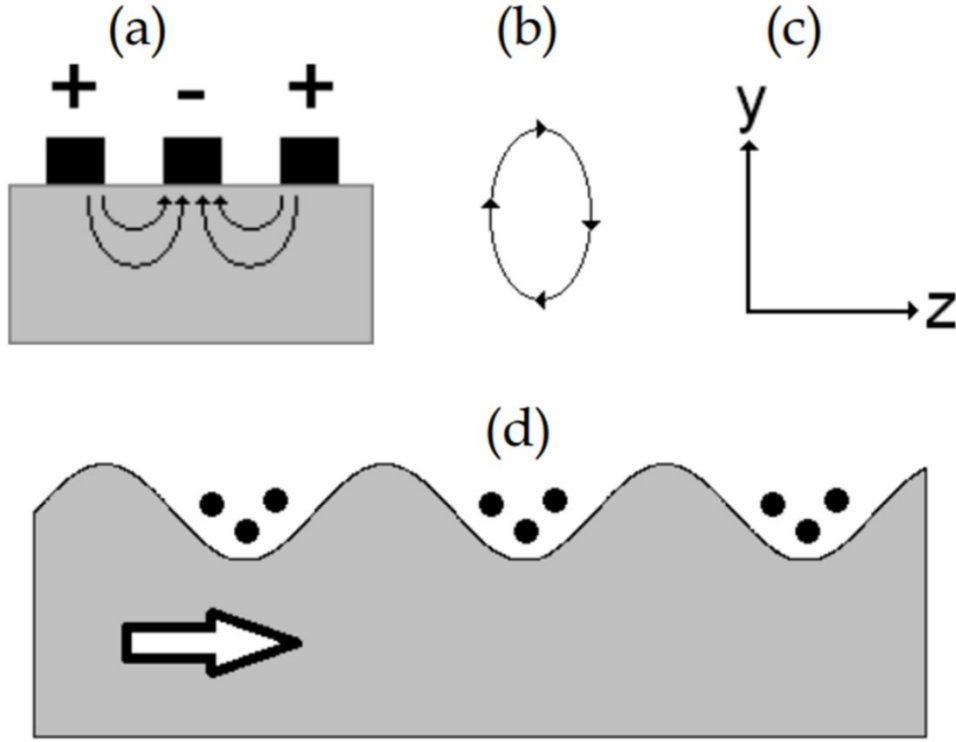


Figure 2.8.3 a) Illustration of the SAWs generation using alternating electrode fingers, b) The SAW propagation lead to an elliptical motion of the atoms in the crystal lattice, c) Materials axis orientation, d) Propagation of SAWs with trapped electrons [D.KRE2012T].

The created electric potential form the propagating wave can be described as

$$\Phi = |\Phi| e^{i(\omega t - kz)} e^{-k|y|} \quad 2.8.5$$

The electric field intensity generated along the SAWs is

$$E_i = -\frac{\partial \Phi}{\partial x_i} \quad 2.8.6$$

SAW Interaction with 2DES in GaAs/AlGaAs Heterostructure

The interaction between SAWs and a 2DES can be studied by magnetotransport at low temperatures and high magnetic fields. The surface acoustic wave attenuation Γ and velocity change probes the density of states and reproduces the Shubnikov-de Haas oscillations of 2DES. By launching surface acoustic waves from one IDTs and detecting the signal with an additional IDTs at the opposite side of the sample/Hall bar, the wave attenuation and phase change can be measured in a homodyne and standard boxcar integration technique [J.HEI1984].

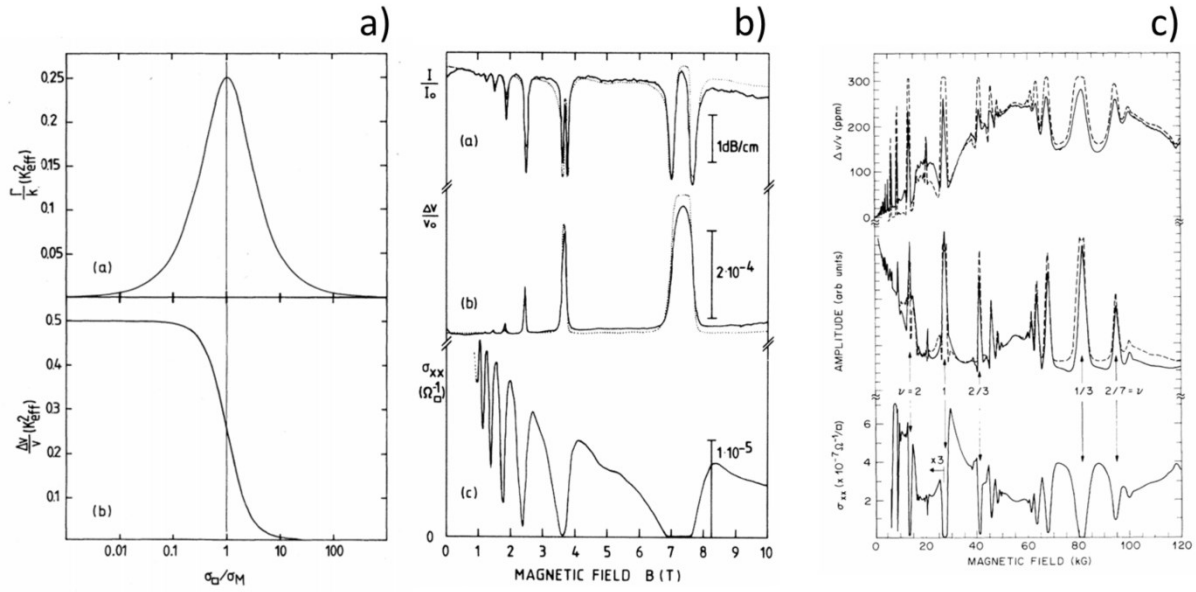


Figure 2.8.4 a) Attenuation factor and velocity change [A.WIX1989]. The attenuation reaches a maximum when the conductivity σ_{xx} is the same as characteristic conductivity σ_m , both for integer quantum Hall effects in b) [A.WIX1986] and fractional quantum Hall effects in c) [R.WIL1994]. Here, σ_m is an experimental determined value of $4 \times 10^{-7} (\Omega/\square)^{-1}$.

Attenuation and phase can be described by

$$\Gamma = \frac{\alpha k (\sigma_{xx}/\sigma_m)}{1 + (\sigma_{xx}/\sigma_m)^2}, \quad \sigma_m = v(\epsilon_0 + \epsilon_s) \quad 2.8.8$$

And

$$\frac{\Delta v}{v} = \frac{v(\sigma_{xx}) - v_0}{v} = \frac{\alpha}{1 + (\sigma_{xx}/\sigma_m)^2} \quad 2.8.9$$

where α being the effective piezoelectric coupling coefficient and ϵ_0 and ϵ_s are the vacuum and semiconductor dielectric constants. In a (100) GaAs surface, α and σ_m are 0.036% and $3.3 \times 10^{-7} (\Omega/\square)^{-1}$ for the [011] direction [T.GRU1981, A.WIX1986]. As can be seen in figure 2.8.4, the experimental data (solid line) fit well the theoretical model (dash line) for both integer quantum Hall effects and fractional quantum Hall effects [A.WIX1986, R.WIL1993, R.WIL1994].

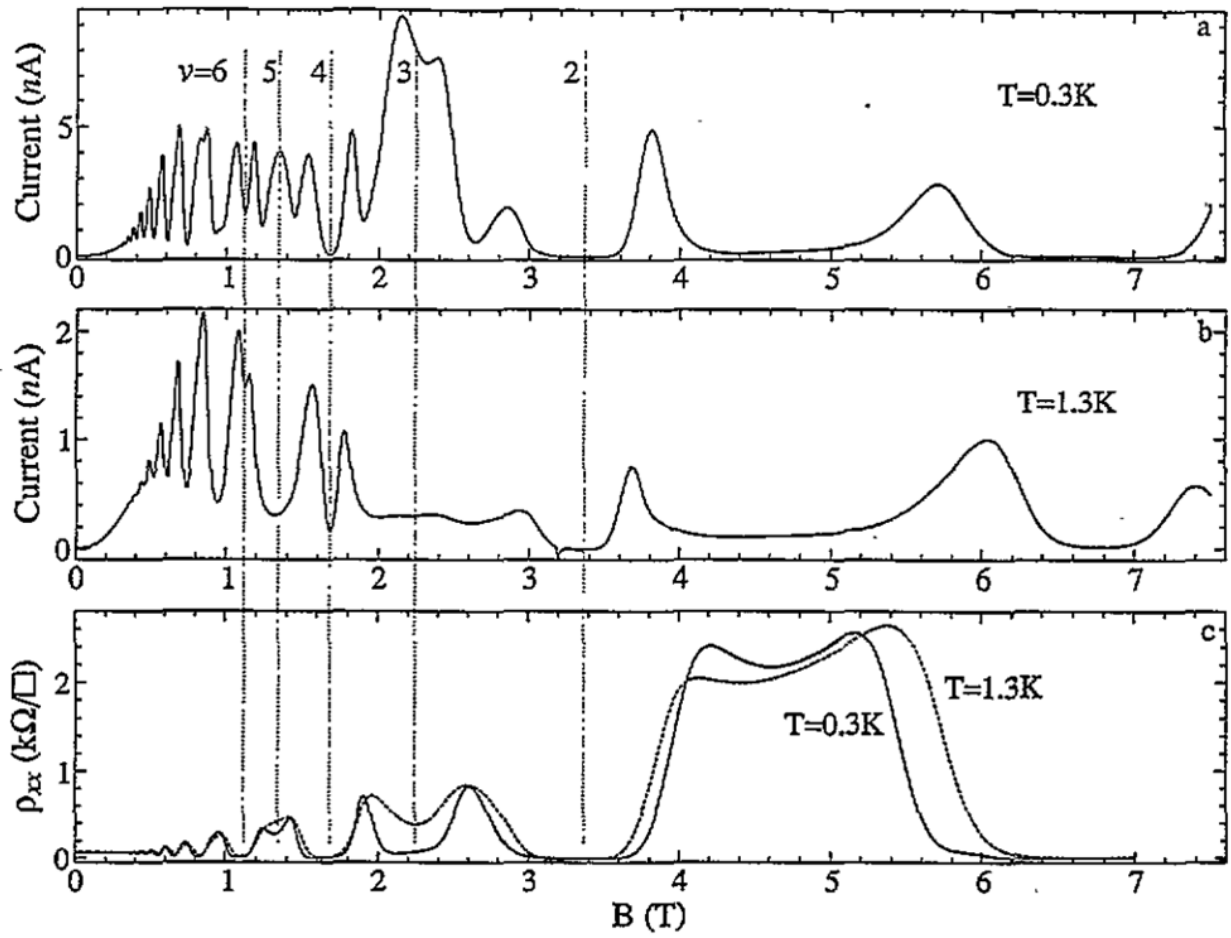


Figure 2.8.5 The acoustoelectric current measured as a function of magnetic field at 0.3 K in a) and 1.3 K in b), which produces the oscillations of the longitudinal resistivity in c) [J.SHIL1995].

In addition to the attenuation and velocity of SAWs, the direct measurement of the acoustoelectric current also reflects the magnetotransport resistance oscillations of a two-dimensional electron system. As shown in figure 2.8.5, the acoustoelectric current reproduces the oscillations in the longitudinal resistance for both 1.3 K and 0.3 K [J.SHIL1995].

SAWs induced Acoustoelectric Current in Graphene

Recently, SAWs induced phonon-electron interaction of graphene on a piezoelectric substrate has been reported [P.THA2010]. By exciting IDTs on piezoelectric substrates, i.e., a LiNbO_3 substrate, an acoustoelectric current was generated which was detectable in a graphene sheet resting on the substrate as shown in Figure 2.8.6 [V.MIS2012].

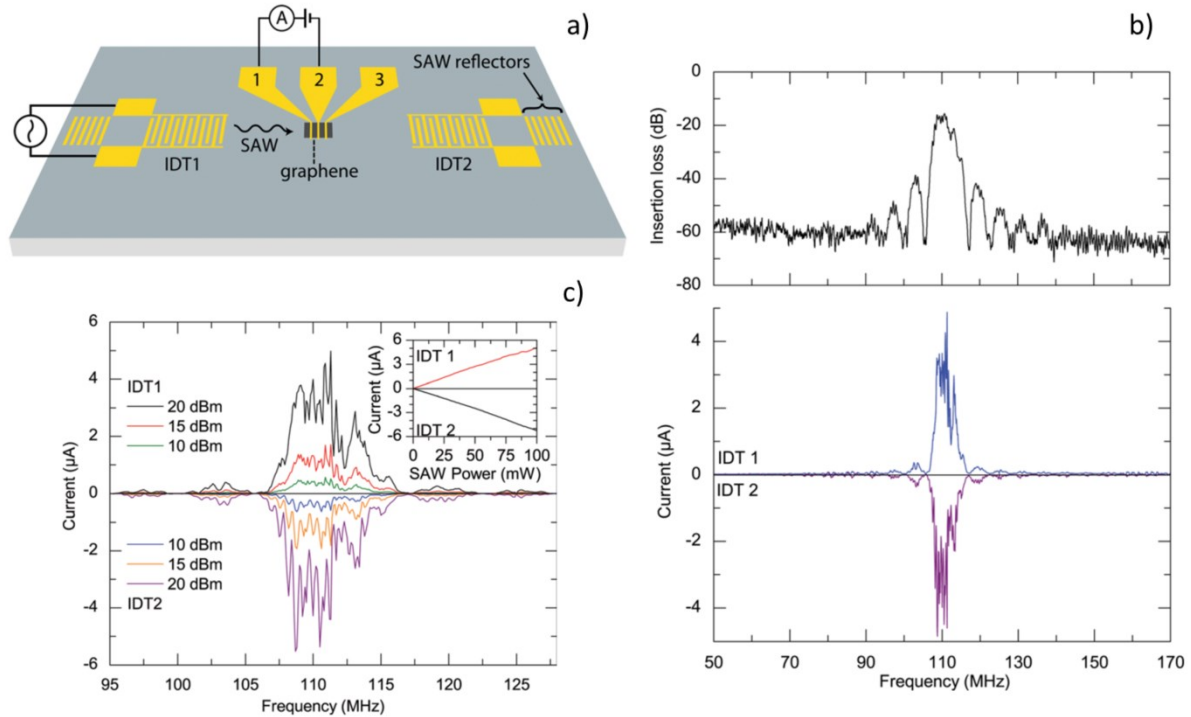


Figure 2.8.6 a) Sample schematic layout, b) Top panel: transmittance of an IDTs on either side of graphene as shown in a), showing the response of the IDTs. Bottom panel: amplitude of the acoustoelectric current generated from either IDTs, being maximum around the resonance frequency, c) Power dependence of the acoustoelectric current [V.MIS2012].

Chapter 3

Sample Fabrication

The following Chapter 3 describes the sample fabrication of conventional III/V semiconductors and monolayer graphene on semi-insulating GaAs substrates. The fabrication of interdigitated transducers, IDTs, by electron beam lithography will be described, which are the prerequisite to excite surface acoustic waves, SAWs. Releasing/suspending thin layers of semiconducting materials can enhance their amplitude. The required processing steps to release a structure will be discussed.

3.1 Hall Bar structures in GaAs/AlGaAs Heterostructures

A standard optical lithography method is used to define and pattern Hall bar structures and Ohmic contacts for magnet transport measurements. Figure 3.1.1 illustrates the pattern transfer and processing steps to fabricate a Hall bar structure. Three consecutive optical lithography steps define the overall sample region, Ohmic contacts and a top gate. After defining the mesa in the first step and wet chemical etching, contact regions are patterned in the second lithography step. Physical vapor deposition, PVD, of Au/Ge makes the electrical contact with the 2DES when the metal diffuses into the semiconductor during thermal annealing. In the final lithography step, a top gate region is defined. A thin layer Au/Ti deposited by PVD over the Hall bar make a top gate to tune the carrier density. During the processing, several crucial steps determine the sample quality.

Patterns Design and Fabrication

The patterns for Hall bars, contacts and gates are sketched with a commercial software called *ELPHY Plus* from Raith Nanofabrication GmbH [M.RAITH]. This sample pattern generation software is also used for sub-micrometer structure fabrication in electron beam lithography. The structure files can be converted to a format readable by a laser lithography machine, DWL 66+ from Heidelberg Instrument. This machine writes the patterns into blank quartz metalized with chromium and coated with S1800 series photoresist from G-materials [HEIDELBERG, G.MATERIALS].

To obtain well-defined lithographic patterns on the samples, it is extremely important to fabricate high quality masks. After fabrication, masks are usually cleaned with *piranha* (a solution of sulfuric acid and hydrogen peroxide) to remove residual photoresist after laser

writing. Since the minimal feature size limitation of our MJB4 Mask Aligner Instrument from Süss Microtec is around 1 μm [SÜSS], the dimensions of all our structures fabricated by standard photolithography are designed to be above 3 to 5 μm . The mask used in optical lithography in “step 1” in figure 3.1.1 is shown in figure 3.1.2. With this mask, I am able to fabricate samples as in figure 3.1.2. Fabricated Hall bar structures have a width of the order of tens of micrometers, and a length of the order of hundreds of micrometers. The square size of contacts is of the order of hundreds of square micrometers.

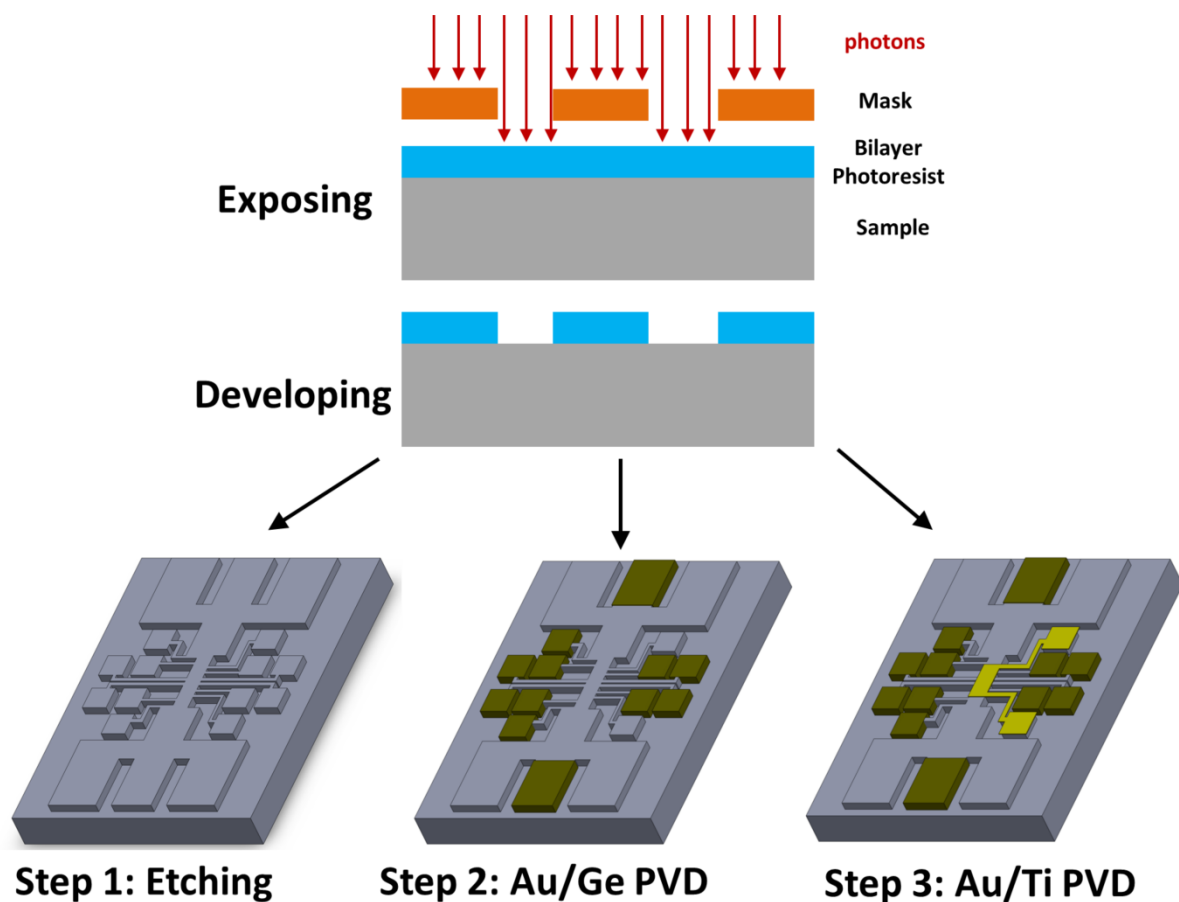


Figure 3.1.1 Process for Hall bars fabricated on GaAs/AlGaAs heterostructures. Exposure and developing transfers the mask pattern to the photoresist on the sample. A process using positive photoresist is used for steps #2 and #3. Negative photoresist with inverted patterns is used for step #1. Additional processes include wet chemical etching and PVD.

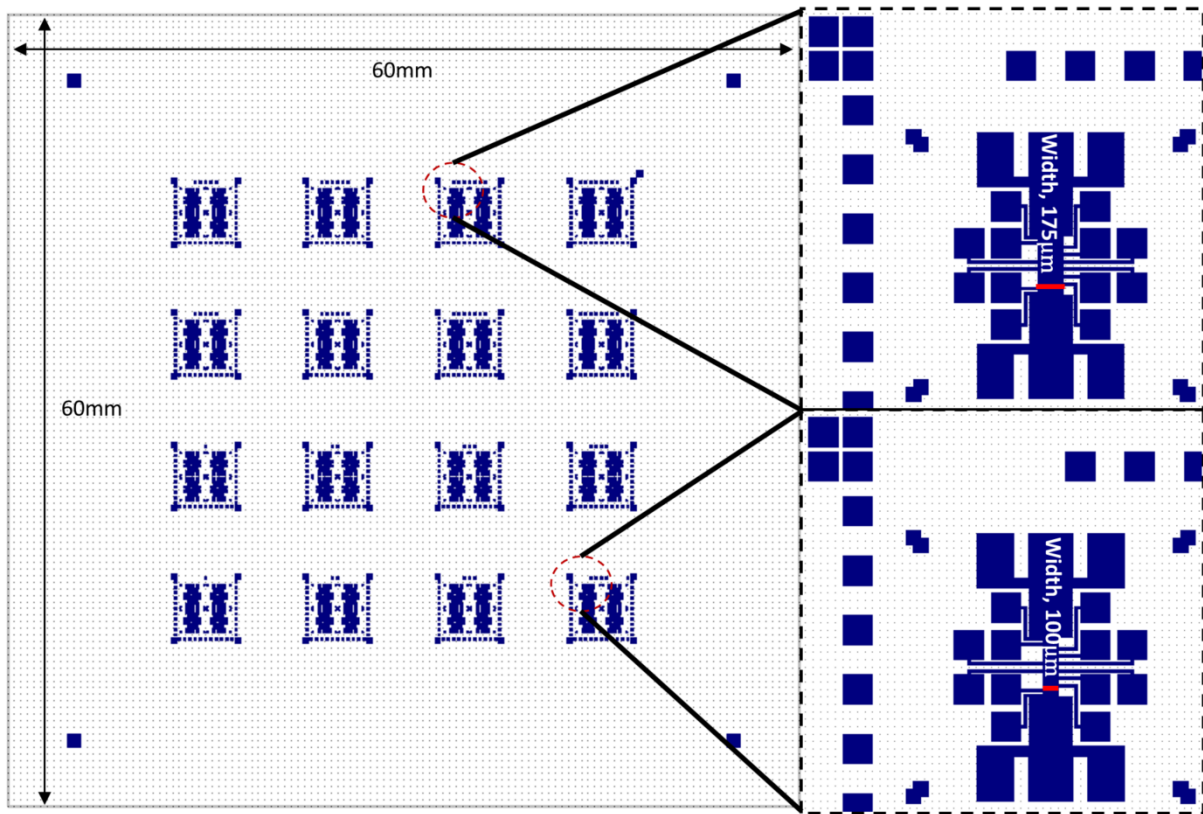


Figure 3.1.2 Lithography mask used in “step 1” in figure 3.1.1 with two enlarged regions with different Hall bar dimensions. The blue regions on the mask will be exposed in DWL 66+.

Etching

After transferring the patterns from the optical mask into the photoresist on the sample by standard UV lithography, a wet chemical or dry etching process is used to engrave the structure into the semiconducting materials. Initially, reactive ion etching, RIE, of GaAs was performed in the group’s Oxford Plasmalab 80 Plus with SiCl_4 . With the anisotropic ion beam etching, uniform structures with high reliability steep edges can be obtained. However, this dry etching setup broke and was no longer available. Alternatively, I use wet chemical etching based on phosphoric acid [E.CHA2001, N. GAYE2018T]. The etchant solution is a mixture of $\text{H}_3\text{PO}_4:\text{H}_2\text{O}_2:\text{H}_2\text{O}$ (10:20:400 ml) with etching rate of 150 to 170 nm per minute. 5 to 6 minutes are thus sufficient to etch through the heterostructures.

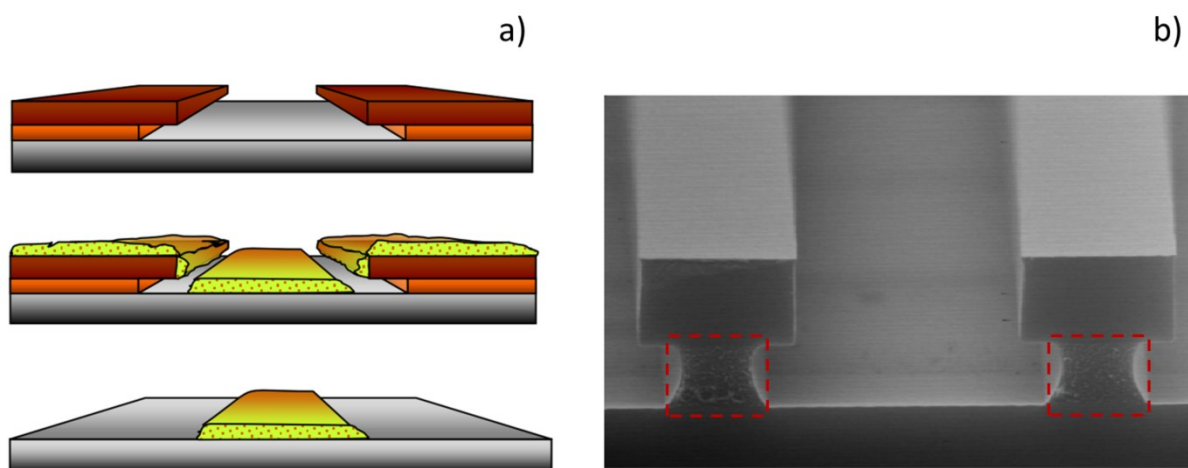


Figure 3.1.3 LOR assisted bilayer photoresist process for lift-off, a) Top: Photo resist (dark red) and LOR (orange) after exposure and developing. Center: Film deposition. Bottom: Deposited film on the material after lift-off, b) SEM image of bilayer resist with a wider window in LOR layer after developing. The dashed box marks the LOR layer. LOR exhibits excellent adhesion to GaAs ensuring the reliability for spin coating of additional resist [MICRO.CHEM].

Physical Vapor Deposition and Lift Off

After defining the contact regions by optical lithography, PVD is used for contacts metallization. Here, after cleaning the sample, LOR 5A resist is spin coated on the sample before adding S1800 series resist. The LOR ensures that an extended undercut window beneath the S1800 resist is created after developing as shown in figure 3.1.3. This resist bilayer generates as well-defined discontinuity/break-line of deposited metal on the sidewalls of the structured photoresist, which facilitates the lift off for metalized compound [MICRO.CHEM].

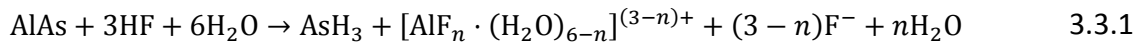
Before putting the sample into the vacuum chamber for metal deposition, the sample is cleaned by an O_2 plasma asher at maximum power for 120 seconds. To make Ohmic contacts, an Au/Ge compound is used. To make a top gate, Ti/Au compound is chosen. A 10 nm thin layer of Ti is evaporated directly on the GaAs substrate as an adhesive layer before the Au is evaporated.

Annealing

The deposition of a 40 nm layer of germanium and a 100 nm layer of gold is sufficient to make good electrical contacts. Immediately after the deposition of the Au/Ge compound and the lift-off, the sample is thermally annealed to form Ohmic contacts with the 2DES. A Rapid Thermal Annealing machine, RTA, with precise control of temperature is used to heat the sample to 430°C [R.JAF1945] for 300 seconds under the constant flow of forming gas (a mixture of Argon and Hydrogen). Before heating the furnace, the chamber is pumped and flushed several times to remove as much oxygen as possible to avoid oxidization. During the thermal annealing, the metal diffuses into the heterostructure and generates a surface doping that reduces the Schottky barrier and allows a linear current/voltage characteristic of the contacts as shown in Chapter 4.

Released Nanostructures

The release of the surface layers from the substrate by removing an embedded AlAs sacrificial layer can generate larger amplitudes in surface acoustic wave measurements. As discussed in Chapter 2, hydrofluoric acid has a high (selective) etch rate ratio of AlAs and $\text{Al}_x\text{Ga}_{1-x}\text{As}$ with x below 50%. During the etching process, escaping gas such as AsH_3 is detected using gas chromatography to monitor the etching of AlAs [J.SCH2005]. The reaction is described by



The released nanostructures might be damaged if too much reactive gas is formed. In addition, the formation of AsF_3 , i.e., white powder with low solubility, is able to prevent further reactions. Control of the etchant concentration and uniformity of etchant are important to obtain good results.

Figure 3.1.4 shows an inhomogeneously suspended structure obtained by undercutting the AlAs sacrificial layer. While I am currently able to release the whole width of Hall bar, the contact arms however have always been broken. Here, more tests of the etching parameters are necessary.

An alternative method to fabricate a released structure is *epitaxial lift off*, ELO (discussed in Chapter 2). In this method, the heterostructures above the sacrificial AlAs is completely peeled off after the HF etch using a temporary support layer/substrate, i.e., wax or photoresist [E.YAB1987].

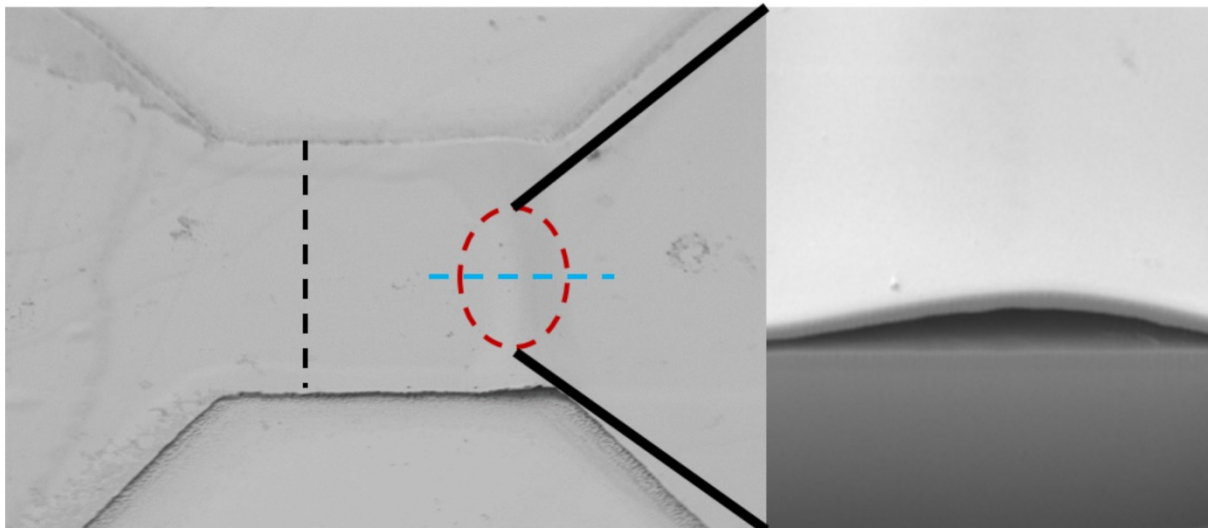


Figure 3.1.4 Scanning electron microscope image of a released nanostructure with Hall bar of 40 μm width (black dash line). The right insert is a blow up of the red circle diced along the blue line by Focused Ion Beam.

A released heterostructure membrane is shown in figure 3.1.5 a). The membrane is transferred to a glass/quartz substrate with holes as shown in figure 3.1.5 b) that are cut by a laser into MM200-Flex. The membrane will bond to the new substrate via van der Waals forces and will be suspended over the area of the holes. So far, I am able to transfer membranes of hundreds of micrometers in size to quartz substrate with holes as shown in figure 3.1.5 c). Currently, the success rate of the above process is very low and the freestanding structures on the new substrate are very fragile, making it difficult to add Ohmic contacts for measurements.

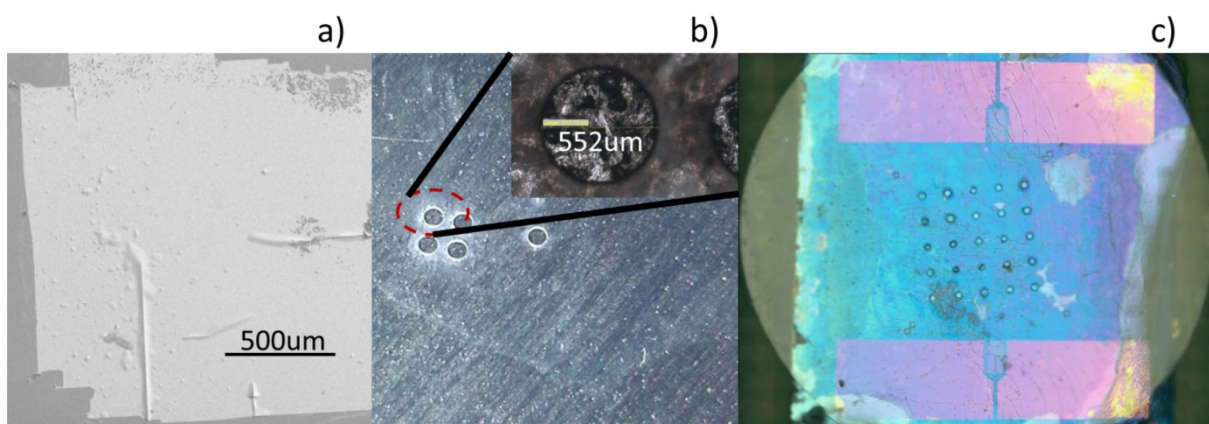


Figure 3.1.5 ELO method for obtaining freestanding nanomembranes on a glass substrate. a) The released membrane after the HF etch is transferred to a temporary support layer/substrate, b) Holes made in a glass substrate, c) Membrane in a) makes van der Waals bonds to the substrate.

3.2 Hall Bar Structures in Monolayer Graphene

I use commercially available CVD graphene, which is grown on copper foil as discussed in Chapter 2. Essential processing steps are the etching/removal of the copper and the cleaning of the graphene in order to obtain a good sample quality. The graphene layer needs to be transferred to a substrate and is further processed by optical lithography, pattern etching by PVD metallization. Figure 3.2.1 illustrates the crucial processing steps.

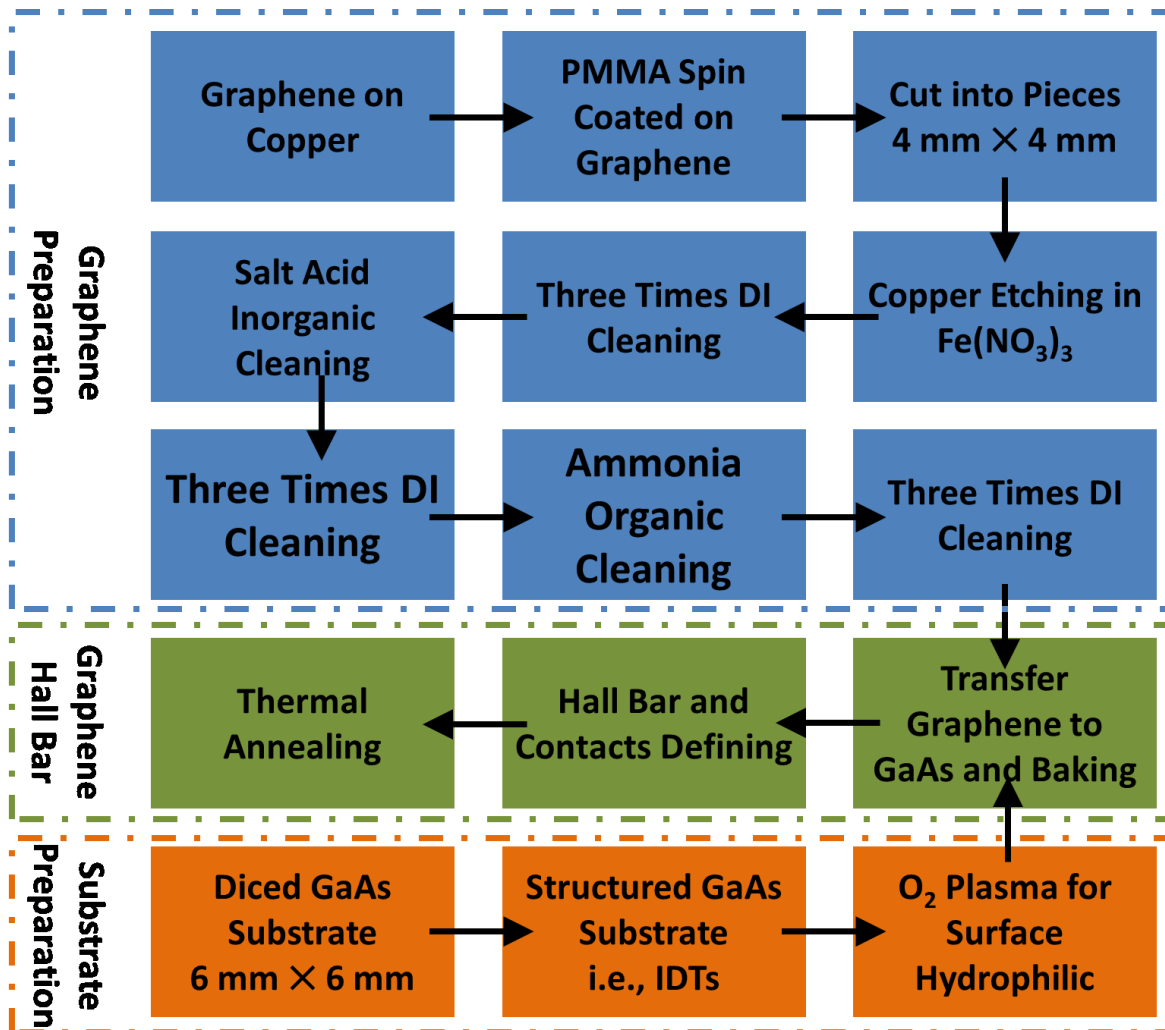


Figure 3.2.1 Process flow chart of graphene Hall bar sample on structured undoped GaAs. The dashed frame shows the three major processing steps, including graphene separation from copper and cleaning [T.LYON2017], substrate preparation, surface hydrophilic process by O₂ plasma and later transfer and the alignment of graphene to the metalized GaAs substrate for Hall bar fabrication.

Graphene Preparation

To make use of the commercial CVD graphene that is grown on copper, it needs to be released from the substrate. The release process starts by spin coating a piece of graphene on copper foil with Poly(methyl methacrylate), PMMA, on the graphene side. The PMMA supports the graphene for the following processes and enhances its visibility once it is released from the copper foil. Since monolayer graphene only absorbs 2.3% of light [R.NAI2008], the PMMA allows us to see it with the naked eye. I diced the PMMA/Graphene/Copper stack into $4 \times 4 \text{ mm}^2$ pieces and place the pieces with the copper side floating down into a solution of $\text{Fe}(\text{NO}_3)_3$ as shown in figure 3.2.2 a). Within approximately 12 hours, the copper will be completely etched away, leaving the PMMA/Graphene stack.

The exposed graphene interface is cleaned to remove inorganic residuals (with salt acid) and organic residuals (with ammonia). I follow the cleaning procedure described by Liang *et al.* [X.LIA2011]. After the copper is etched in $\text{Fe}(\text{NO}_3)_3$, the PMMA/Graphene is cleaned 3 times with deionized, DI, water ($\geq 10 \text{ M}\Omega$) by wet transfer. Then an $\text{HCl}/\text{H}_2\text{O}_2/\text{H}_2\text{O}$ (5:5:100 ml) etching solution is prepared for removing inorganic contaminations (duration 15 minutes), followed by additional three DI water cleaning steps. A $\text{NH}_4\text{OH}/\text{H}_2\text{O}_2/\text{H}_2\text{O}$ (1:1:100 ml) solution is used for removing organic contaminants, followed by three DI water cleaning steps [T.LYO2017T].

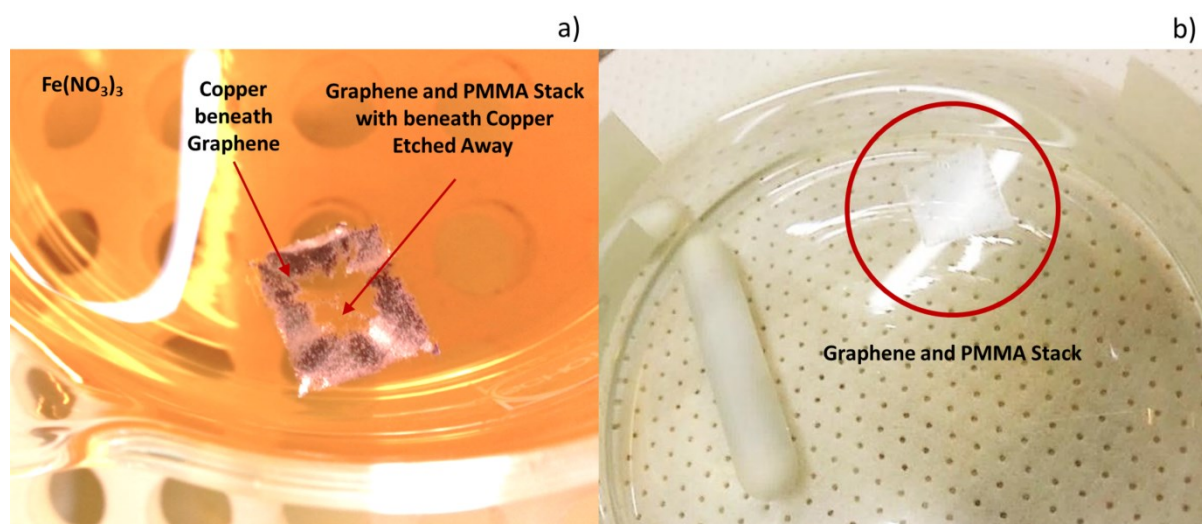


Figure 3.2.2 a) Copper etch in Iron(III) Nitrate leaves the PMMA /Graphene stack floating atop the solution, b) PMMA/Graphene floating atop DI water after cleaning with salt acid, ammonia and 6 times DI water (picture s permission from Sichau [J.SIC2015T]).

Graphene Hall bar on GaAs Substrate

The cleaned PMMA/Graphene piece floating atop the DI water as shown in figure 3.2.2 b) is transferred to a GaAs substrate. In order to make the GaAs surface hydrophilic and increase the adhesion of the graphene layer, the GaAs sample is treated with an O₂ plasma at maximum power for 300 seconds prior to the transfer. After scooping up and aligning the PMMA/Graphene stack with the center of the 6 × 6 mm² GaAs sample, the transferred sample is dried at 150 °C for 15 minutes. Afterwards the PMMA layer is removed in an acetone bath.

During the transfer process, the graphene layer can fold over, making it a double layer. Chapter 5 will discuss Raman spectroscopy measurements, with which I use to verify the transferred graphene is still monolayer.

Graphene Hall bars are defined by standard optical lithography similarly to the process for semiconductor samples. After the Hall bar geometry is patterned, an O₂ plasma treatment at maximum power removes/etches the graphene layer, which is not covered by the patterned photoresist. Ti/Au metal contacts are made by PVD using the previously discussed bilayer photoresist process.

Thermal Annealing

In contrast to semiconductor 2DES quantum wells, graphene is exposed to the ambient atmosphere and in direct contact with the substrate. Surface contaminations such as water or residuals from the PMMA can act as dopants. Prior to the low temperature measurements, thermal annealing steps are necessary to remove as many adsorbates and contaminations from the surface as possible.

The first thermal anneal is a 12-hour RTA bake under vacuum. After wire bonding the sample, I mount the sample to the probe, the sample is annealed in a MTI Corporate OTF 1200-X Instrument for a second time (≥ 48 hours) inside the probe connected to a rotary pump.

3.3 Interdigitated Transducers (IDTs)

Interdigitated transducers, as shown in figure 3.3.1, are used to generate surface acoustic waves that propagate along the 2DES confined in GaAs/AlGaAs heterostructures or monolayer graphene. The fabrication of IDTs with high linewidth resolution and reproducibility is important to generate homogeneous SAWs in our piezoelectric GaAs substrate.

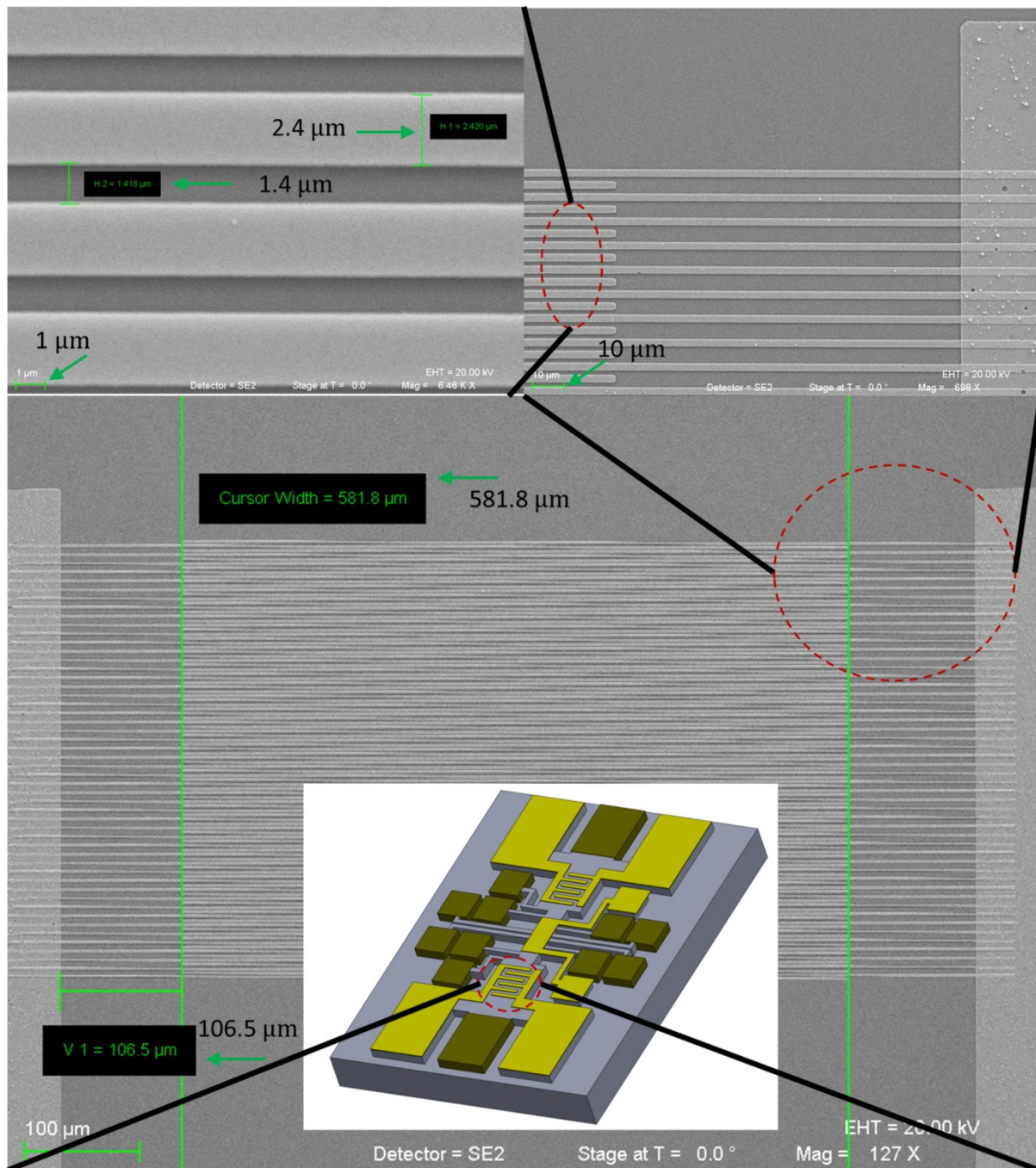


Figure 3.3.1 Scanning electron microscope image of our IDTs after patterning by EBL and metallization with PVD and lift off.

The IDT fingers are designed with a commercial software by RAITH and all electron beam pattern is done using a ZEISS SUPRA 55. I use a three-point alignment method based on predefined aligning markers to place the IDTs at the specific positions on the sample. During the EBL exposure, the electron beam follows the mask design of the software. The exposure parameters, such as area dose, dwell time and step size are adjusted for each new exposure to obtain well-defined IDT structures.

Due to the small feature size, the lift-off process after metallization is critical and may result in a destruction of the IDTs. To facilitate the lift-off, I have used a bilayer resist for EBL, similar to the one described for semiconductor structures. The bilayer resist used here is stack of PMMA with a molecular weight of 600 K (bottom layer) and 950 K (upper layer) which are recommended for high resolution by ALLRESIST GmbH [ALLRESIST]. After exposing by EBL, the bilayer resist can be developed in AR 600-55 to get patterned structures. The lift-off is done in AR 300-70 after PVD metallization.

Chapter 4

Measurement Infrastructure

The following chapter outlines the measurement instrumentation used in this thesis. The first section reviews the experimental setup, sample mounting, contacts testing and the basics of data acquisition. The next two sections give a brief description of the cryogenic setups, required for quantum Hall effects related measurements and discuss a home-built probe with wiring for electrical measurements and high frequency semi-rigid coaxial cables that terminate in a loop antenna at the sample stage.

4.1 Experimental Setup

All low temperature measurements are performed in helium bath cryostats with superconducting magnets (solenoid) that generate magnetic fields up to 8 Tesla. The samples are cooled down in a vacuum probe and lowered into the Helium bath. Because DC measurements are vulnerable to noise, a standard low frequency AC Lock-in method is used that allows detecting signals at very low signal-to-noise ratio (above 100 dB dynamic reserve). These AC measurements are performed with high precision Stanford Research SR830 DSP Lock-in amplifiers and Zurich Instruments HF2LI Lock-in Amplifier connected to a HF2TA Current Amplifier as shown in schematics of Figure 4.1.1. A home-made Python-based data acquisition software is used for device communication and data acquisition through a GPIB bus, connected to the computer via a National Instruments GPIB-USB-HS adaptor. Home-made breakout boxes are used to make the electrical connection between the probe/sample and the equipment with BNC cables.

After wire bonding of the sample on a chip carrier, the chip carrier will be plugged into a socket. For ESR measurements, both the socket and the chip carrier have to be cut on the side that faces the loop antenna; otherwise, this would partially shield the sample from the microwave radiation. The socket is mounted on the bottom of the probe as shown in figure 4.1.2. The stage where the socket is mounted is designed to allow different angles in respect to magnetic field direction (90°, 75°, 60°, 45°, 30°, 15°).

After a sample is mounted on the probe, it is electrically characterized at room temperature to check the contacts for Ohmic behavior by measuring I/V characteristics. Sample testing is done with a source measurement unit (SMU, Keithley 2400 Source Meter) by applying a small voltage to a sample contact while all other contacts are grounded on the breakout box. To prevent excessive high currents that may damage the sample, a maximum current limitation (compliance) is set based on the common contacts resistance (several kilo ohms).

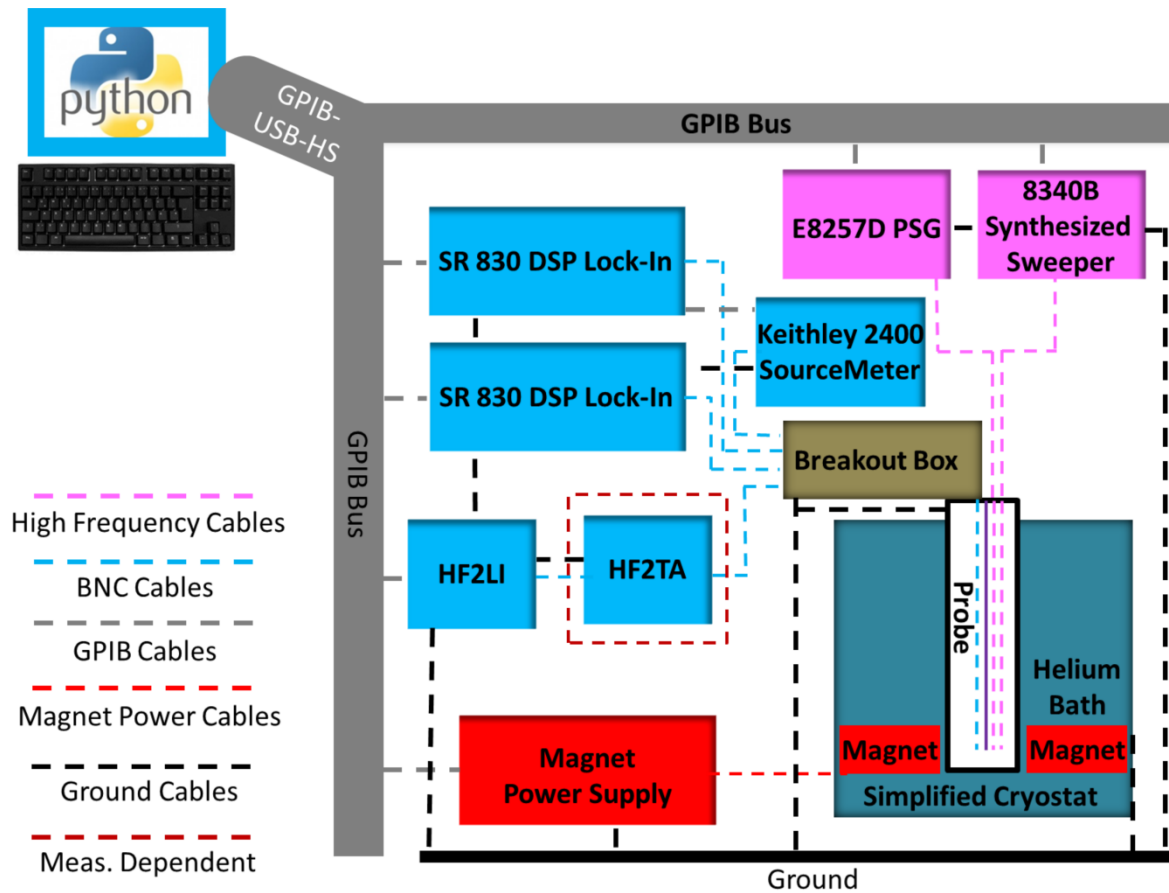


Figure 4.1.1 Schematic overview of the experimental setup. All devices are connected to a GPIB bus for controlling and data acquisition with the master computer. A low frequency AC sine reference is set to be $f = 37 \text{ Hz}$ ($T \approx 27 \text{ ms}$), and a time constant $T_c = 300 \text{ ms}$ (above $10 \cdot 1/f = 270 \text{ ms}$). A breakout box establishes electrical connection to the devices. “Meas. Dependent” (dark red dash line surrounding “HF2TA”) is only used for acoustoelectric current amplification.

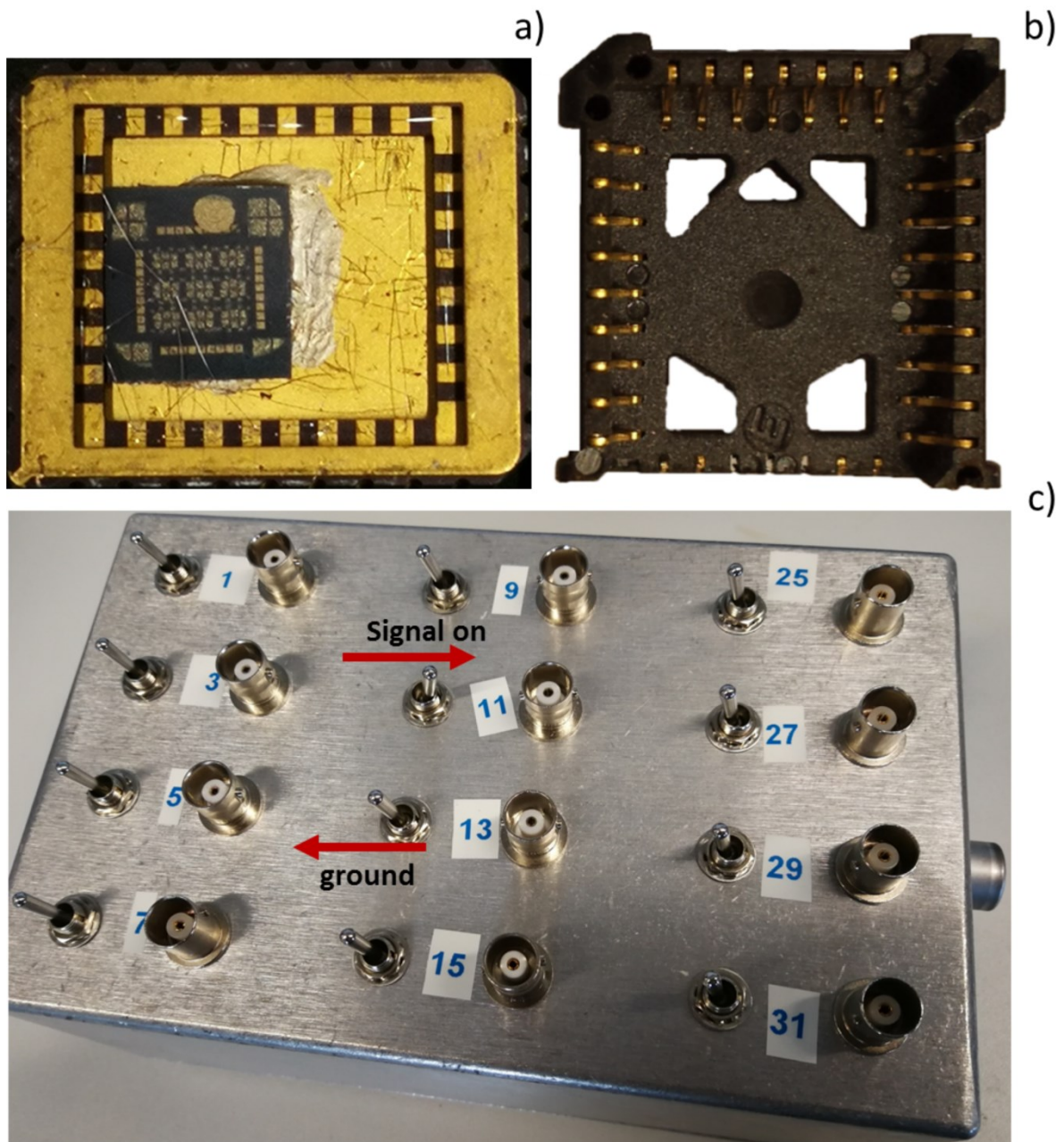


Figure 4.1.2 a) Exemplary sample, wire-bonded on a chip carrier, b) The socket used to hold the chip carrier shown in a). The bottom side is cut away to make allow microwave radiation to reach the sample from loop antenna, c) Home-made breakout box with switches to ground or connect the sample contacts.

Table 4.1.1 Typical currents and contacts resistance for a GaAs 2DES sample. The voltage applied by SMU is 1 mV.

	Current (nA)	Resistance (k Ω)
300 K and air	$\sim 180 - 350$	$\sim 3 - 5.5$
300 K and helium ex. gas	$\sim 150 - 330$	$\sim 3 - 6.5$
4.2 K and helium ex. gas	$\sim 900 - 2\,500$	$\sim 0.4 - 1.1$

Table 4.1.1 shows exemplary values for a typical GaAs 2DES sample at room temperature at ambient atmosphere, at room temperature with helium exchange gas, and at 4.2 Kelvin. Figure 4.1.3 shows an exemplary linear (and low resistance) I/V characteristic, which is required for low temperature magnetotransport measurements.

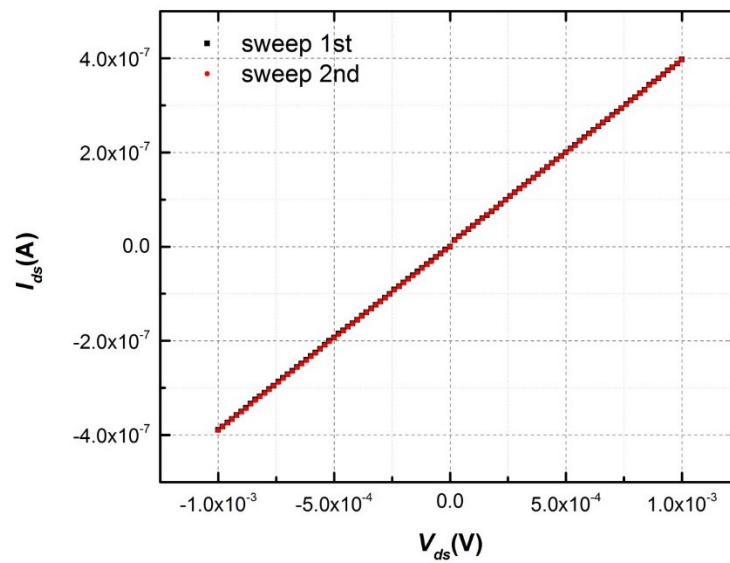


Figure 4.1.3 Exemplary I/V characteristic showing a linear behavior as required for quantum transport.

For measurements of the quantum Hall effects, a constant current is passed through the sample by putting a large resistor, usually 10 to 100 M Ω (i.e., much larger than the 2DES resistance and the contact resistances as determined above) in series to the sample which is directly connected the sine output of one (master) Lock-in Amplifier. The second Lock-in Amplifier is phase-locked to the master, so that longitudinal and Hall voltages can be measured at the same time while sweeping magnetic field. A schematic is shown in figure 4.1.4 demonstrating how the connection of a dual lock-in measurement is made. The gate voltage is applied with a Keithley 2400 Source Measurement Unit.

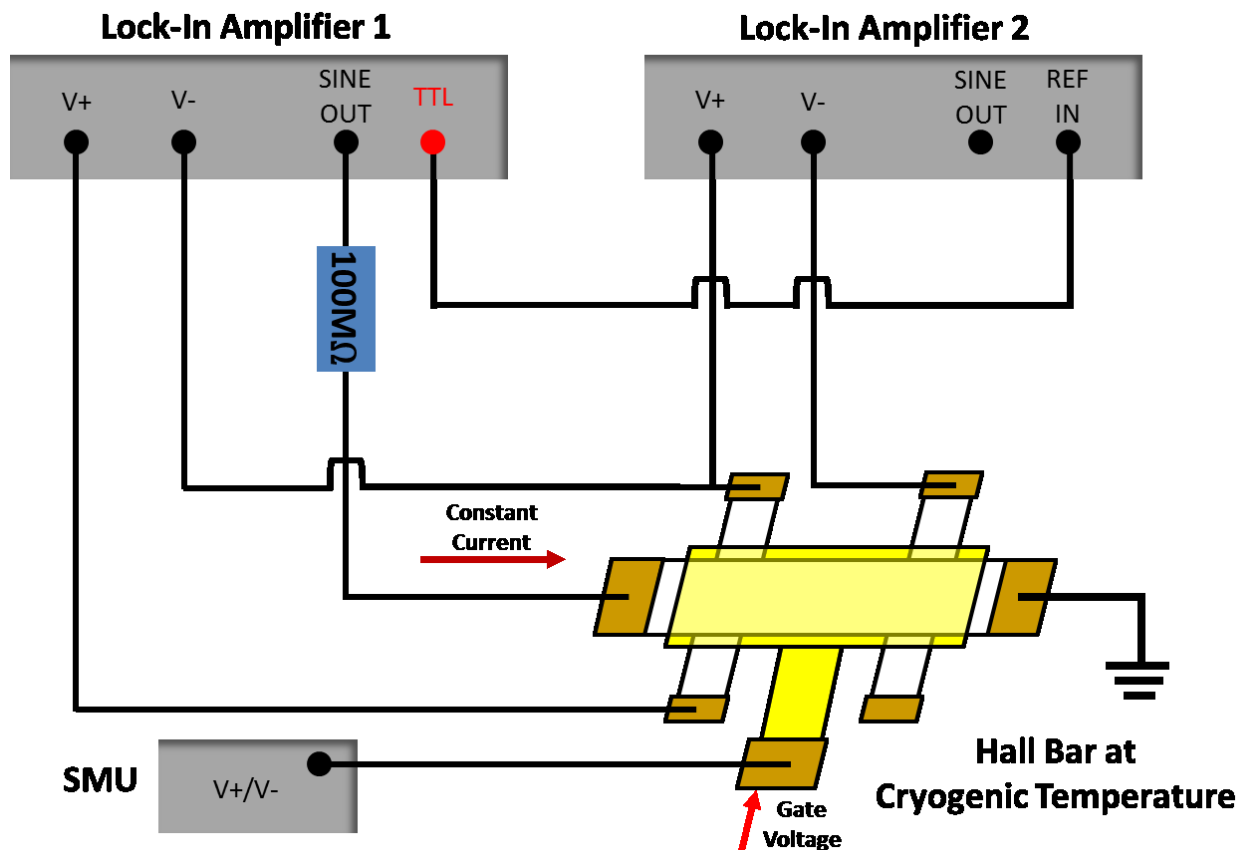


Figure 4.1.4 Double Lock-in Amplifier setup for standard magnetotransport measurements. Since the contact resistances are several kilo ohms as shown in table 4.1.1, the current flowing into the Hall bar is determined only by the in-series 100 M Ω resistor and can be regarded as a constant.

As discussed in Section 2.5, microwaves irradiated on a 2DES in a perpendicular magnetic field allow performing electron spin resonance and determining the Zeeman splitting. Microwaves are generated by a frequency generator (Agilent E8257D PSG Analog Signal Generator) at room temperature. A semi-rigid coaxial wire acts as a wave guide, which terminates in an isolated copper wire forming a loop coil antenna perpendicular to the effective external magnetic field as shown in figure 4.1.5. The antenna is located 3 to 5 mm next to the sample. The inductance of the antenna is estimated by [R.DEN2016]

$$L_{Loop} \cong N_{Loop}^2 \mu_0 \mu_r \frac{D}{2} \left(\ln \left(\frac{8D}{d} \right) - 2 \right) \quad 4.1.1$$

where N_{loop} is the number of loop turns, D is the diameter of the antenna loop, and d is the copper wire thickness. The calculated inductance is 32.8 nH.

The induced ac magnetic field from the loop antenna can be calculated for a sinusoidal electromagnetic wave as follows. The description of energy transport rate per unit area of microwave field can be described according to the Poynting vector

$$S = \frac{c_0 B_m^2}{2\mu_0} \quad 4.1.2$$

where B_m is the loop induced magnetic field, c_0 is the speed of light. For a microwave with power of P with spherical radiation center from the antenna

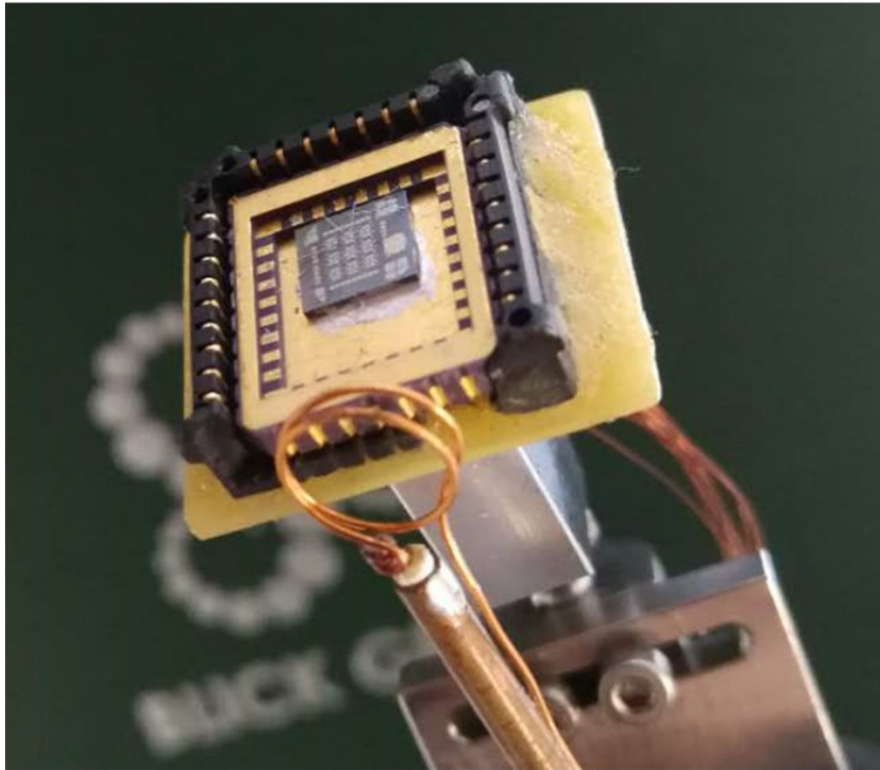
$$P = S * A \quad 4.1.3$$

$$B_m = \sqrt{\frac{\mu_0 P}{2\pi c_0 r^2}} \quad 4.1.4$$

where r is the distance between sample and copper wire loop. The estimated B_m is of the order of 1 μ T. Since our sample structures are much smaller than the loop diameter, we can regard the resulting electromagnetic field as approximately uniform impacting on the device under test.

As discussed in Chapter 2, the position of the ESR resonance with respect to the magnetic field is influenced by nuclear effects through the hyperfine interaction. To study this influence, we need to control the polarization of the nuclei. One possible approach is to utilize a second coaxial wire with a coil antenna as shown in figure 4.1.5 b) to depolarize the nuclei with a frequency that matches the nuclear Zeeman splitting.

a)



b)

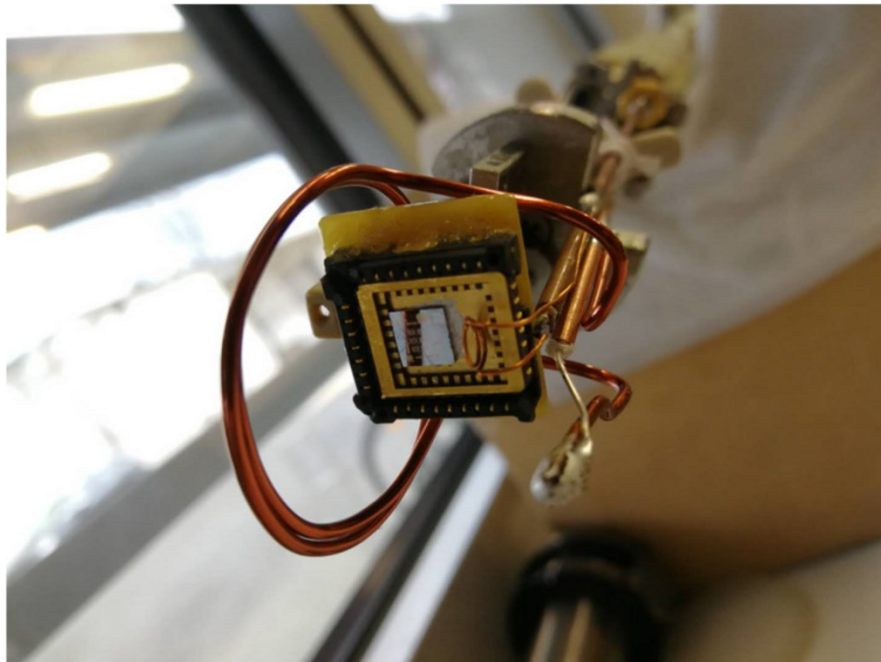


Figure 4.1.5 a) Photo of the loop antenna for ESR measurements, b) Modified antenna designed for the manipulation both nuclear spins (large antenna) and electron spin (small antenna).

The second semi-rigid coaxial wire is also needed for surface acoustic waves studies, discussed in Section 2.8. For these measurements, the coil is removed and the coaxial cable is directly connected to interdigitated transducers contacts located in the piezoelectric substrate. The IDTs convert the microwaves into a propagating electric field and mechanical wave along the surface of piezoelectric materials to manipulate the electrons and spins in the GaAs 2DES materials or graphene.

All our experiments requiring microwaves rely on two signal generators, that is, Agilent E8257D, ranging from 250 kHz to 67 GHz and Hewlett-Packards 8340B SYNTHESIZED SWEEPER, ranging from 10 MHz to 26.5 GHz, as shown in figure 4.1.1. Since the output of the E8257D has a 1.85/2.4 mm connector, an adaptor from 1.85/2.4 mm to 2.92/3.5 mm is used to convert the output to coaxial and semi-rigid cables (table 4.1.2 lists the frequency range for types of connectors used in the setups).

In this thesis, all data acquisition is performed by custom programs written in Python 2.6/3.7 to remotely control the instruments and to collect data. The Origin software package (OriginLab) is used for data analysis, curve fitting and plotting.

Table 4.1.2 Cutoff frequency for different types of connectors used in thesis. The connectors are named by the inside diameter of the outer conductor. Connectors of 1.85 mm and 2.4 mm are mounting compatible, connectors of 2.92 mm and 3.5 mm are mounting compatible [IEEE2007].

Connector Type	Cutoff Frequency
1.85 mm	73 GHz
2.4 mm	56 GHz
2.92 mm	46 GHz
3.5 mm	38 GHz

4.2 Cryogenic Systems

The cryostat that is used in the thesis is a liquid ^4He superconducting magnet system by Oxford Instruments with magnetic fields up to 8 Tesla at 4.2 K; a diagram is shown in figure 4.2.1. The helium main bath (reservoir) has a volume of 49 Liters. Under normal boil off conditions, the magnet is submerged in liquid helium and can be kept in a superconducting state for over 60 hours. The sample probe is cooled down by lowering it into the main bath and into the center field of the magnetic coil.

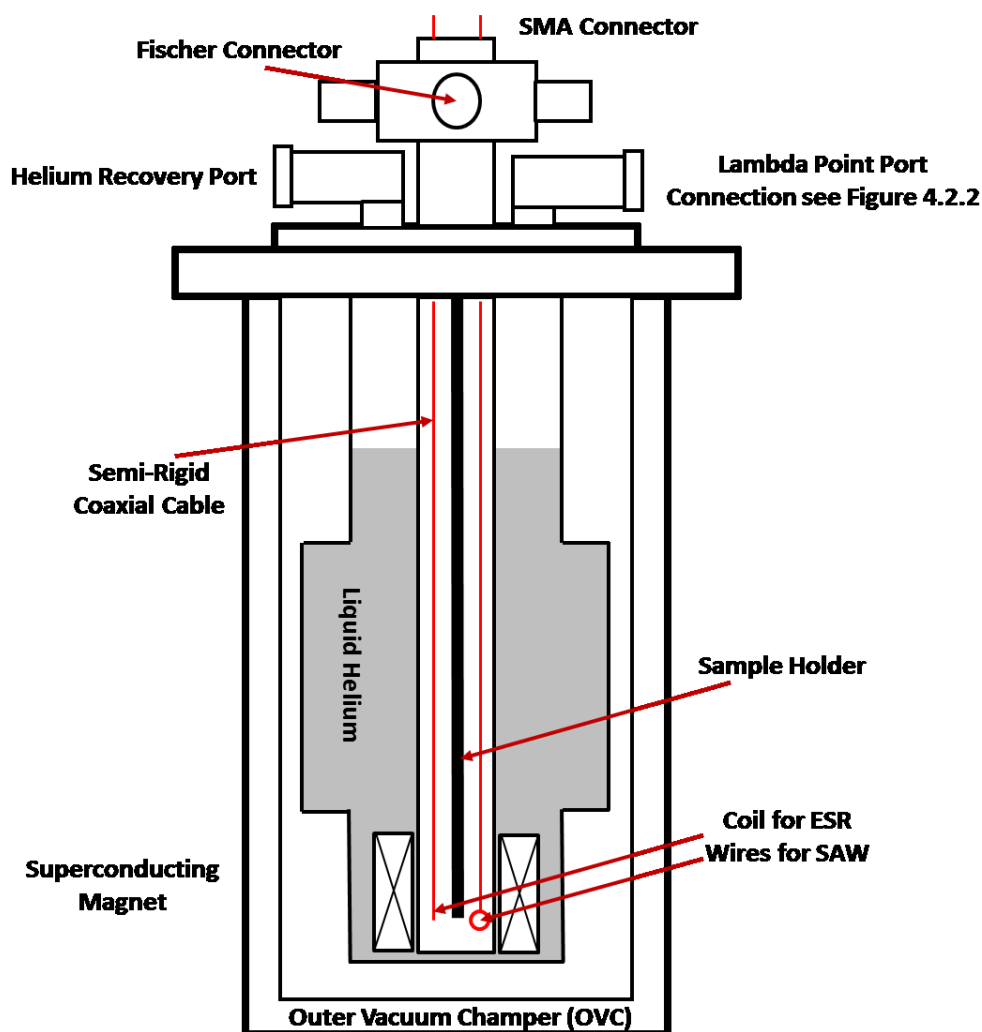


Figure 4.2.1 Schematic of helium bath cryostat with the probe inserted through the center of the magnet coil. The system is capable of 8 T at 4.2 K for normal operation and 10 T at 2.2 K for enhanced performance by lambda point refrigeration.

For some ESR measurements, lower temperature and higher magnetic field are required to increase the Landau level Zeeman splitting and/or to reach lower filling factors. For this purpose, the lambda point coil is pumped via a rotary pump to cool the helium bath down to approximately 2.2 K as shown in figure 4.2.2, allowing the magnet to maintain its superconducting state up to 10 T. Because of strong convection currents of liquid helium, helium moves down displacing warmer liquid around magnet. The bath temperature, which can be controlled by a needle valve that manipulates the flow rate, is monitored through resistance sensors (values are given in table 4.2.1).

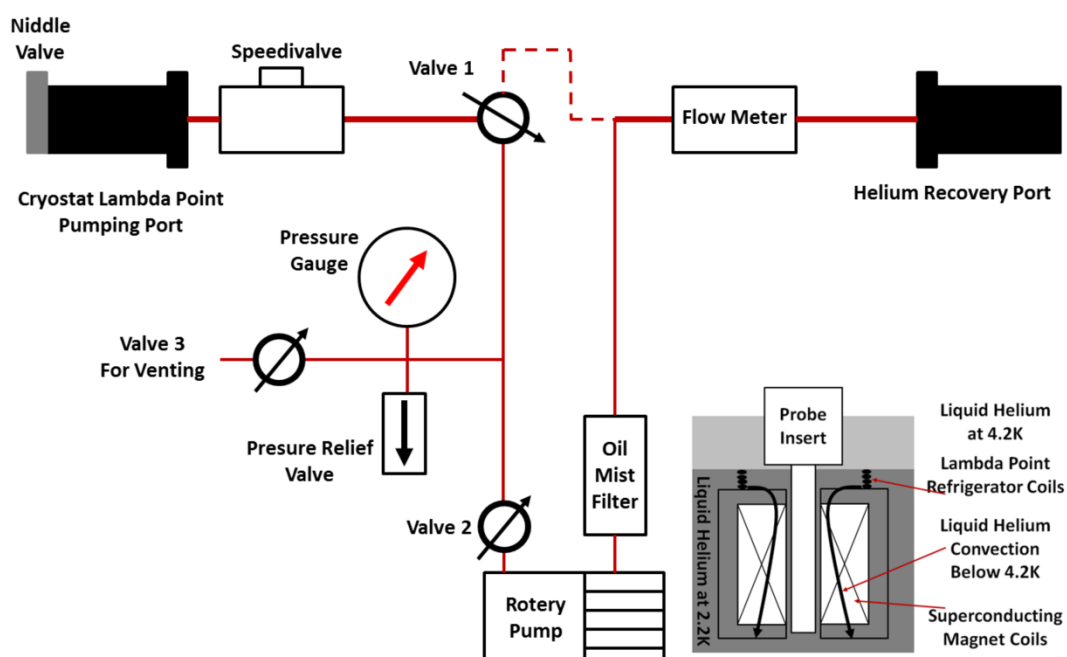


Figure 4.2.2 Schematic of the lambda point refrigerator pumping system. A rotary pump with capability of 80 m³ per hour pumps the lambda refrigerator. A pressure gauge is used to monitor the flow rate. It has to be noted that the pressure gauge should be as far as possible from the cryostat to prevent freezing. The lower right-hand inset shows the schematic of the lambda point refrigerator inside the cryostat.

Table 4.2.1 Lambda Point Refrigerator reference resistances. Allen Bradley Resistors R1, R2 and R3 are mounted 10 cm above the lambda refrigerator, directly on the refrigerator and on the magnet, respectively, to monitor the temperature. The time and resistance required to reach approximately 2.2 K are shown in bold [O.INS2005].

Elapsed Time (min)	Resistance R1 (Ω)	Resistance R1 (Ω)	Resistance R1 (Ω)	Pressure (mbar)
0	957	1057	1043	25
35	978	2585	2253	40
60	987	3690	3650	40
80	992	3700	3760	40

Some measurements are conducted in a (dry) *Triton* dilution refrigerator by Oxford Instruments, which was installed in our laboratory during the final year of this thesis. The system has a base temperature to 10 mK and achieves magnetic fields up to 12 T. Instead of using evaporation cooling of liquid ^3He and ^4He , the working principle of the dilution refrigerator is based on a mixture of ^4He and ^3He isotopes. Below approximately 0.9 K, the mixtures separate into two distinguishing phases, i.e., a lower heavier ^4He rich phase (bosons) with the lighter ^3He phase (fermions) on top as seen in phase diagram of figure 4.2.3. By pumping on a “Still” which is heated to approx. 0.6 K, only ^3He is removed from the dilute phase. Since the ^3He concentration in the dilute phase cannot fall below 6% (due to the different masses of the two isotopes and their binding energies), ^3He atoms from ^3He rich phase pass the boundary from a system with a higher energy (fermions) to a system of lower energy (mostly bosons). The cooling power can be calculated from the released energy as [C.ENS2005]

$$\int \Delta C_{\text{Helium}-3} dT \propto T^2 \quad 4.2.1$$

which is based on the big difference of the specific heats of ^3He in two phases due to concentration difference, $C_{\text{Helium}-3} \propto T/x_{\text{He}3}^{2/3}$. The efficiency of cooling with a mixture of the two isotopes is higher than evaporation cooling, which displays exponential temperature-dependence.

The ^3He gas is cycled back into the cryostat after precooling (in wet systems with a ^4He 1 K pot) with a heat exchange system and liquefaction through a constriction as seen in figure 4.2.3 b). The ^4He rich phase acts as an inert background because of its low vapor pressure and its bosonic nature.

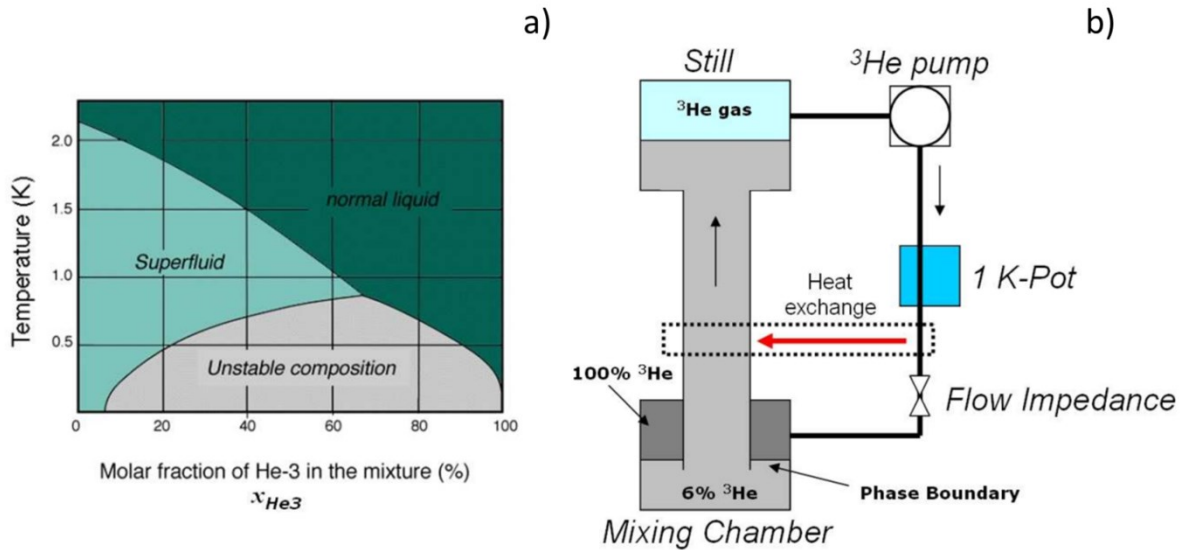


Figure 4.2.3 a) Phase diagram of ^3He and ^4He mixture, with at least 6% concentration of ^3He existing in mixture, b) Principle of dilution fridge with the ^3He cycle figure from [L.TIE2008].

4.3 Probe Design

I use a home-made probe that is compatible with the 4.2 K helium bath cryogenic system described in Section 4.2. The probe length is adjusted to the position of the magnet inside the main bath so that the sample is located in the center of the magnetic field. The probe is sealed in a vacuum-tight stainless steel tube. In addition to a regular twisted pair loom for electrical measurements, semi-rigid coaxial wires are guided along the spine, which terminate in SMA connectors at the head of the probe. These wires act as wave guides from microwaves in the ESR and SAWs measurements.

Before inserting the probe into the cryostat, it is evacuated to below 10^{-3} to 10^{-4} mbar to remove the ambient air and condensed water on the sample or the probe's interior. A small amount of helium exchange gas is added to the vacuum to enable a thermal contact between the (warm) interior and the helium bath in order to cool down the sample to 4.2 K (or to 2.2 K) and to maintain a stable temperature during measurements.

Since the probe, sealed by a stainless steel tube, is always under vacuum, a room temperature leak or a cold leak inside the He bath would lead to build up of (frozen) gases inside the probe. When the probe is warmed up, frozen air or liquid helium would lead a harmful and dangerous overpressure. To safely release potential overpressures, a pressure release valve is installed.

Two 18-pin Fisher vacuum feedthroughs are used to plug into the breakout box with 12 BNC connectors corresponding to contacts on the chip carrier. Inside the probe, the two Fisher connectors are connected to copper and constantan wires, which are soldered to female Micro-D-Sub connectors, located 100 mm above the sample position. The corresponding male Micro-D-Sub connectors are connected to copper wires, which lead to the pins of the sample socket. With the Micro-D-Sub connector design, it is possible to use either copper wires or the constantan wires along the spine of the probe in terms of thermal coefficients considerations.

For the measurements requiring microwaves, self-made SMA vacuum feedthroughs are connected to the head of the probe, as shown in figure 4.3.1. Semi-rigid coaxial wires with two SMA connectors on both ends act as wave guides inside the probe. RG-405 coaxial cables are chosen, which are made of silver plated copper-clad steel as center conductor, stainless steel as outer conductor and PTFE (Polytetrafluoroethylene) as the dielectric materials. Stainless steel has a low thermal conductivity to reduce the rate of heating dissipation from top to the bottom of the probe where a constant liquid helium temperature is required during measurements. The bandpass of the semi-rigid is around 20 GHz. For higher frequencies needed in the measurements, we compensate the attenuation by using a larger microwave power.

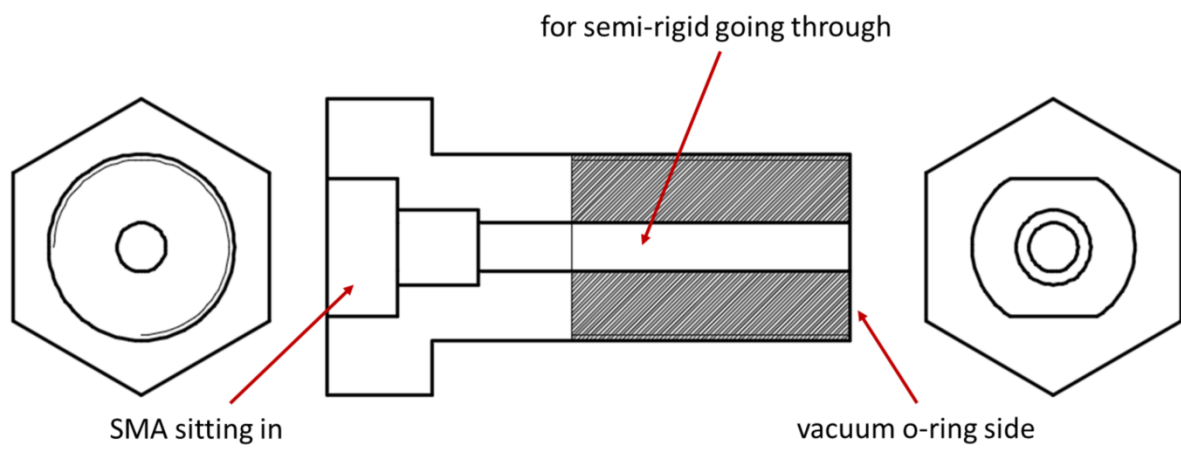


Figure 4.3.1 SMA vacuum tight seal schematic. The semi-rigid coaxial wire is fixed by a vacuum tight holder.

Chapter 5

Sample Characterization and Measurements

This chapter will introduce sample characterization and measurement methods. In the first half, I will focus on two-dimensional electron systems confined to conventional MBE-grown III-V GaAs semiconductor heterostructures. First, standard magnetotransport studies are shown which are then extended by resistively detected electron spin resonance (RD-ESR) experiments in which the sample is irradiated with microwaves. In the second half, I will concentrate on measurements performed on monolayer graphene Hall bar samples, which are transferred to a plane semi-insulating GaAs substrate. After the graphene samples are calibrated by standard magnetotransport, RD-ESR experiments are performed by either passing a regular constant ac current through the sample or an acoustoelectric current, generated by surface acoustic waves (SAWs).

5.1 Characterization of GaAs/AlGaAs Heterostructures

The measurements on three different GaAs/AlGaAs heterostructure samples will be discussed. Samples A and C are fabricated in the in-house clean room from heterostructures grown in the group of Prof. W. Hansen of the Univ. of Hamburg. Sample B is a high electron mobility transistor (HEMT) sample, grown in the group of Prof. W. Wegscheider at the ETH/Zürich. Other samples/wafers which were fabricated are listed in Appendix A.

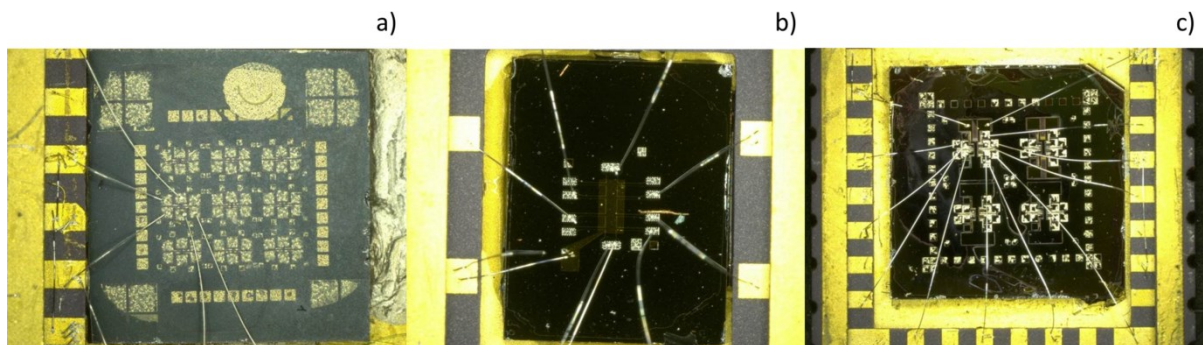


Figure 5.1.1 Three samples measured in the thesis. a) Hall bar sample without top gate and IDTs (sample A), b) Hall bar sample with top gate, but without IDTs (sample B), c) Hall bar structures integrated with IDTs (sample c).

Figure 5.1.1 shows photographic images of three Hall bar samples, wire bonded inside ceramic chip carriers (see chapter 4), which were measured at low temperatures. Regular contacts resistances at 4.2 Kelvin range between (1 – 4) k Ω . For the magnetotransport measurements, a constant current is passed through the sample in the longitudinal direction while the magnetoresistances can be calculated from the measured longitudinal and Hall voltage as a function of magnetic field. In our measurements, a constant ac current of 10 nA with 37 Hz, generated by the Lock-in Amplifier is used. From the longitudinal and Hall resistance the electron density and carrier mobility will be deduced.

Characterization of Sample A

Sample A is measured at different temperatures, with the results shown in figure 5.1.2. Clearly visible is the evolution from semi-classical characteristics at low magnetic field towards Shubnikov-de Haas (SdH) oscillations and integer quantum Hall effects at high magnetic fields, which are the result of the Landau level formation and Zeeman splitting [R.MEI2005]. For the integer quantum Hall effects regime, I am able to resolve odd (i.e., spin-split) filling factor at sufficiently low temperatures.

The carrier density can be calculated as

$$n = \frac{B}{e\rho_{xy}} = \frac{1}{1.6 \times 10^{-19} \times 1132} = 5.52 \times 10^{11} \text{cm}^{-2} \quad 5.1.1$$

We can further calculate the mobility with the above density,

$$\mu = \frac{1}{e n \rho_{xx}} = \frac{1}{1.6 \times 10^{-19} \times 5.52 \times 10^{11} \times 67.8} = 2.27 \times 10^5 \text{cm}^2 \text{V}^{-1} \text{s}^{-1} \quad 5.1.2$$

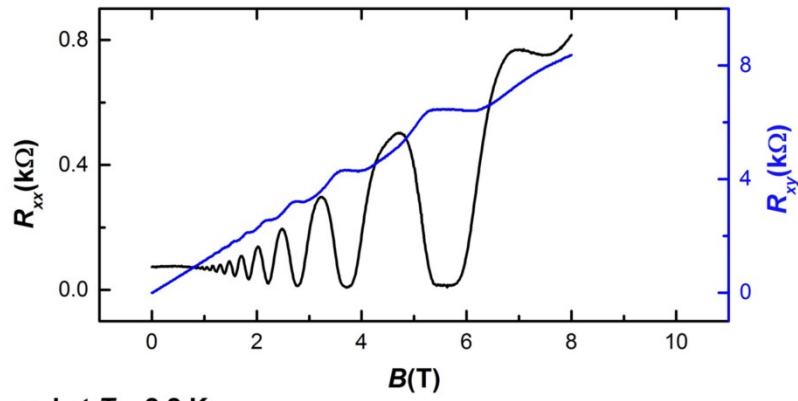
From the density and mobility, we can get the mean free path, $l_m = 278$ nm, in the sample.

Characterization of Sample B

Similar to sample A, a carrier density of $n = 1.75 \times 10^{11} \text{cm}^{-2}$ and the corresponding mobility of $\mu = 5.38 \times 10^6 \text{cm}^2 \text{V}^{-1} \text{s}^{-1}$ at 4.2 K are determined. Sample B was fabricated with a top gate as shown in figure 5.1.1, which is used to tune the carrier density. The changes in density can be observed as shifts in the magnetic field position of the minima in the longitudinal resistance oscillations as shown in figure 5.1.3.

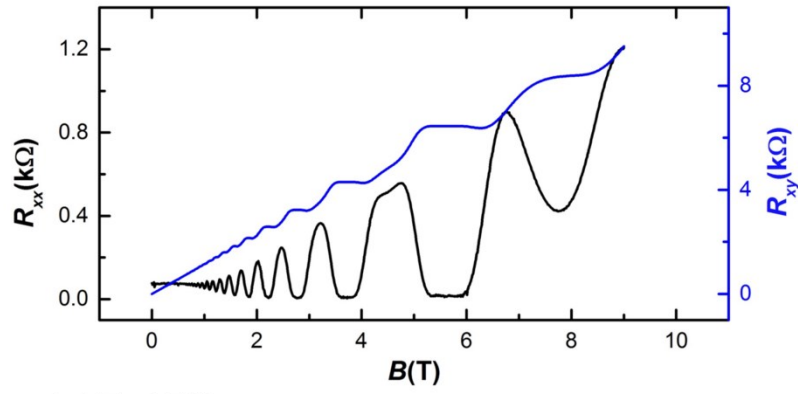
measured at $T = 4.2$ K

a)



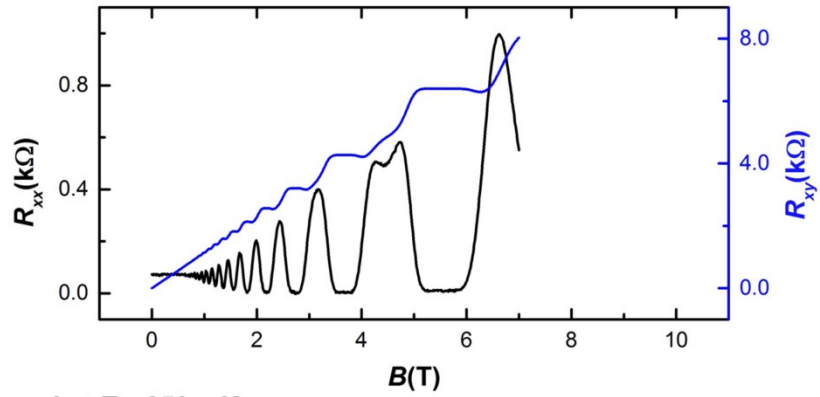
measured at $T = 2.2$ K

b)



measured at $T = 1.5$ K

c)



measured at $T = 250$ mK

d)

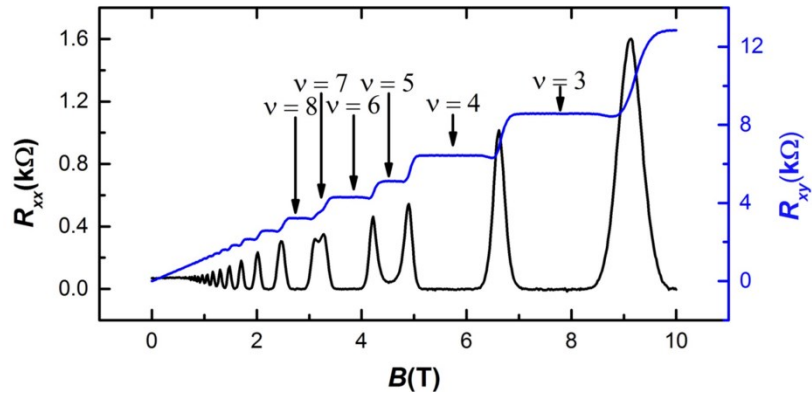


Figure 5.1.2 Sample A characterized at a) 4.2 K (Helium bath), b) 2.2 K (Lambda point refrigerator), c) 1.5 K (VTI), d) 250 mK (^3He cryostat).

measured at $T = 4.2$ K

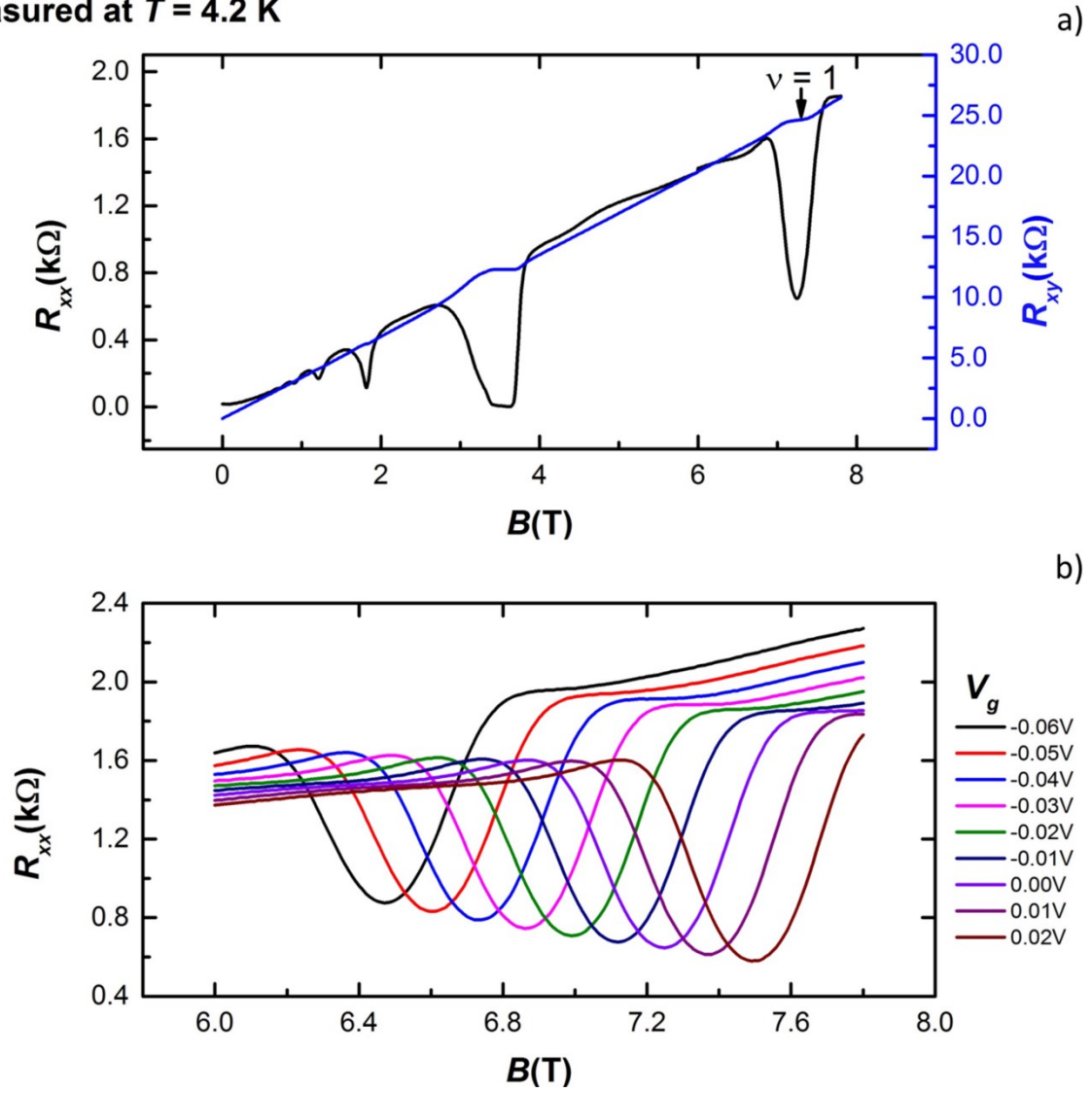


Figure 5.1.3 Sample B characterized at 4.2 K, a) With filling factor 1 at around 7.2 T and filling factor 2 at around 3.6 T, b) Evolution of filling factor 1 by tuning the gate voltage, the density changes from $1.81 \times 10^{11} \text{cm}^{-2}$ to $1.56 \times 10^{11} \text{cm}^{-2}$ between 0.02 to -0.06 Volts.

Characterization of Sample C

Sample C is designed for transport studies using surface acoustic waves. Figure 5.1.4 shows the longitudinal and Hall resistances up to 8 T at 4.2 K. No clear quantum oscillations or quantum Hall effects are visible. This is possibly related to the quality of the materials itself or a non-optimal contact arm configuration/geometry, which differs from regular Hall bars due to the use of SAWs and the released process.

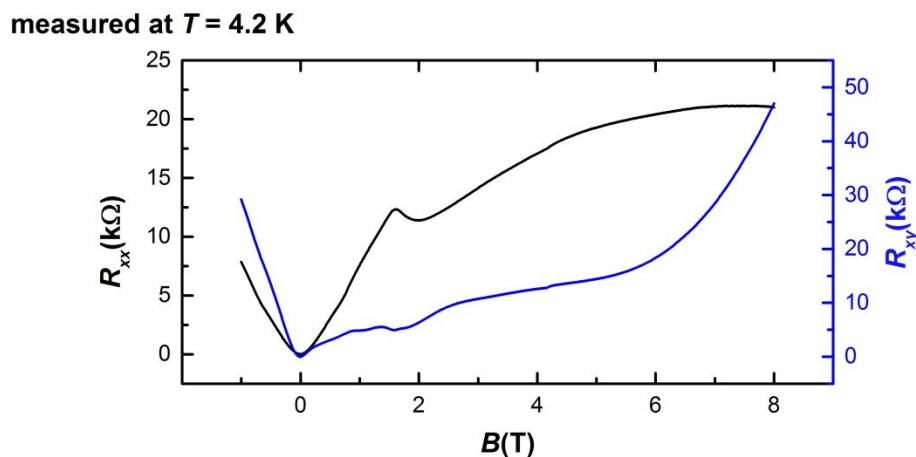


Figure 5.1.4 Sample C, designed for SAWs measurements characterized at 4.2 K, shows no quantum Hall effects.

5.2 Electron Spin Resonance in GaAs/AlGaAs Heterostructures

In this section, I will show the results of ESR experiments on 2DEs in GaAs/AlGaAs heterostructures. As discussed in Section 2.5, the Zeeman splitting, which is observed at odd filling factors, can be probed by microwave irradiation when the energy of the electromagnetic waves match the Zeeman splitting energy. The induced electron spin flips are detectable as changes in the magnetoresistance. For ESR experiments, I will focus on sample A and Sample B since they exhibit quantum Hall effects and minima in the longitudinal resistance at odd filling factor, as discussed in Section 5.1. Two SR830 Lock-in Amplifiers are used for the magnetoresistance measurements, and an Agilent E8257D signal generator is used to generate microwaves up to 67 GHz. All measurements shown in this

section are performed in a helium bath cryostat at 4.2 Kelvin under a perpendicular magnetic field with respect to the sample. Figure 5.2.1 shows a schematic of the setup with the coil being orthogonal to the sample and external magnetic fields.

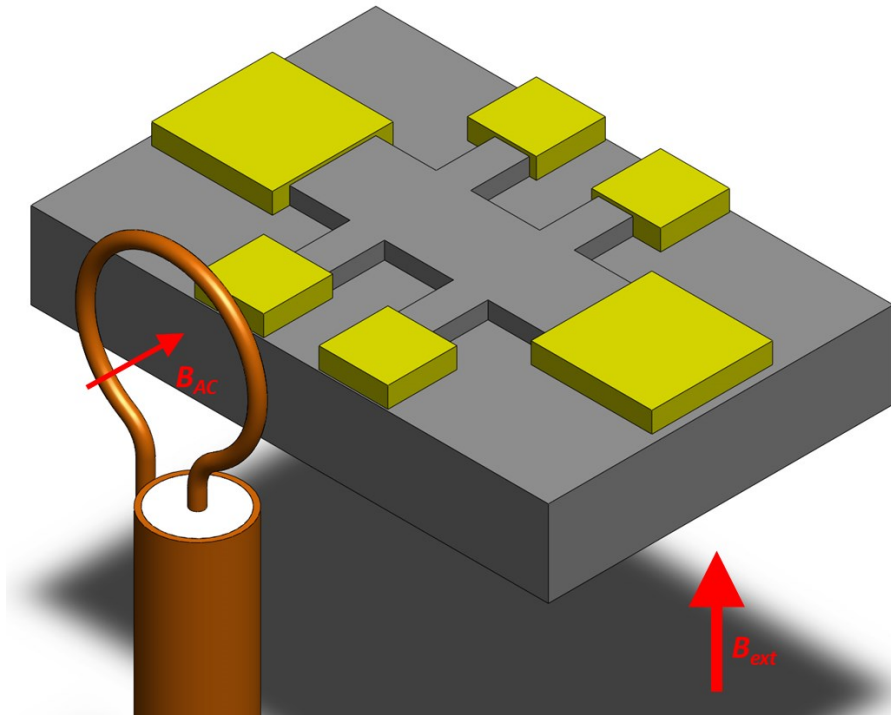


Figure 5.2.1 Schematic setup for ESR measurements. An external magnetic field B_{ext} is applied perpendicular to the sample plane. The microwave AC field is perpendicular to B_{ext} . Yellow areas represent Ohmic contacts.

ESR Performed on Sample A

The magnetotransport measurements shown in figure 5.1.2 indicate the positions of all experimentally accessible odd filling factors for ESR, i.e., $\nu = 7$ at 3.18 T, $\nu = 5$ at 4.54 T and $\nu = 3$ at 7.72 T as well as a general temperature-dependence (i.e., the thermal activation with $k_B T$). Since the effective g -factor of electrons in the 2DES confined to a GaAs quantum well can differ from -0.44 due to wave function overlap into the barrier and since the Zeeman energy splitting can also be influenced by nuclear effects, the electron spin resonance frequencies have to be determined by *trial and error*. While sweeping the magnetic field from 0 T to 8 T, a constant frequency in the range between 5 GHz to 60 GHz with a constant power (between several milliwatts to several hundreds of milliwatts) is applied.

Under microwave irradiation, heating thermally activates electrons so that the minima in the longitudinal resistance become less pronounced. For certain frequencies, however, additional resonant features are observed at a filling factor of 5 and a filling factor of 7 as shown in figure 5.2.2 a) and b). The relative resonance position for 10 GHz and 12 GHz will be explained later in terms of the hyperfine interaction. The simple model of Zeeman splitting implies the existence of a single resonance frequency for each magnetic field value. However, in addition to resonances found at 10 GHz and 12 GHz (each at a specific field), a full resonance spectrum could be observed, showing various distinct resonances. Figure 5.2.3 summarizes the magnetic field positions for the different resonance frequencies observed for filling factors 5 and 7. For up sweeps of the magnetic field, resonances are found in the range between 4 T and 5 T for $\nu \sim 5$. For $\nu \sim 7$, resonances are found in the range between approx. 3 T and 4 T for down sweeps. As figure 5.2.3 demonstrates, the resonance positions for the up sweep and down sweep are different even for the same frequency. In the following, I will further study and explain this behavior by focusing on the range between 3 T and 5 T for specific frequencies.

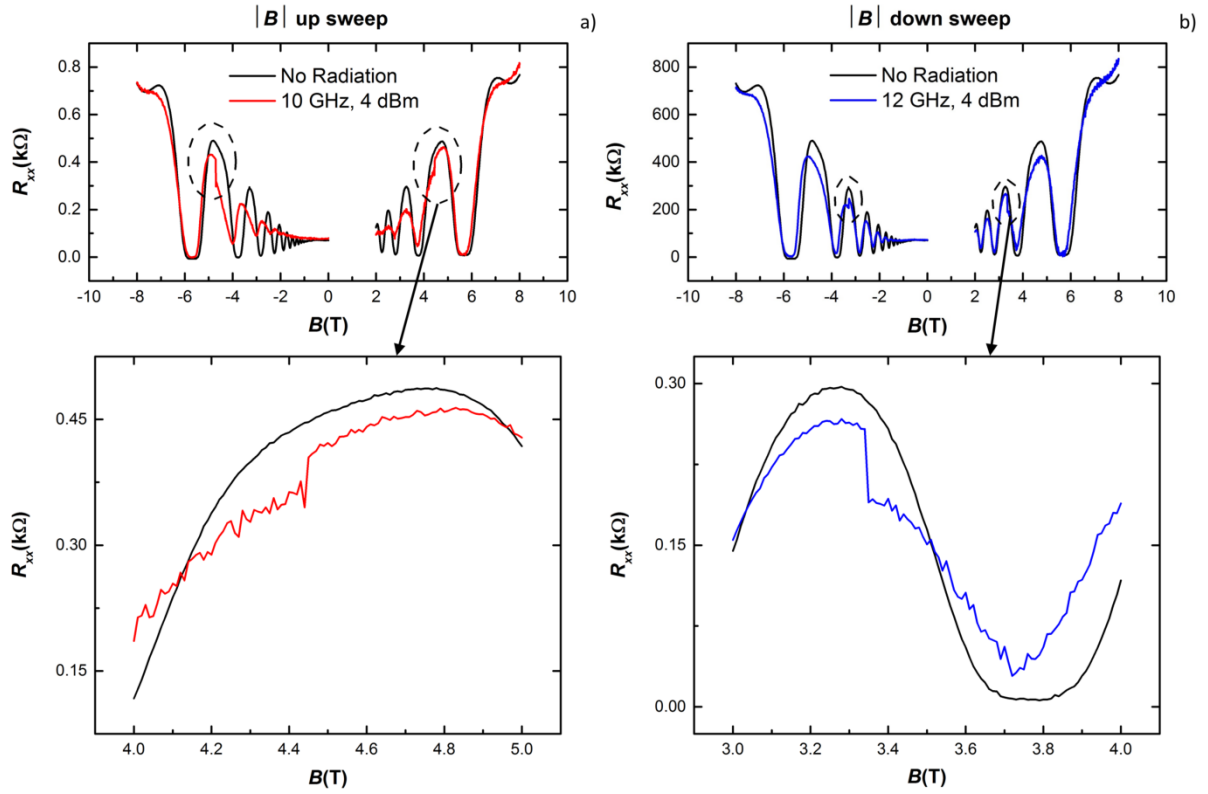


Figure 5.2.2 The solid black line is a sweep without radiation. For 10 GHz a) with magnetic field sweeping from low magnetic fields to high magnetic fields, a resonance is observed at filling factor of 5. For 12 GHz b) with magnetic field sweeping from high magnetic fields to low magnetic fields, the resonance is seen at filling factor of 7.

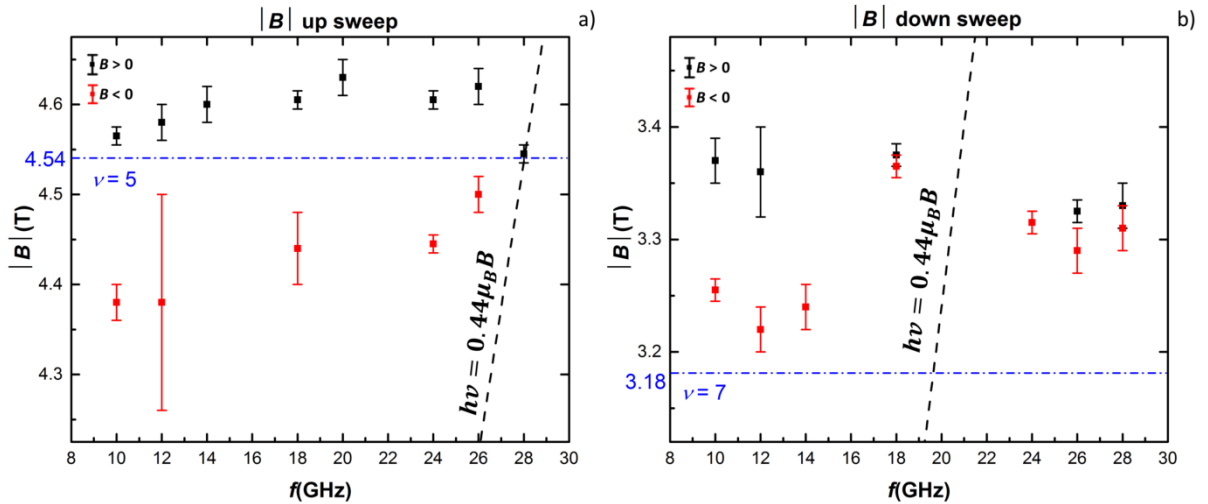


Figure 5.2.3 Comparison of the absolute resonance positions for all the frequencies with $|B|$ up sweep a) and down sweep b). The black dash line is a guide calculated with g -factor of bulk GaAs, -0.44.

I. Effective g -factor and Resonance Frequency

The effective g -factor in GaAs is -0.44, however, experimentally it often strongly differs from this expected value, as discussed in Chapter 2 [M.DOB1988]. The resonances around filling factor 5 (figure 5.2.3) can be used to calculate the effective g -factor in our sample using the method described in Ref. [M.DOB1988]. According to Equation 2.5.5, the effective (corrected) g -factor in sample A is,

$$g^*(B_{=4.54\text{T}}, N_{=2}) = g_0 - c \left(N + \frac{1}{2} \right) B = 0.4 - 0.0115 \times \left(2 + \frac{1}{2} \right) \times 4.54 = 0.27 \quad 5.1.1$$

With this calculated effective g -factor of -0.27, the expected resonance frequency at 4.54 Tesla (i.e., filling factor of 5), is approx. 17.2 GHz, while for the expected g -factor of -0.44 it would be approx. 28 GHz. Very close to this estimated value of 17.2 GHz, i.e., at 18 GHz, a resonance is indeed seen in experiment (figure 5.2.4). However, since we observe various resonances, the estimated deviation of the effective g -factor alone cannot explain this behavior.

B up sweep

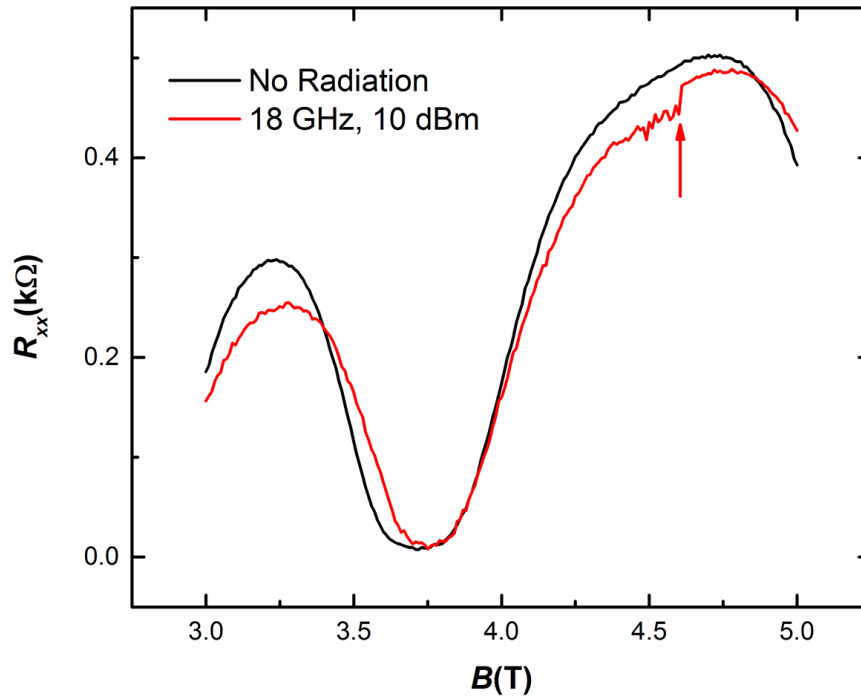


Figure 5.2.4 Spin resonance at 18 GHz near filling factor of 5.

II. Appearance of Various Resonances

Figure 5.2.3 has demonstrated that for a small magnetic field range around odd filling factors, many resonances can be observed. Figure 5.2.5 illustrates the emergence of these resonances for two exemplary microwave excitation frequencies of 10 GHz and 12 GHz. When the magnetic field is swept up, a resonance transition from a state of lower resistance to a state of higher resistance is seen around filling factor of 5 for 10 GHz [subfigure a), red curve]. In a subsequent down sweep, however, the resistance remains high when crossing $\nu = 5$. A transition back to the original state of low resistance occurs at filling factor of 7 [subfigure b), blue curve]. This phenomenon is reproducible as shown in subfigure b). When the sample is irradiated with microwaves of 12 GHz, the directions of the resonant transitions at filling factor of 5 and 7 are reversed. That is, in an upsweep, the sample resistance drops at $\nu = 5$ and in the following downsweep, the resistance returns to its original state of higher resistance at $\nu = 5$ as shown in figure 5.2.6.

III. Line Shape and Hysteresis

Figure 5.2.7 is a blow-up of the resonant transitions, demonstrating that the transition for both 10 GHz and 12 GHz are step-like with a very large slope. Figure 5.2.7 a) also shows that the magnetic field position of the transition slightly shifts for repeated measurements. The shift is probably related to the build-up of a nuclear (Overhauser) field induced by our ESR measurements that modifies the electron resonance condition via the hyperfine interaction between nuclear spins and electron spins. As discussed in Chapter 2, the nuclear spin polarization increases when electrons flip their spins during a resonant absorption (i.e., ESR) due to the conservation of energy and momentum through the hyperfine interaction (flip-flop processes). This enhanced nuclear spin polarization results in a nuclear magnetic field, B_N , called Overhauser field. Consequently, the effective magnetic field seen by the electrons consists of two parts and can modify the Zeeman splitting and the resonance condition for ESR as

$$E_{phonon} = h\nu = g_e^* \mu_B B_{eff} = g_e^* \mu_B (B_{ext} + B_N) \quad 5.2.3$$

Assuming the (corrected) effective g -factor of our GaAs 2DES materials is approximately -0.27 as previously calculated, the resonant position for 10 GHz will be around 2.76 Tesla (corresponding to a filling factor of 8) instead of around 4.7 T (corresponding to a filling factor of 5). However, considering an Overhauser field, which can reach up to 5.3 T in GaAs [D.PAG1977] at low temperatures, it is feasible that 10 GHz can still induce a resonant transition at around 4.7 T (i.e., at a filling factor of 5).

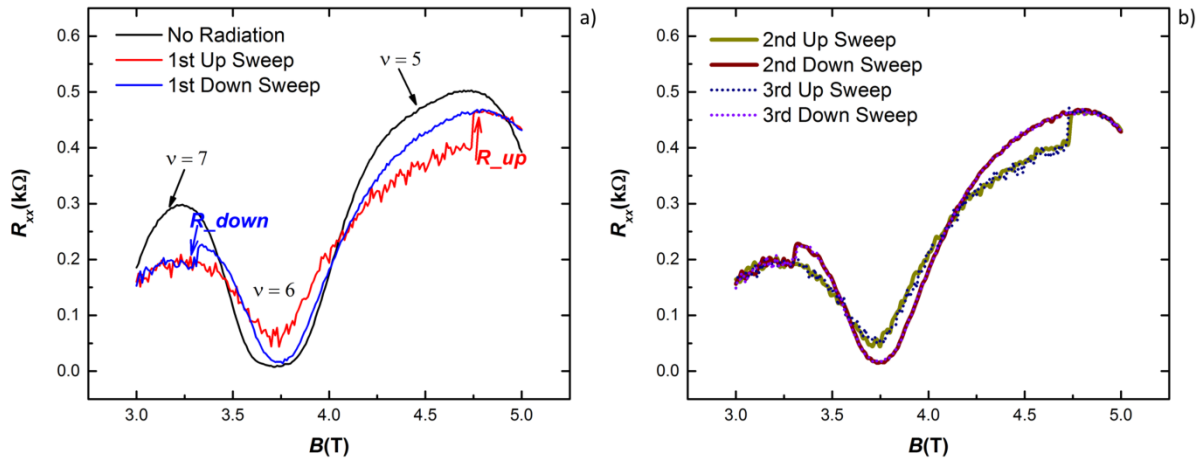


Figure 5.2.5 Magnet field sweeps under 10 GHz and 4 dBm, a) A resonance transition from a state of lower resistance to a state of higher resistance at a filling factor of 5 in a up sweep (red curve) and the reverse transition at a filling factor of 7 in a subsequent down sweep (blue curve), the red and blue arrows indicate the direction of the transition, i.e., from low (high) to high (low) resistance state, b) Reproducibility of the phenomenon.

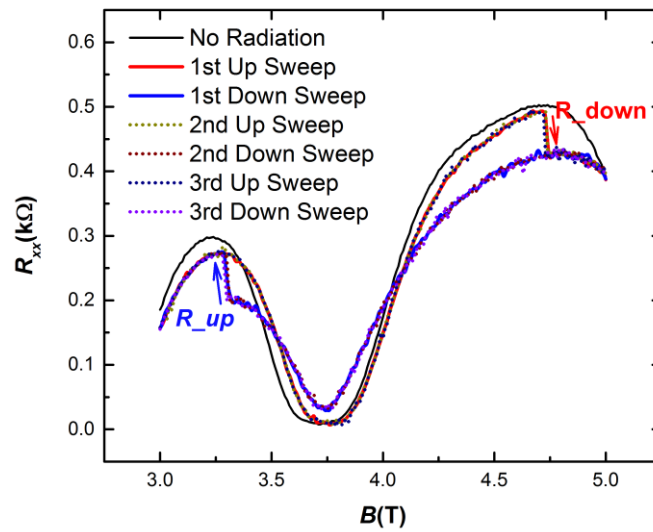


Figure 5.2.6 Repeated up and down sweeps of the magnetic field under 12 GHz and 4 dBm. While the resonant transition appears at approximately the same filling factors, the direction, however, is reversed. At filling factor of 5, the resonant transition for the up sweep is now from a state of higher resistance to a state of lower resistance as the red indicator shows.

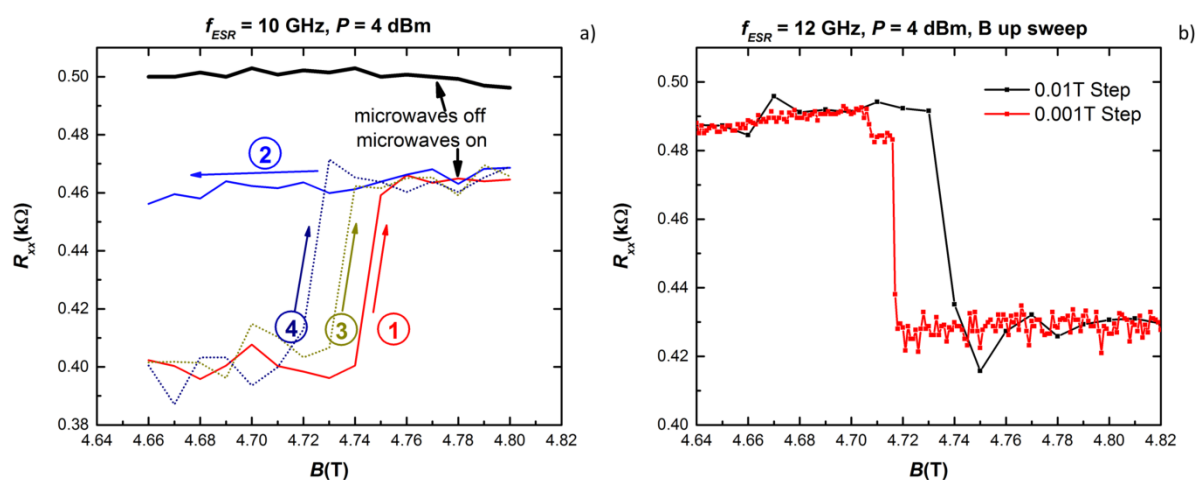


Figure 5.2.7 Blow-up of the resonant transition near odd filling factors. a) Three consecutive up sweeps under 10 GHz compared to a single corresponding down sweep and the dark condition. The numbers indicate the order of the measurements, b) Magnetic field range around the $\nu = 5$ for two up sweeps under 12 GHz with coarse (10 mT) and fine (1 mT) step size with the measured data point shown by dots. Both plots show a shift of resonance.

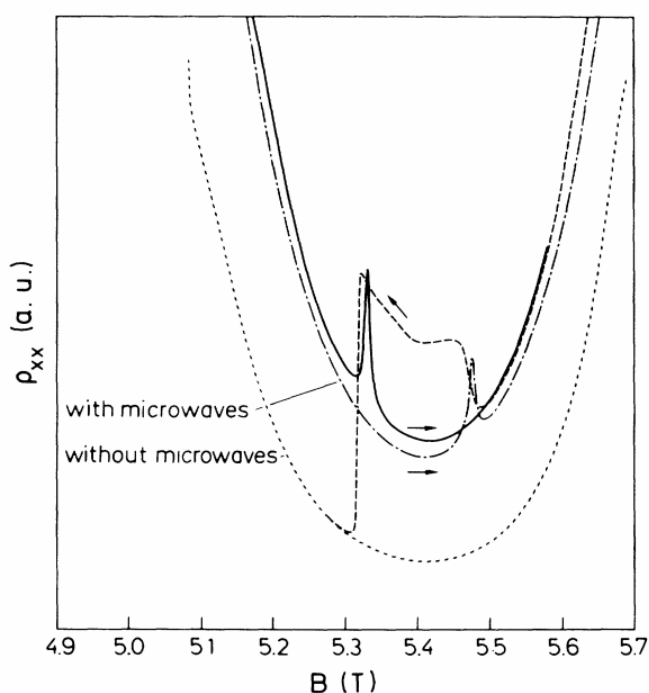


Figure 5.2.8 A similar hysteresis and shift was observed in Ref. [M.DOBE1988], which was attributed to an Overhauser shift.

As discussed in Section 2.5, a GaAs quantum well consists of 60.1% ^{69}Ga , 39.9% ^{71}Ga , and ^{75}As all having a nuclear spin quantum number of 3/2. The total Overhauser shift created by the nuclear spin polarization is a sum of spin polarization for each type of isotope with its natural abundance taken into account in $b_{N,i}$. Using equation 2.6.1 [Y.LI2008], the Overhauser shift can be calculated from

$$\mathbf{B}_{N,all\ isotopes} = \mathbf{B}_{N,Ga-69}\langle I \rangle + \mathbf{B}_{N,Ga-71}\langle I \rangle + \mathbf{B}_{N,As-75}\langle I \rangle \quad 5.2.4$$

The product of $B_{N,i}\langle I \rangle$ is the Overhauser shift for each isotope which can be found in table 2.5.1. With $\langle I \rangle = -3/2, -1/2, 1/2, 3/2$, we obtain

$$\mathbf{B}_{N,all\ isotopes} = -0.91\langle I \rangle - 0.78\langle I \rangle - 1.84\langle I \rangle \quad 5.2.5$$

Tables 5.2.1., 5.2.2. and 5.2.3. show the theoretical nuclear Overhauser fields in Tesla for the Gallium and Arsenide isotopes, according to the assumption in Equation 5.2.5.

The (idealized) theoretically calculated magnetic field \mathbf{B}_N created by a nuclear spin polarization differs from the experimentally observed Overhauser shifts. While the calculated maximal field is about 5.3 Tesla, Dobers *et al.* instead found 0.2 Tesla (at 4.2 K and 5.5 Tesla). Since the nuclear spin splitting is very small even at high magnetic fields, temperature increases or microwave-induced heating easily depolarizes the nuclei thus reducing \mathbf{B}_N .

In the simple model discussed by Dobers *et al.* [M.DOBE1988], the nuclear polarization should increase through ESR by means of the hyperfine interaction and flip-flop processes. This is in contrast to what is observed here, i.e., a shift of the resonance to lower fields after repeated ESR measurements. An increase of the nuclear polarization can also not explain the reversed resonant transition at lower magnetic field at around a filling factor of 7. Since published reports of similar observations did not exist and to better understand the phenomenon, it is planned to deliberately depolarizing the nuclei using NMR.

Table 5.2.1 Individual Overhauser shift of the three isotopes of GaAs, units in Tesla (temperature unspecified) [M.DOBE1988, Y.LI2008]

	$\langle I \rangle: -3/2$	$\langle I \rangle: -1/2$	$\langle I \rangle: 1/2$	$\langle I \rangle: 3/2$
^{69}Ga	1.365	0.455	-0.455	-1.365
^{71}Ga	1.17	0.39	-0.39	-1.17
^{75}As	2.76	0.92	-0.92	-2.76

Table 5.2.2 Overhauser shift created by the Gallium isotopes, units in Tesla.

	⁶⁹ Ga, -3/2, 60.1%	⁶⁹ Ga, -1/2, 60.1%	⁶⁹ Ga, 1/2, 60.1%	⁶⁹ Ga, 3/2, 60.1%
⁷¹ Ga, -3/2, 39.9%	-2.535	-1.625	-0.715	0.195
⁷¹ Ga, -1/2, 39.9%	-1.755	-0.845	0.065	0.975
⁷¹ Ga, 1/2, 39.9%	-0.975	-0.065	0.845	1.755
⁷¹ Ga, 3/2, 39.9%	-0.195	0.715	1.625	2.535

Table 5.2.3 Total Overhauser shift in GaAs, units in Tesla.

	⁷⁵ As, -3/2	⁷⁵ As, -1/2	⁷⁵ As, 1/2	⁷⁵ As, 3/2
⁷¹ Ga, -3/2, ⁶⁹ Ga, -3/2	-5.295	-3.455	-1.615	0.225
⁷¹ Ga, -3/2, ⁶⁹ Ga, -1/2	-4.385	-2.545	-0.705	1.135
⁷¹ Ga, -3/2, ⁶⁹ Ga, 1/2	-3.475	-1.635	0.205	2.045
⁷¹ Ga, -3/2, ⁶⁹ Ga, 3/2	-2.565	-0.725	1.115	2.955
⁷¹ Ga, -1/2, ⁶⁹ Ga, -3/2	-4.515	-2.675	-0.835	1.005
⁷¹ Ga, -1/2, ⁶⁹ Ga, -1/2	-3.605	-1.765	0.075	1.915
⁷¹ Ga, -1/2, ⁶⁹ Ga, 1/2	-2.695	-0.855	0.985	2.825
⁷¹ Ga, -1/2, ⁶⁹ Ga, 3/2	-1.785	0.055	1.895	3.735
⁷¹ Ga, 1/2, ⁶⁹ Ga, -3/2	-3.735	-1.895	-0.055	1.785
⁷¹ Ga, 1/2, ⁶⁹ Ga, -1/2	-2.825	-0.985	0.855	2.695
⁷¹ Ga, 1/2, ⁶⁹ Ga, 1/2	-1.915	-0.075	1.765	3.605
⁷¹ Ga, 1/2, ⁶⁹ Ga, 3/2	-1.005	0.835	2.675	4.515
⁷¹ Ga, 3/2, ⁶⁹ Ga, -3/2	-2.955	-1.115	0.725	2.565
⁷¹ Ga, 3/2, ⁶⁹ Ga, -1/2	-2.045	-0.205	1.635	3.475
⁷¹ Ga, 3/2, ⁶⁹ Ga, 1/2	-1.135	0.705	2.545	4.385
⁷¹ Ga, 3/2, ⁶⁹ Ga, 3/2	-0.225	1.615	3.455	5.295

As discussed in Chapter 4, this can be done by adding a second coil to the experimental setup to excite and depolarize the nuclei while simultaneously performing the ESR measurements. Table 2.5.1 shows the required nuclear Overhauser fields in Tesla for the Gallium and Arsenide isotopes. If the nuclei can be depolarized, repeated ESR transition without shifts should be observable. However, after the sample was warmed up for the installation of the second antenna, the effect could not be reproduced. This is very likely related inhomogeneities of the 2D electron system and the impact of temperature on the spin splitting as seen in figure 5.1.2 a). It is possible that each cool down yields a different configuration of “puddles” of varying density, varying filling factors and/or varying polarization, which may favor various resonant transitions.

To enhance the spin-splitting in the longitudinal resistance and to potentially boost the ESR signal, the sample temperature was reduced to 2.2 K by using the lambda point refrigerator and later to 1.5 K in a VTI cryostat as shown in figure 5.1.2 b) and c). While this indeed enhanced the separation between spin up and spin down Landau levels, it was still insufficient to obtain a stable and reproducible ESR signal to study the effect of nuclear (de-)polarization.

ESR Performed on Sample B

Figure 5.2.9 shows additional electron spin resonance measurements performed on a high electron mobility sample in a different liquid helium bath cryostat at 4.2 K (with only one coil available). See Section 5.1 for sample details and characterization. Instead of appearing at an odd filling factor, resonant peaks are observed around a filling factor of 2 for specific frequencies. Similar to sample A, the resonance shifts with repeated sweeps of the magnetic field.

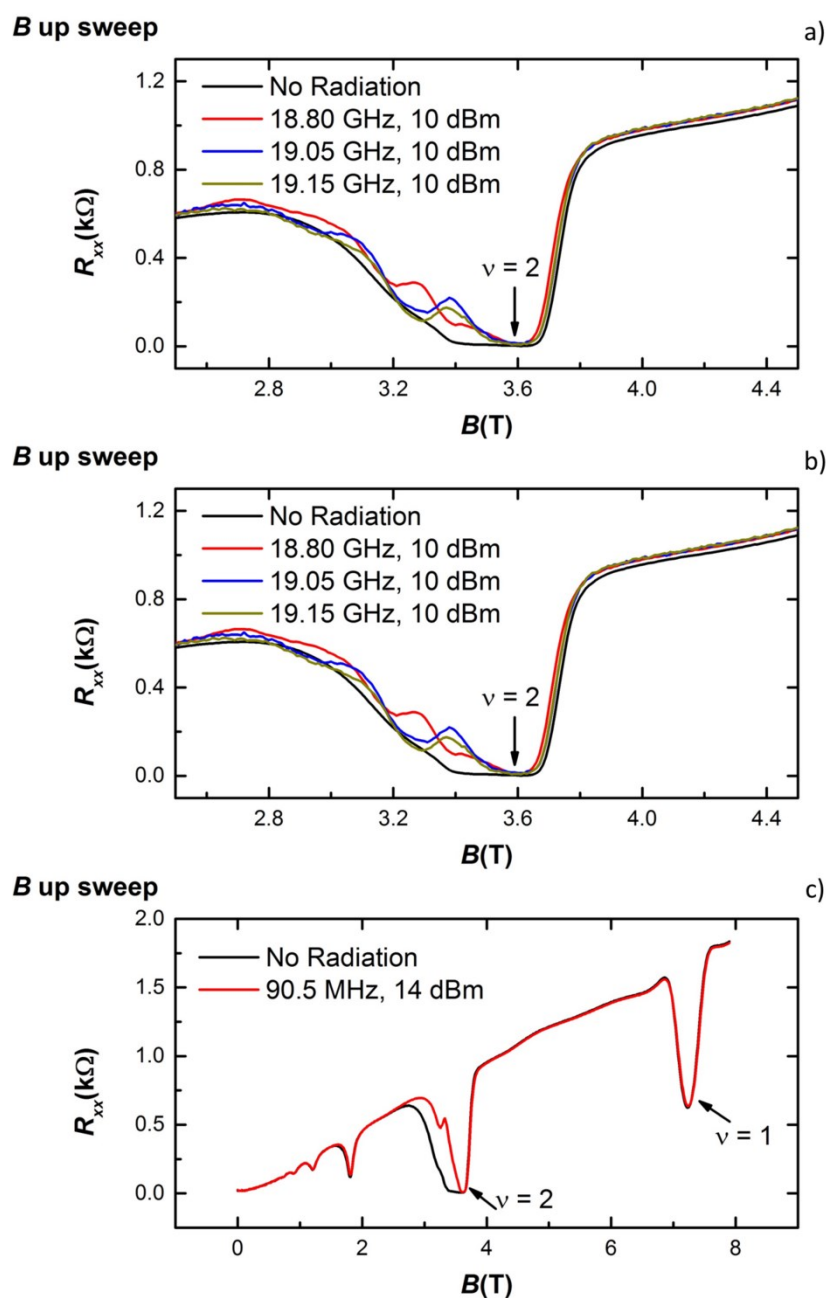


Figure 5.2.9 a) ESR measurements with excitation frequencies around 19 GHz, b) Repeated ESR measurements with 19.15 GHz show a shift in the resonant position, c) Anomalous NMR peak appearing for 90.5 MHz.

To study the influence of the nuclear field in a cryogenic system equipped with one coil, two methods can be used: (1) the modulation of the (electron spin) microwave excitation in the GHz range with (nuclear) excitations in the MHz range, or (2) a seesaw-like measurements scheme in which the frequency range is rapidly switched between MHz (NMR) and GHz (ESR). Since the modulation frequency of our signal generator cannot exceed 2 MHz (which is more than one order magnitude smaller than required for nuclear magnetic resonance, as shown in table 2.5.1), the second method was tested.

This scheme to study the nuclear polarization and to perform NMR is based on the rapid change between the two frequency ranges and the assumption that the nuclear spin diffusion times are sufficiently long:

- i. around the fixed magnetic field position B_i of an ESR transition, the corresponding microwave resonance frequency f_{ESR} is applied for t_1 seconds to polarize the nuclei via electron spin flips.
- ii. application of f_{NMR} that matches the theoretical nuclear resonance frequency for t_2 seconds.
- iii. Repeating i. and ii., while keeping f_{ESR} constant but incrementing f_{NMR} by a fixed step of several kHz until f_{NMR} has covered the expected range of the nuclear resonance.

Steps i. through iii. are repeated with slightly different f_{ESR} and/or magnetic fields. The expectation is that the nuclear polarization, induced by flip-flop electron-spin-nuclear-spin processes during ESR would generate a strong NMR signal at a specific f_{NMR} . This frequency could then have been used to deliberately depolarize the nuclei during the ESR measurements. However, after various measurements with different parameter tests, it is not possible to see the expected results. This is possibly related to the low magnetic field, the high temperature of 4.2 K and a short nuclear spin diffusion time, which prohibits stable nuclear polarization.

Nuclear magnetic resonance is also tested at the high-magnetic field flank of the filling factor of 1 resistance minimum by sweeping f_{NMR} . For the magnetic field position of $\nu = 1$ approx. 7.2 Tesla, the expected NMR resonance frequency of the ^{71}Ga isotopes is around 93 MHz. surprisingly however, a peak was not observed at $\nu = 1$ but instead around the low-magnetic field flank of the filling factor of 2 as shown in figure 5.2.9 c).

When a gate voltage is applied to tune the carrier density, additional anomalous effects and peaks appear. Figure 5.2.10 shows some examples. The origin of all these anomalous phenomena is not clear, however, it is likely that the ESR and NMR peaks around $\nu = 2$ are not related to spin excitations but simply result from a temperature induced coupling between the $\nu = 1$ and $\nu = 2$ edge channels that mimic a resonant excitation. When a gate voltage is added, the edge channels in the ungated contact arms and the gated active regions do not align, which may show up as measurement artifacts such resonant transitions or density changes. Therefore, the study of this sample was concluded. However, appendix

A proposes additional plans and new sample designs to study the effect of nuclear polarization on electron spin resonance in the future.

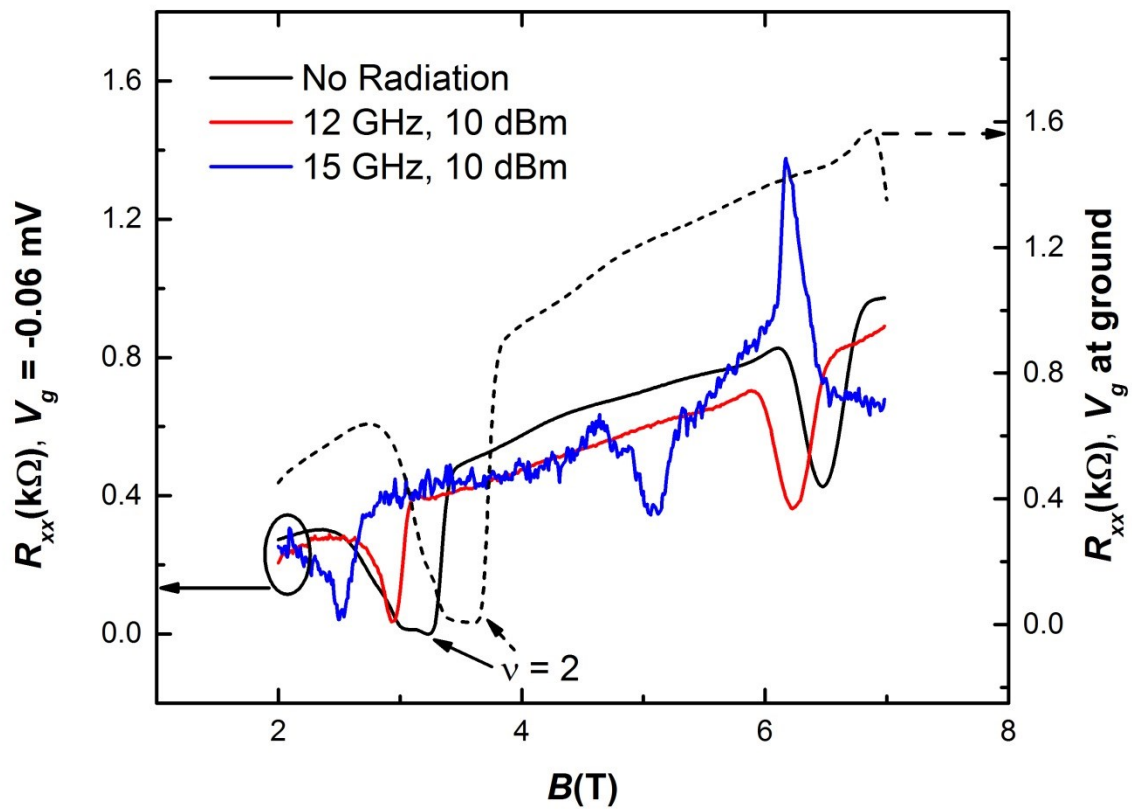


Figure 5.2.10 Application of a gate voltage of -60 mV. Under microwave irradiation, anomalous additional density changes or peaks are seen. The dashed line shows a sweep with the gate grounded (right y-axis)

5.3 Surface Acoustic Wave induced Current in a Two-Dimensional Electron System

The complete measurement setup to excite and study surface acoustic waves is shown in figure 5.3.1 a). The interdigitated transducers fabricated on sample C are wire-bonded by aluminum wires to the chip carrier, which connect via semi-rigid coaxial cables to a radiofrequency signal generator (SG) that excites SAWs and acoustic currents. The radiofrequency signal generator (SG) is amplitude modulated (AM) by an external connection using the reference frequency from a Lock-in Amplifier, which acquires a measurement signal will be maximum at the resonance frequency of the IDTs as discussed in Section 2.8. The principle of this method is based on the modulation of the output signal by a periodic reference, which is used to excite the SAWs, as shown in figure 5.3.2. The reference will also be used for the measurement of the generated acoustic signal by the Lock-in so that the applied signal and measured current or voltage have a common phase relation.

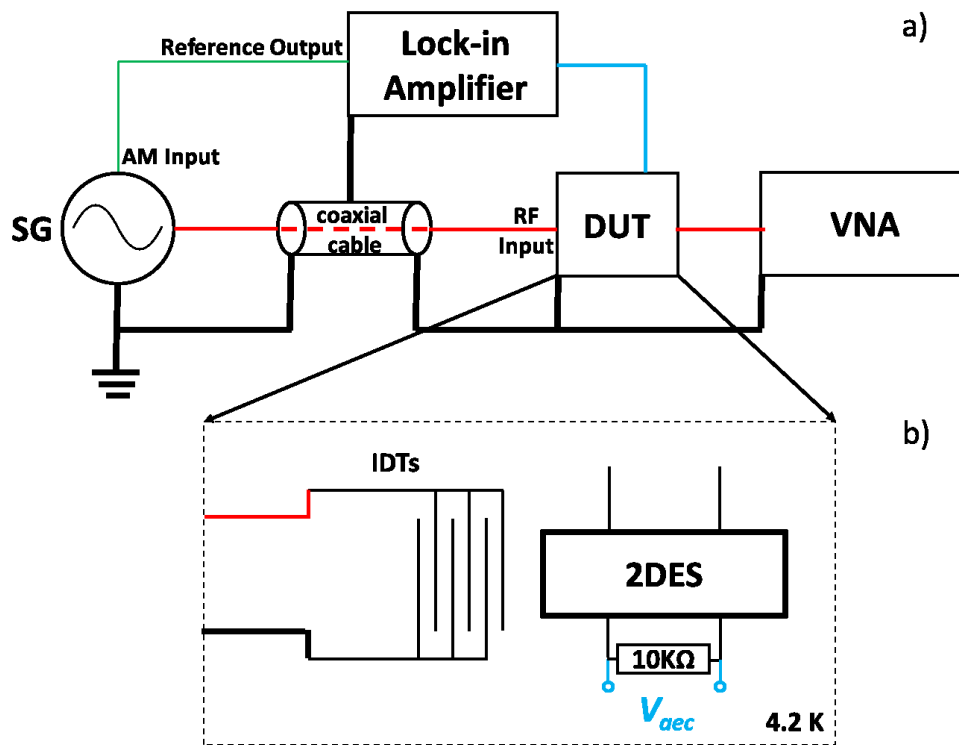


Figure 5.3.1 a) Sketch of amplitude modulation (AM) for SAWs measurements, b) Measurements connection for the device under test (DUT) shown in a). 2DES: Two-Dimensional Electron Systems, AM: Amplitude Modulation, DUT: Device under Test, IDTs: Interdigitated Transducers, V_{aec} : voltage induced by the acoustoelectric current. RF: Radiofrequency Signal; SG: Signal Generator; VNA: Vector Network Analyzer.

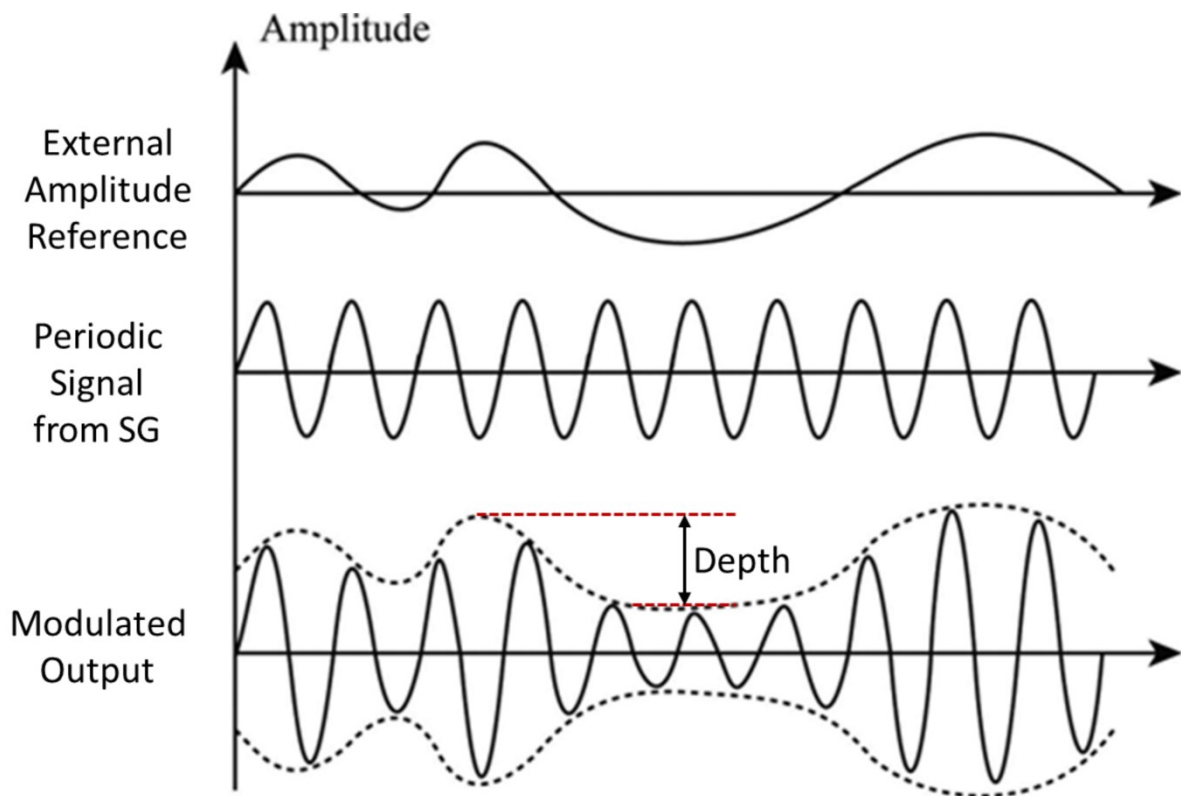


Figure 5.3.2 Principle of amplitude modulation [WIKI.AM]. Here, the modulation depth is between 90% and 100%.

SAWs generate an acoustic current passing through the etched Hall bar, which can be measured by connecting a resistor between two longitudinal contacts on the same side of the Hall bar as shown in figure 5.3.1 b). The resistor closes an electrical circuit for the electrons that are dragged along by the surface acoustic waves. The acoustic current can be deduced by measuring the voltage drop across the resistor. Two additional methods to measure the acoustic current will be discussed when introducing the acoustoelectric transport in graphene in Section 5.6.

The resonance frequency of the IDTs is determined by sweeping the frequency as shown in figure 5.3.3 for various powers between -18 dBm to +2 dBm. A strong maximum of the acoustic current appears around 700 MHz. This resonant frequency is scrutinized by repeatedly sweeping with higher resolution several times as shown in the inset.

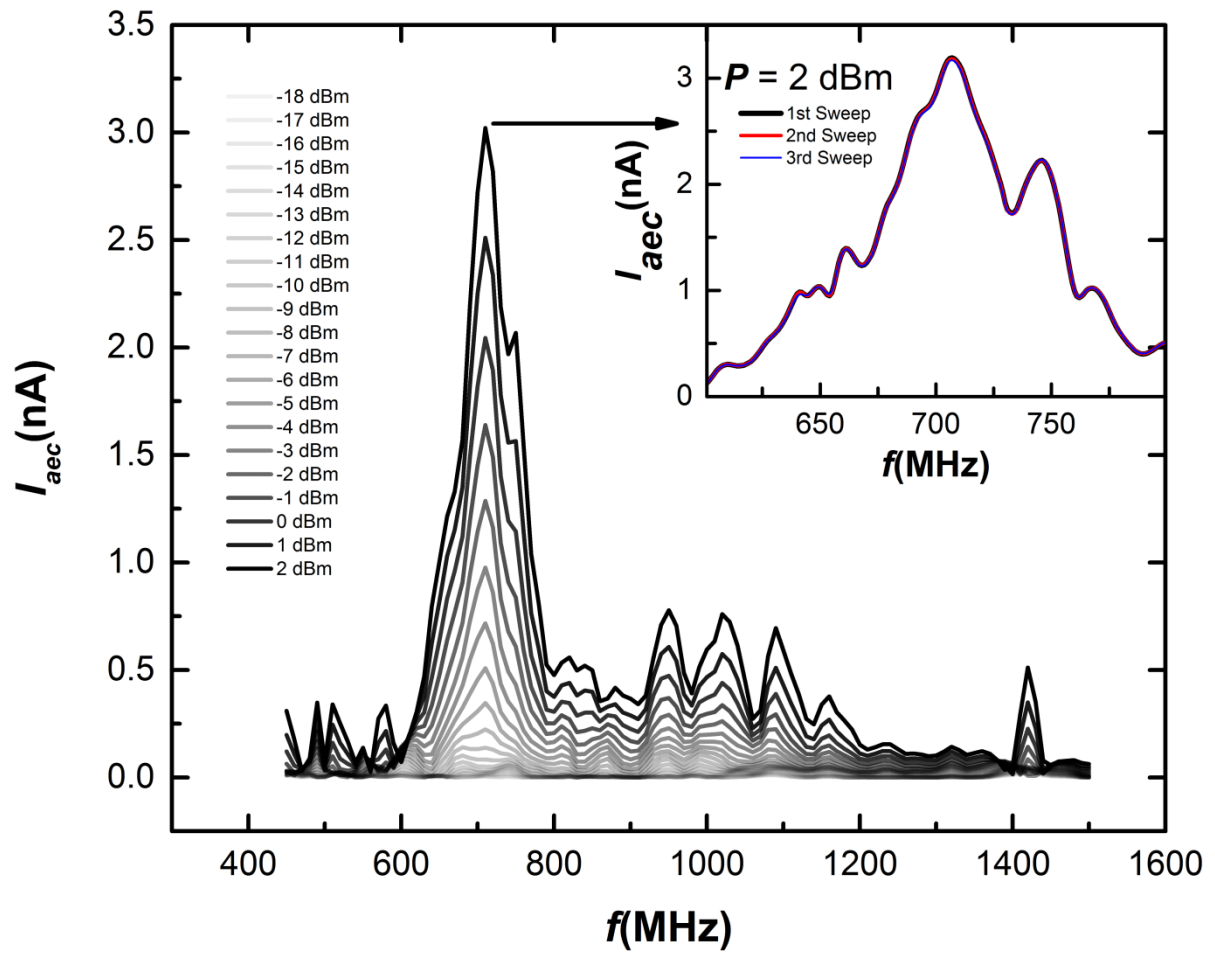


Figure 5.3.3 Power dependence of the acoustic current for different frequencies. The inset shows a finer frequency step size in the range between 600 MHz and 800 MHz with 2 dBm. The resonance is fully reproducible for repeated sweeps.

5.4 Characterization of Graphene on a GaAs Substrate

When graphene is transferred to a piezoelectric substrate, surface acoustic waves excited in the substrate can be used to drive transport in the graphene on top. After a transfer process of CVD monolayer Graphene onto a GaAs substrate as described in Refs. [T.LYO2017T, J.SIC2015], Raman spectroscopy is used to verify that we are still having monolayer graphene. Raman spectra are measured with a Reinshaw inVia microscope that operates at 532 nm.

Figure 5.4.1 a) shows Raman measurements by Timothy Lyon on CVD monolayer graphene transferred to a SiO₂ substrate [T.LYON2017]. For comparison, figure 5.4.1 b) shows Raman spectra of our sample with Graphene on top of GaAs. The height of the G-peak is approximately one third of 2D-peak, indicating that the transferred graphene has monolayer character. Since the visibility of graphene on GaAs is very low [K.PET2011], no optical image is shown.

In order to minimize defects and to remove surface doping such as water, the sample is baked prior to the cool down as discussed in Chapter 3. Because IDTs are used to induce surface acoustic waves and drive an acoustic current through the graphene layer, no Ohmic contacts (i.e., source and drain) are located in propagation path of SAWs. A constant current for regular magnetotransport has to be applied between the side contacts as shown in the inset of figure 5.4.2. The longitudinal voltage and Hall voltage are measured on the other four contacts. At 4.2 Kelvin, typical resistances of the Ohmic contacts to the graphene layer are of the order of (20 – 25) k Ω . From the slope of the Hall resistance between -2 and 2 T, we can deduce a carrier density of $n = 9.1 \times 10^{11} \text{cm}^{-2}$, and the corresponding mobility of $\mu = 4.16 \times 10^2 \text{cm}^2 \text{V}^{-1} \text{s}^{-1}$. Since the 500 μm thick GaAs substrate is undoped, it is not possible to access the charge neutrality point of the graphene layer by applying a voltage to the inside of the chip carrier since this would require hundreds of volts.

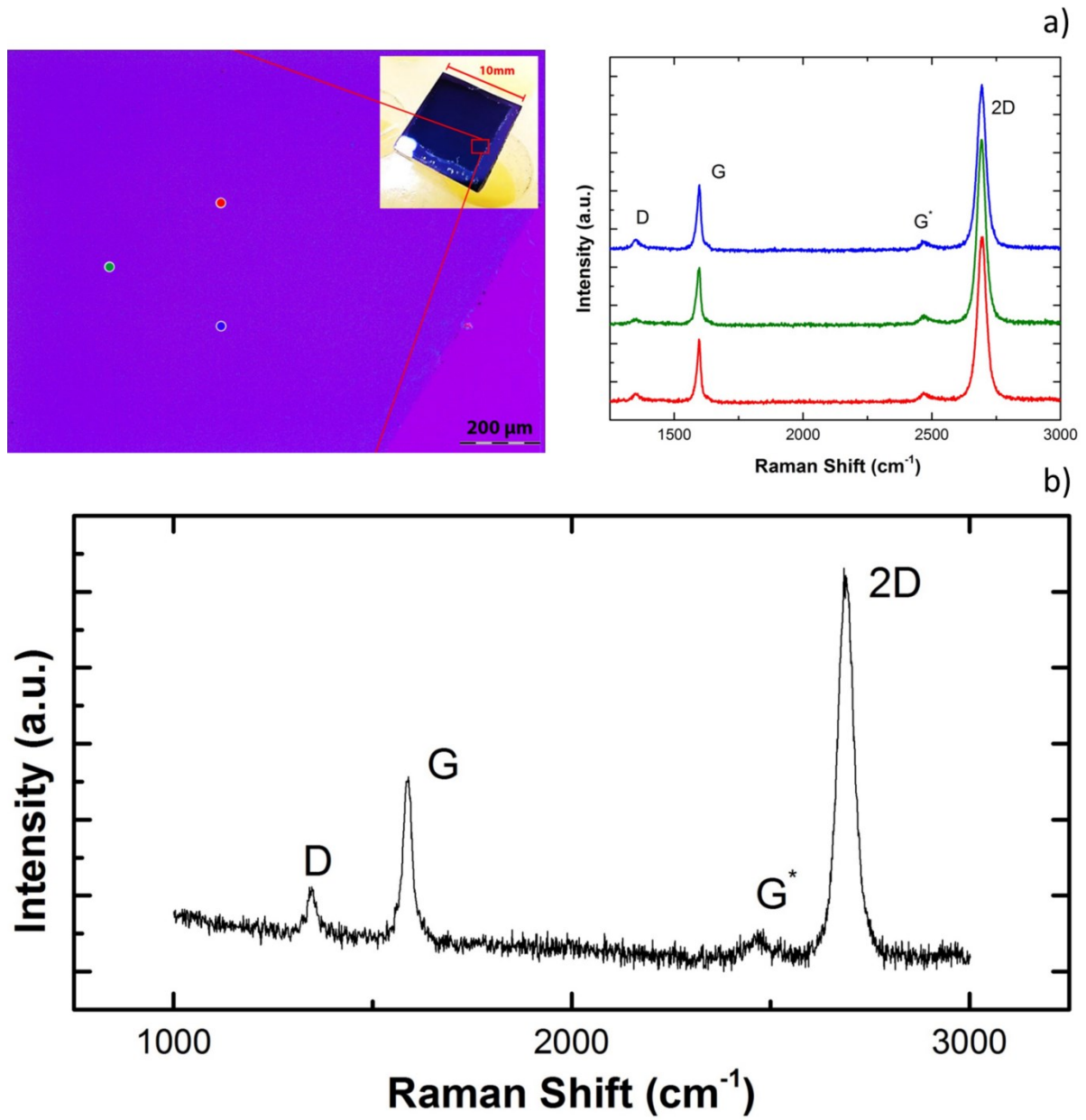


Figure 5.4.1 a) Left: optical microscope image of a transferred monolayer graphene on SiO_2 , Right: Raman spectra measured at the three colored points in the left image [T.LYON2017], b) Raman spectra of a transferred monolayer graphene on GaAs. The ratio between G and 2D peaks verifies the monolayer character of this sample.

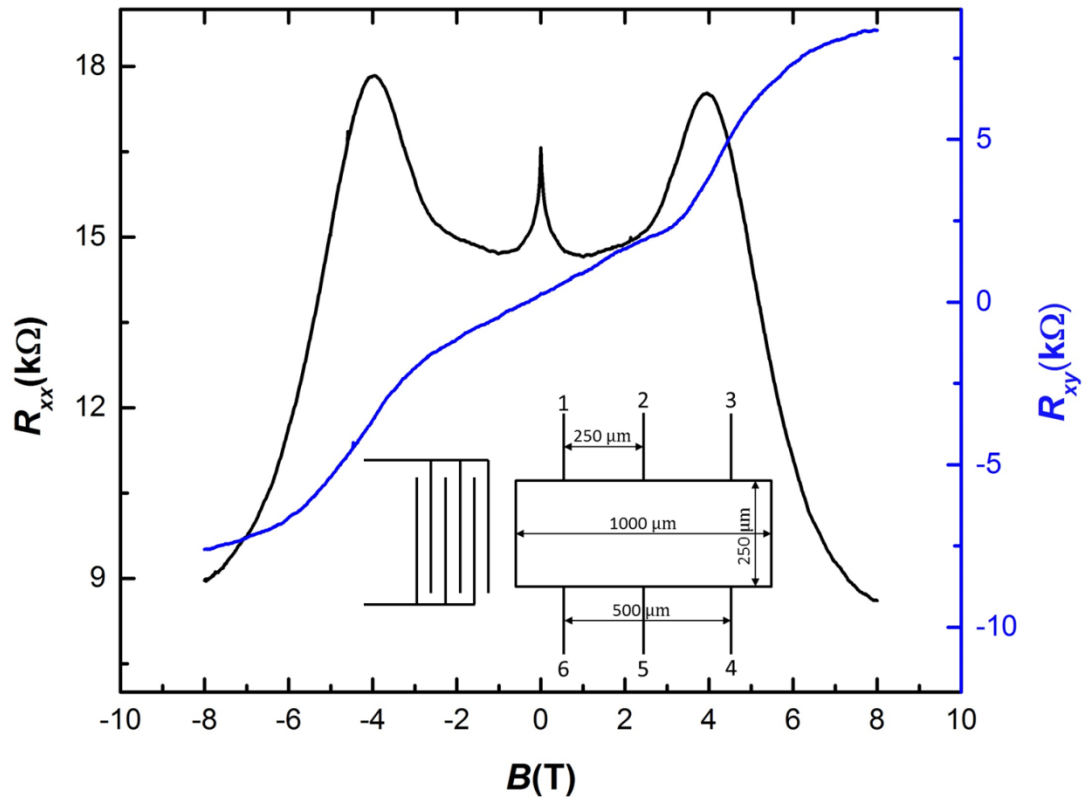


Figure 5.4.2 Regular magnetotransport of monolayer graphene on a GaAs substrate using a constant current between contacts 1 (source) and 3 (drain/ground). The longitudinal voltage is measured between contacts 4 and 6 and the Hall voltage between contacts 2 and 5. A weak localization peak is seen around 0 T and the onset of Landau quantization beyond 8 T. The measurements are performed at 4.2 K. The inset shows the geometry of the measured graphene sample.

5.5 Electron Spin Resonance in Monolayer Graphene

From systematical resistively detected ESR measurements on monolayer graphene, Timothy Lyon and Jonas Sichau extracted the intrinsic g -factor of graphene. Figure 5.5.1 shows the corresponding data, with the yellow dashed line being a guide to the eye for the measured electron Zeeman splitting, which has a slope of 1.95 ± 0.02 [J.SIC2018].

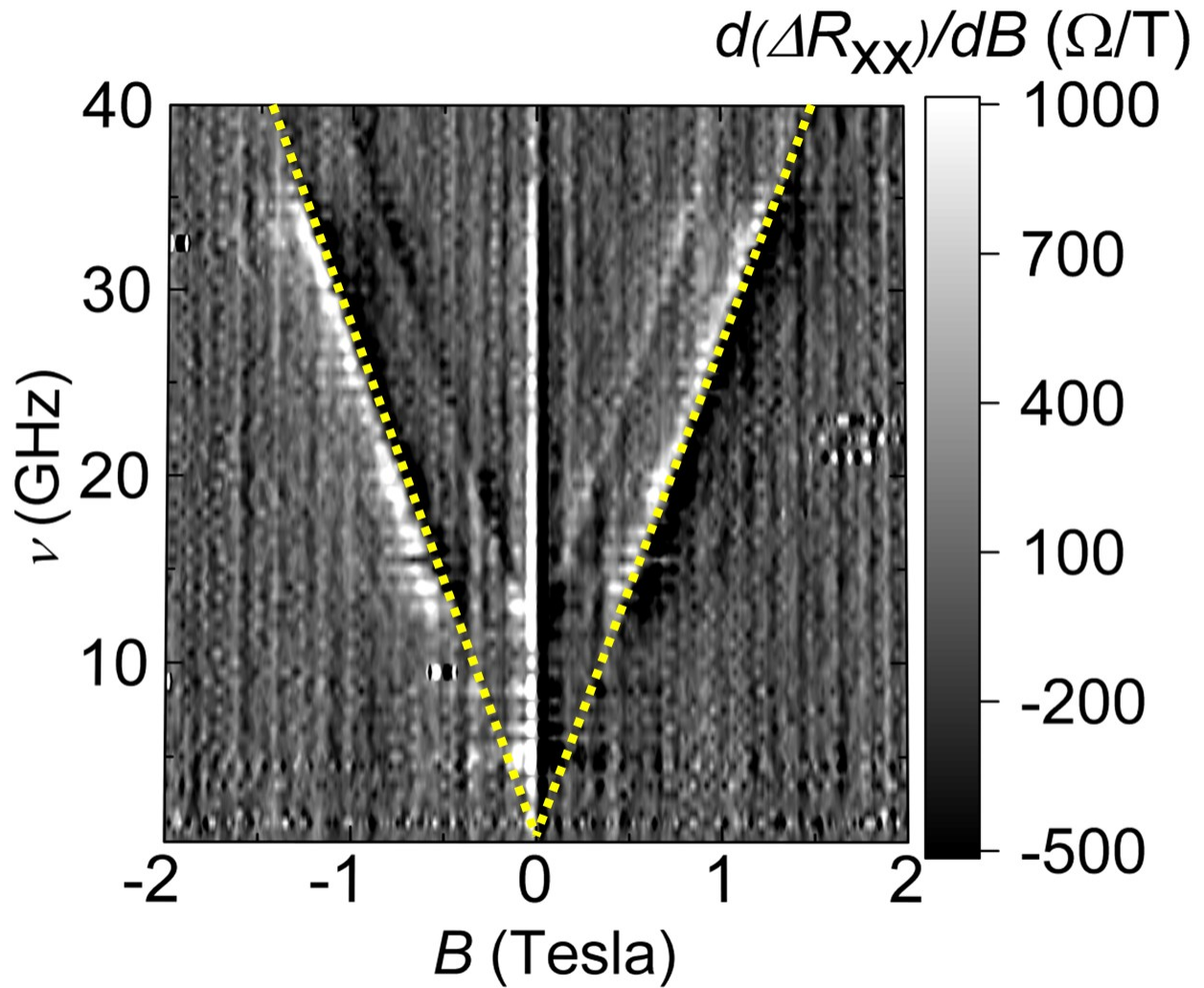


Figure 5.5.1 Derivative of ΔR_{xx} , i.e., the frequency induced change of the longitudinal resistance measured at 4.2 K. The yellow dashed line emphasizes the Zeeman splitting according to Equation 5.5.1. Data from [J.SIC2018].

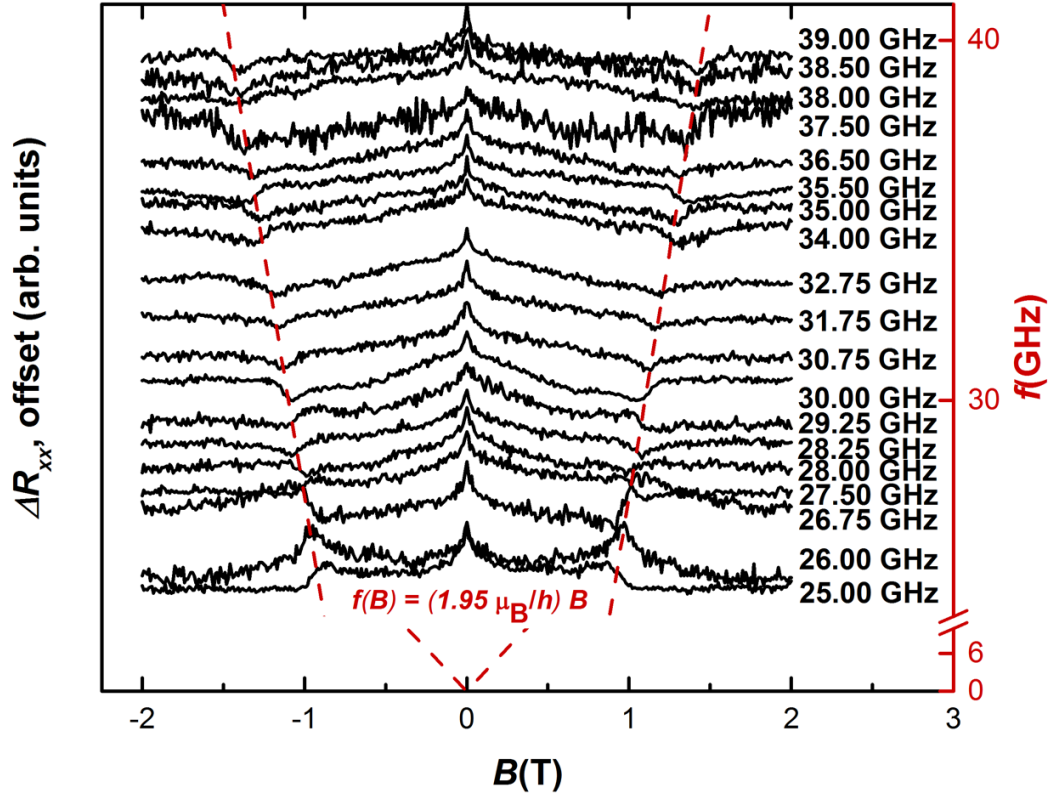


Figure 5.5.2 Normalized ΔR_{xx} for graphene on a GaAs substrate. The resonance positions are shifted according to the frequencies. The dashed red line is plotted according Equation 5.1.1 assuming a g -factor of 1.95.

With the g -factor of 1.95, it is possible to calibrate the ESR measurements of graphene on GaAs by calculating the required resonant frequency as a function of magnetic field

$$f = \frac{g\mu_B B}{h} = 27.3(\text{GHz} \cdot \text{T}^{-1}) \times B \quad 5.5.1$$

Equation 5.5.1 very well describes the electron spin resonances observed in my monolayer graphene on a GaAs substrate as shown in figure 5.5.2. The red dashed line is a guide to the eye calculated with a g -factor of 1.95.

It should be noted that in contrast to the measurements performed by Jonas Sichau, the derivative of the magnetoresistivity (obtained by subtracting the dark resistivity from the resistivity under microwave irradiation) shows both peaks and minima. Two representative examples are shown in figure 5.5.3. Currently, the physical mechanism behind this phenomenon is not understood.

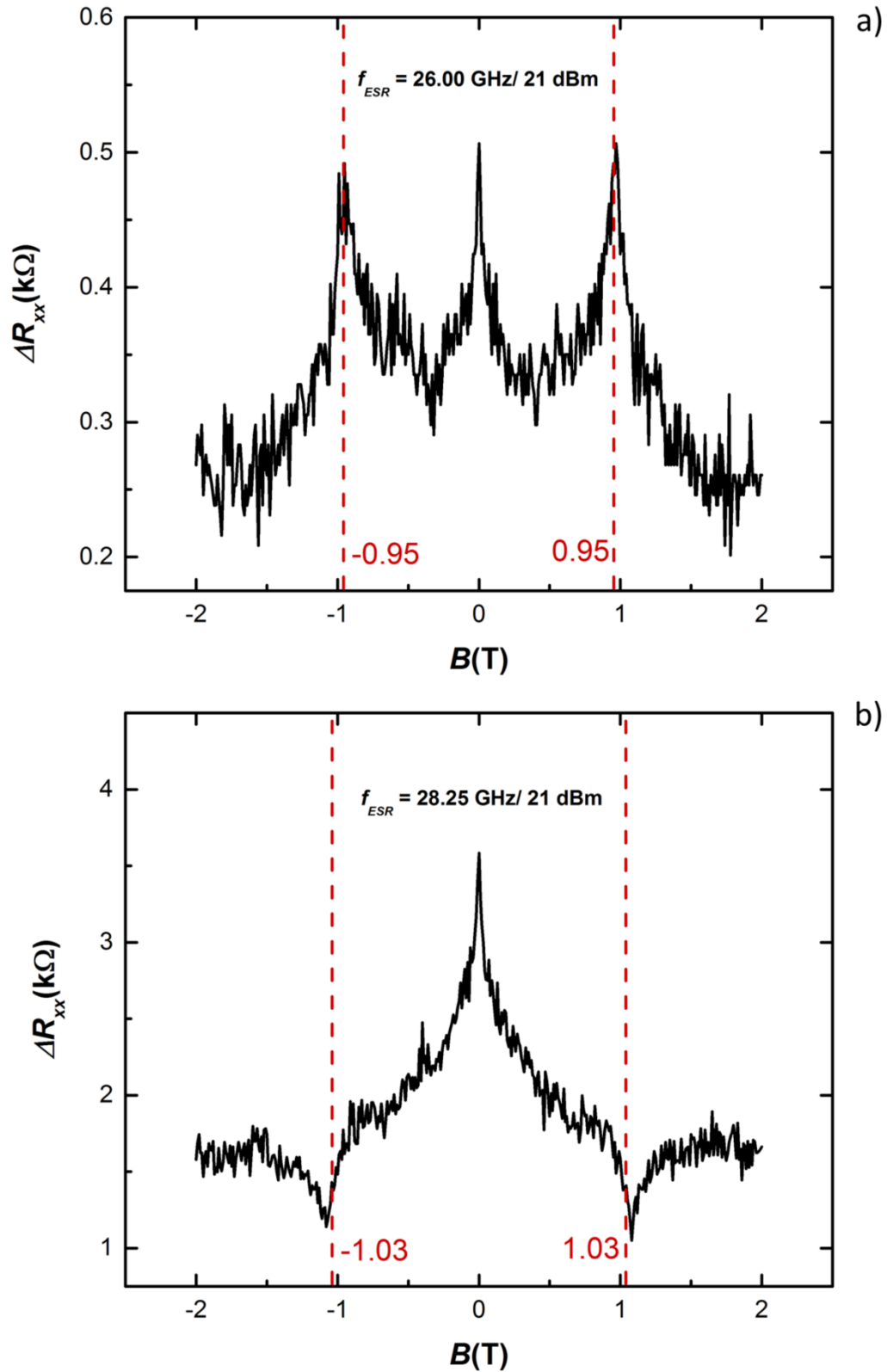


Figure 5.5.3 The difference between dark longitudinal resistivity and the resistivity under microwave irradiation for a) 26 GHz and b) 28.25 GHz vs. magnetic field. Electron spin resonances emerge as an increase or a decrease in resistance. The dashed red plot is resonant position calculated with a g -factor of 1.95.

5.6 Surface Acoustic Wave Interaction with Graphene

The previous section has shown standard magnetotransport and ESR measurements on monolayer graphene that is resting on an insulating GaAs substrate. For these measurements, a constant low frequency ac current was passed through the sample. In the following section, I will show how surface acoustic waves generated by IDTs on the GaAs substrate can trigger an acoustoelectric current that substitutes the regular ac current used in the previous experiments. By studying the frequency and power dependence of the IDTs, its transmission and resonance frequency can be determined as well as the power required to drag along (acoustoelectric) electrons in the graphene sheet. Finally, resistively detected electron spin resonance using magnetotransport based on an acoustoelectric current is studied. We are the first to implement and report SAW-induced currents in graphene for ESR measurements using an electrical detection method.

Transmission of Interdigitated Transducers

The transmission of IDTs is determined by measuring the S_{22} parameter, i.e., the reflection coefficient at the output port of a Network Analyzer. Here, I used an Agilent 8357A PNA series Network Analyzer as shown in figure 5.6.1. The Network Analyzer sweeps the radio frequency while simultaneously detecting the reflection. The IDT's resonance is the frequency with the lowest reflection S_{22} , or maximal absorption, respectively. In the present sample, the resonance is found at 570 MHz.

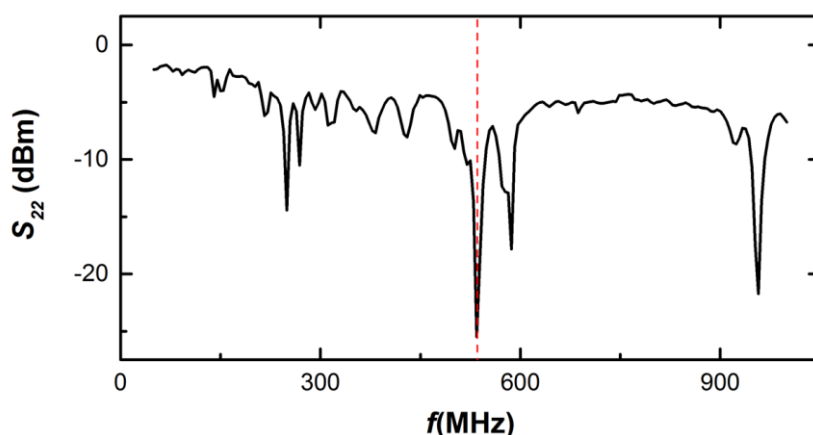


Figure 5.6.1 IDT reflection coefficient S_{22} measured at the output port of a Network Analyzer. The main resonance is seen at 570 MHz.

Acoustoelectric Current Detection

Figure 5.6.2 compares three methods for the measurement of the acoustoelectric current. Method a) is identical to the one previously shown in figure 5.3.1 b) which uses a known resistor to close the electrical circuit and to calculate the I_{aec} from the measured voltage drop. Methods b) and c) use a real physical mass (ground/drain) potential to close the electrical circuit. The drain contact should be located at the far end of the Hall bar, i.e., on the opposite side of the IDTs. The current is measured either directly with a current meter or indirectly from the voltage drop across a resistor. While all three methods give the same acoustoelectric current, using a physical ground potential is preferable.

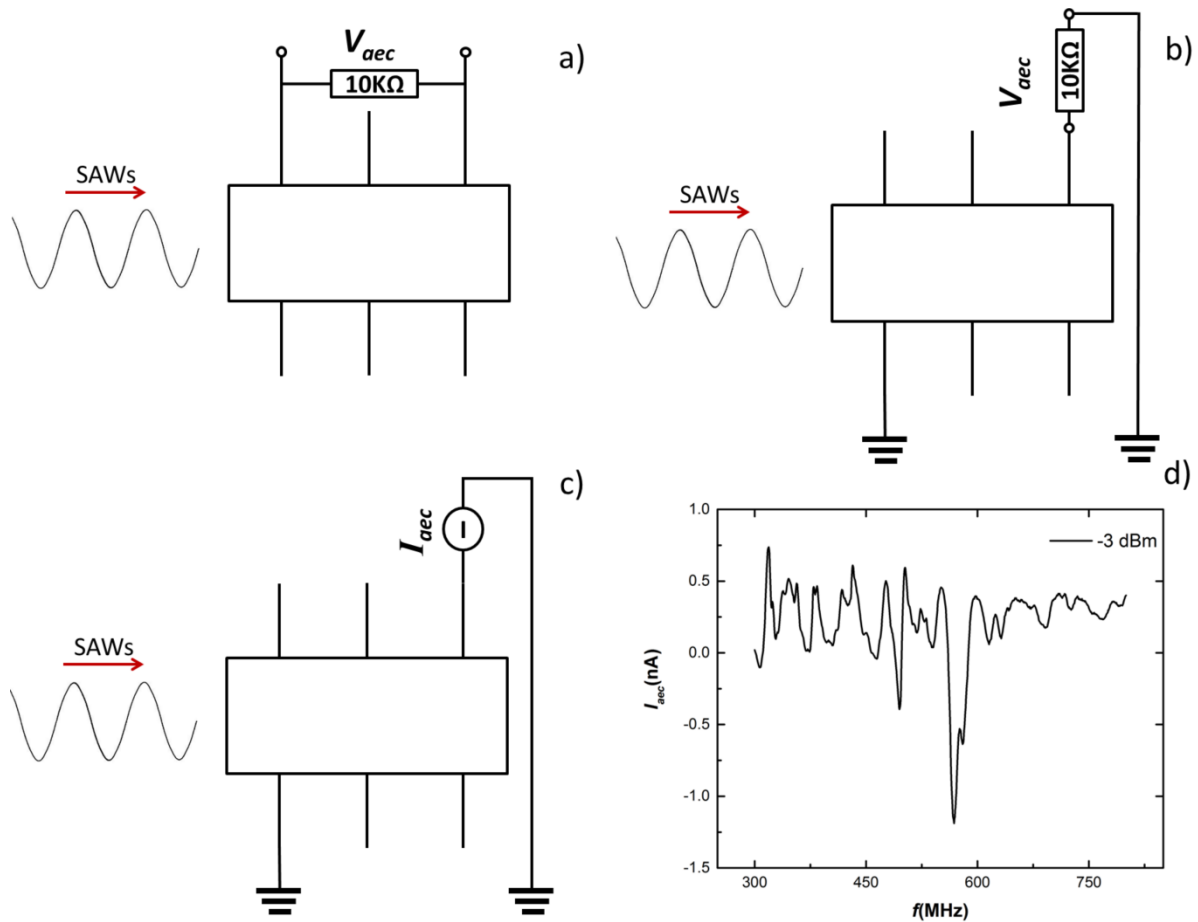


Figure 5.6.2 Three equivalent methods to detect acoustoelectric currents. a) Measurement of the voltage drop across a 10 KΩ resistor in parallel to the Hall bar that closes the electrical circuit, b) A 10 KΩ resistor *in series* to the Hall bar and connected to ground, c) A current meter (Lock-in Amplifier) connected *in series* to the Hall bar. For methods b) and c), the drain contact should be located on the opposite of the IDTs.

Acoustoelectric Current Studying

For all subsequent measurements of the acoustoelectric currents, method c) was used. The experimental setup is shown in figure 5.3.1 a) with the Lock-in Amplifier providing a reference for both modulation of signal generator and the input of Lock-in amplifier for acoustoelectric current measurement. Since the acoustoelectric current is directly measured with the “current input” of the Lock-in Amplifier, the lockin’s phase sensitive detection allows for a study of the electron flow direction.

To determine the resonance frequency of the IDTs, first a coarse frequency sweep (10 MHz steps) is performed to find the resonance, followed by a fine sweep (2.5 KHz steps) for the exact resonance condition. the resonance frequency of our IDTs in graphene is 571.5 MHz as shown in figure 5.6.3.

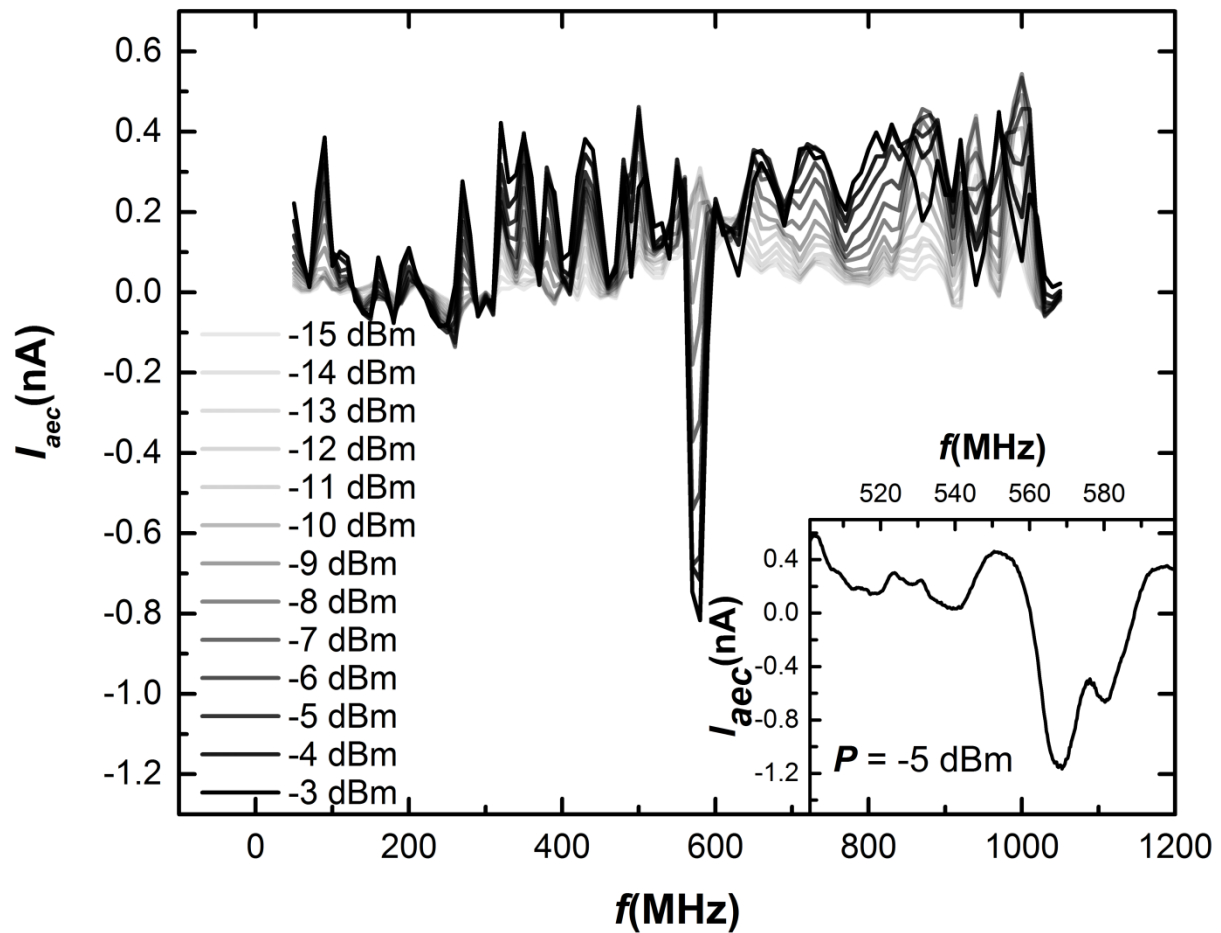
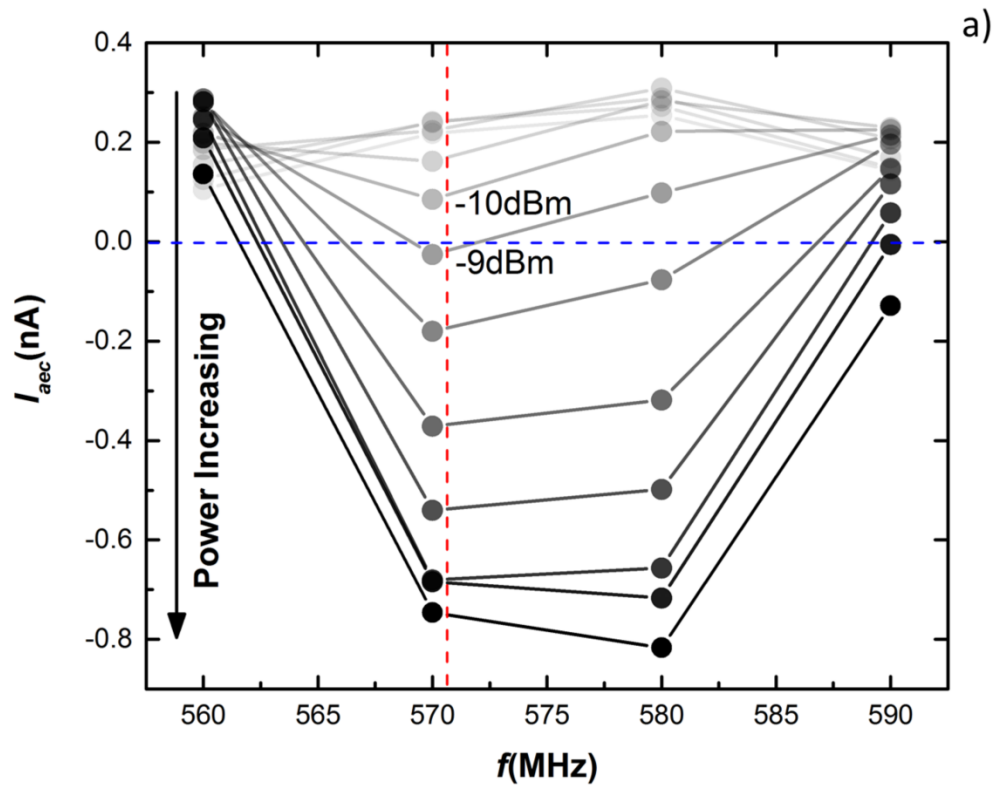


Figure 5.6.3 Resonance frequency measurement. Inset: fine step sweeping to locate the accurate resonance.



Power: $\sim > \sim > \sim$

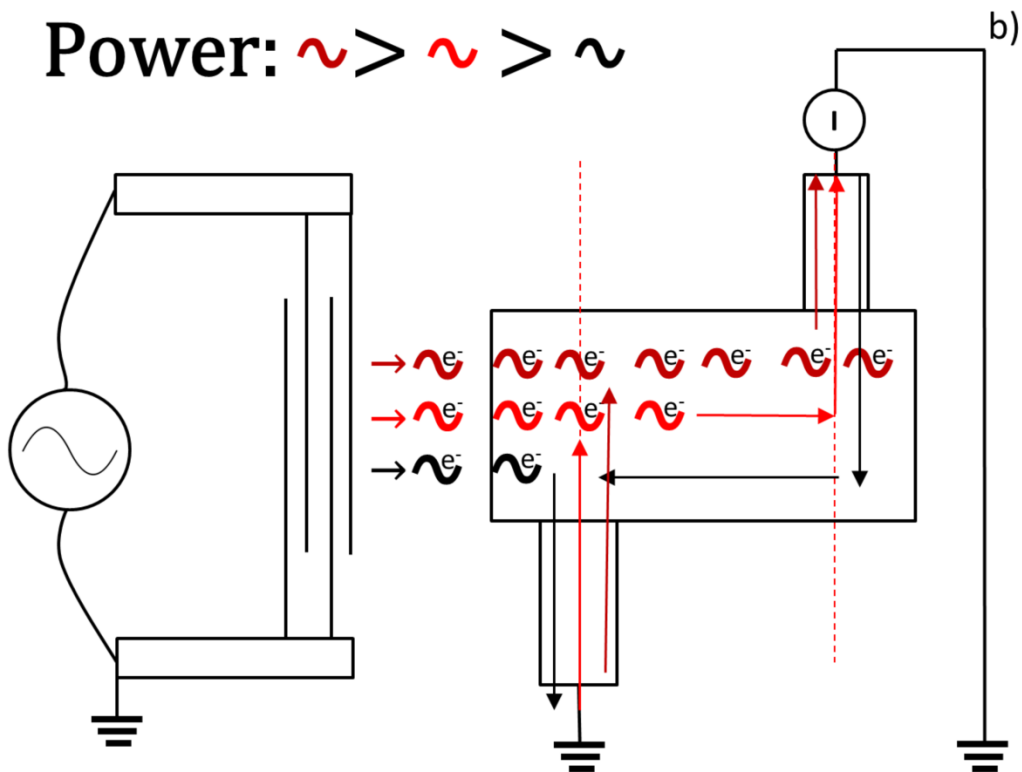


Figure 5.6.4 a) Dependence of the acoustoelectric current on the power applied to the IDTs. The acoustoelectric current changes sign from positive to negative between -10 dBm and -9 dBm, b) Sketch explaining the change in sign. For small powers, electrons flow predominantly towards the lower left terminal while for large powers the SAW is strong enough to drag electrons to the upper right terminal.

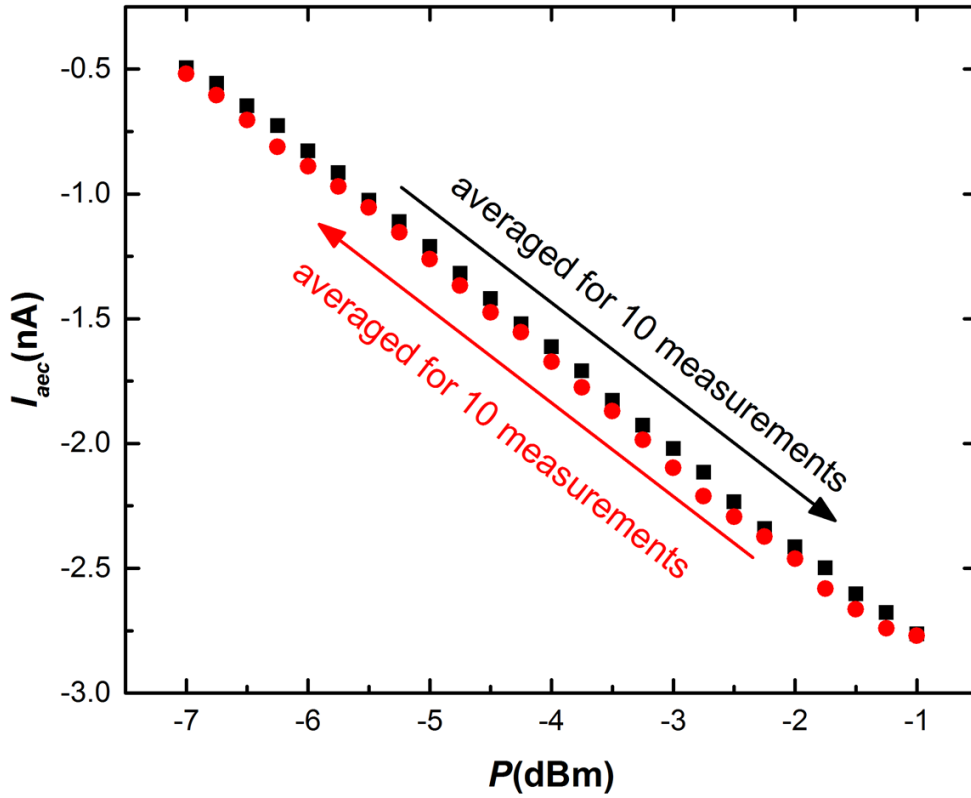


Figure 5.6.5 Acoustoelectric current as a function of power (for power increase indicated by black dots and decrease indicated by red dots)

The acoustoelectric current exhibits a sign reversal for small powers [fig. 5.6.4 a)]. At powers below -9 dBm the current is positive, while it changes sign to negative for larger powers. The change in sign is probably related to the ability of the surface acoustic waves to drag along electrons. Low powers will only generate weak propagating waves. The grounded contact closest to the IDT will act as a drain that accepts the majority of electrons. In this case, the electrical circuitry will supply electrons originating from the terminal contact at the other end, which also measures the current. Electrons will thus enter the graphene Hall bar indicated by the black solid line shown in figure 5.6.4 b), resulting in a positive current. With increasing power, the generated SAWs have the ability to drag the majority of electrons to the distant terminal contact, resulting in a negative current. Figure 5.6.5 shows the power dependence of the acoustoelectric current, which increases proportionally with applied power.

Electric Current Transport induced by SAWs in Graphene Measured in Strong Magnetic Field

The following section will present magnetotransport experiments, which are driven by acoustoelectric currents instead of conventional low frequency ac currents. The surface acoustic wave induced current is measured at “Contact 3” (most distant to the IDT) and “Contact 1” (closest to the IDT) is grounded (contact numbers are shown in figure 5.4.2). The longitudinal voltage is measured between “Contact 4 and 6”, and the Hall voltage between “Contact 2 and 5”.

The measured longitudinal and Hall voltages are purely resulting from an acoustoelectric current, no (additional) AC or DC bias current was applied. The acoustoelectric current is induced by exciting the interdigitated transducers at their resonant frequency of 571.5 MHz, with an output power of -2 dBm. The generated acoustoelectric current is approximately 2 nA at 0 Tesla.

The (acoustoelectric) longitudinal voltage as well as the measured acoustoelectric current is shown in figure 5.6.6, which compares them to conventional transport measured with a conventional constant ac current. The acoustoelectric data reproduce the general trend of the conventional transport. Differences/shifts could be related to the velocity shift of the surface acoustic waves, which are very sensitive to the conductivity of graphene.

The transport data based on an acoustoelectric current exhibit additional oscillating features, which are not observed in conventional transport measurements. The origin of these oscillations has yet to be understood, however, they might be related to strain-induced lateral potential wells generated by the SAW, which match the electron cyclotron orbits. Surface acoustic waves that drags electrons with speed of approximately 10^3 ms^{-1} will modify the conductivity of the Graphene sample in contrast to conventional currents, with electrons travelling with the Fermi velocity and without strain. However, more experimental and theoretical work is needed to understand these features.

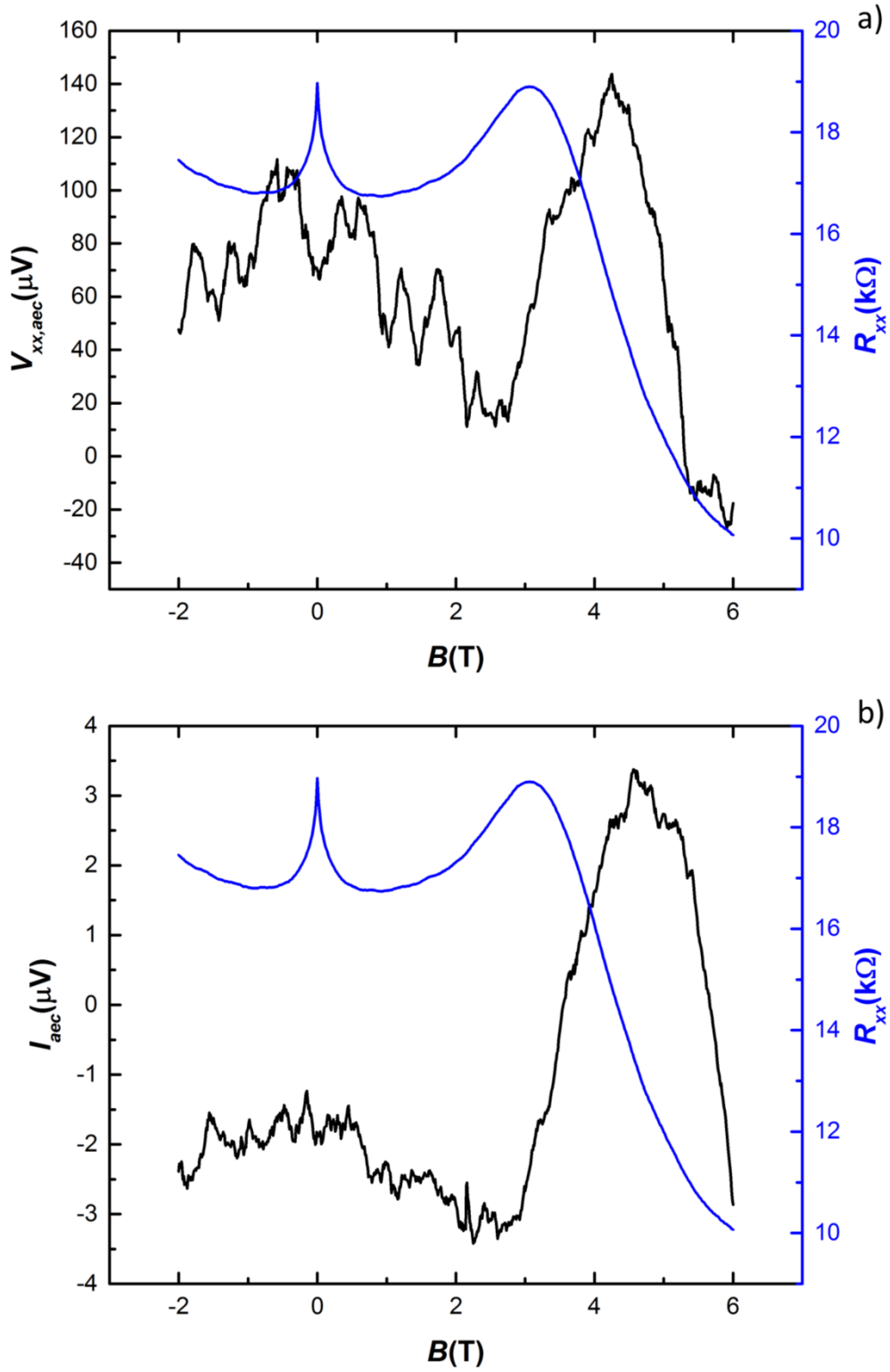


Figure 5.6.6 Magnetotransport measured with an acoustoelectric current (solid black lines, left axis) compared to conventional magnetotransport with a low frequency ac current (solid blue lines, right axis). a) Longitudinal voltage and b) acoustoelectric current as a function of magnetic field.

Electron Spin Resonance Measurements with Acoustoelectric Currents in Graphene

Acoustoelectric currents have been implemented in resistively detected electron spin resonance experiments. Since surface acoustic waves generate dynamic strain that breaks the crystal symmetry, resulting changes in the g -factor might appear as frequency shifts in the ESR signal. ESR measurements based on acoustoelectric currents are performed as follows: To improve the signal-to-noise ratio, an average of three measurements with the same (ESR) frequency is calculated. Like in conventional ESR, the resonance is only seen when the voltage difference between the dark condition and the irradiated condition is plotted. Figure 5.6.7 shows an example for an ESR frequency of 28 GHz. The figure demonstrates the reproducibility of the measurements.

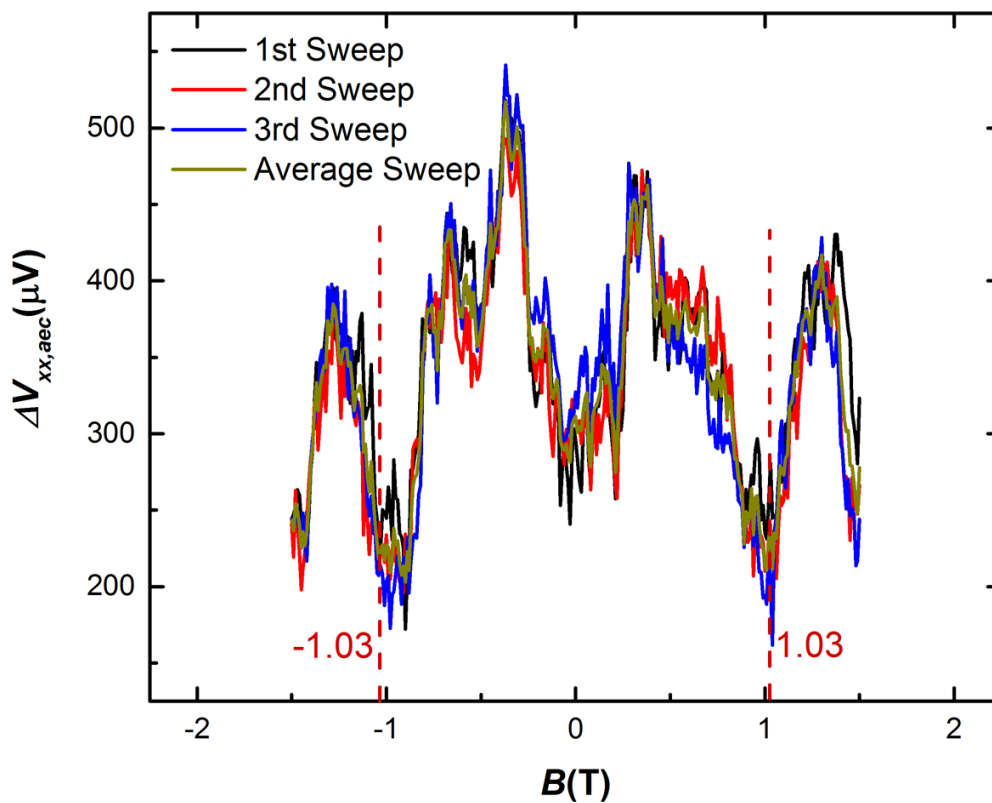


Figure 5.6.7 Difference of a longitudinal voltage before and after microwave radiation with 28 GHz at 20.5 dBm. The voltage is the result of an acoustoelectric current that was generated by SAWs (571.5 MHz and -2 dBm).

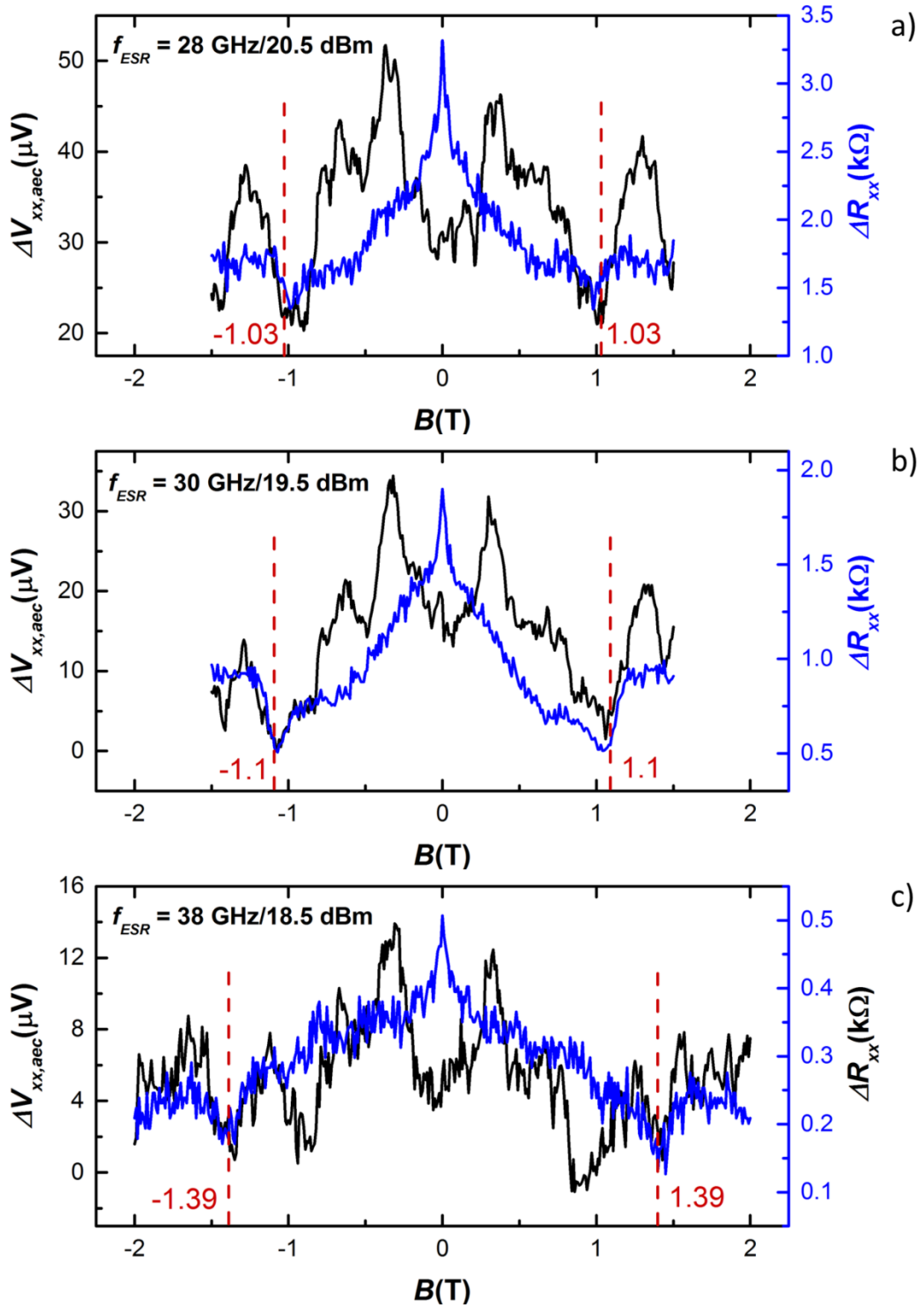


Figure 5.6.8 Comparison of electron spin resonance using acoustoelectric currents (black, left axis) and conventional currents (blue, right axis) at a) 28 GHz, b) 30 GHz and c) 38 GHz. The dashed red line is a guide to the eye indicating the expected ESR resonance for a g -factor of 1.95. A pronounced minima, shifting with frequency, appear in both the black and the blue plots, following the position of dashed red line.

For certain frequencies, I am able to identify electron spin resonances (measured with acoustoelectric currents) which are also detectable with conventional ac currents, as shown in figure 5.6.8. At the expected (ESR) resonance position for a g-factor of 1.95, I am able to observe minima in both the conventional current plot (red) and the acoustoelectric current plot (black). Figure 5.6.9 shows a waterfall plot combining multiple acoustoelectric ESR measurements. The measured data were normalized and shifted to allow comparison. The dashed red line is a guide to the eye for the expected resonance using the experimentally determined g-factor of 1.95 by Timothy Lyon [T.LYO2017T]. With increasing ESR frequency, some valleys shift towards higher magnetic fields while other peaks or valleys are pinned. Those valleys that shift follow roughly the dashed red line, implying that these are indeed electron spin resonances which have been measured by an acoustoelectric current.

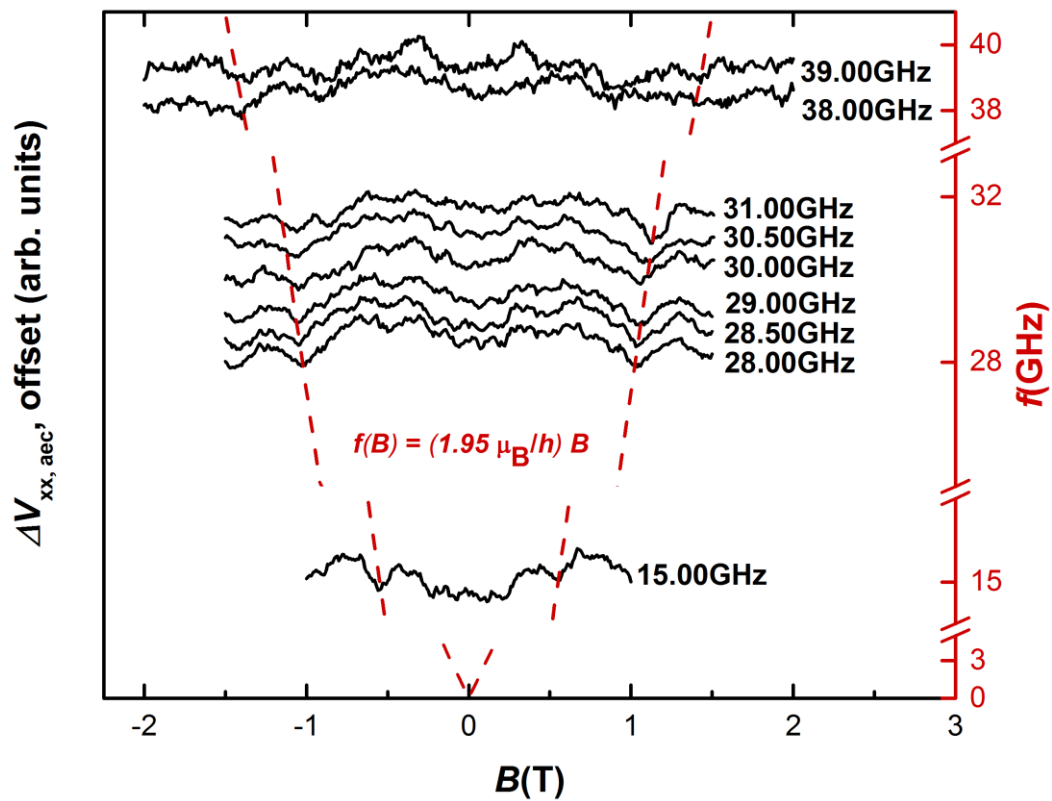


Figure 5.6.9 Normalized and shifted plots of the changes of the longitudinal voltage measured with acoustoelectric currents.

A persisting problem for these measurements, however, is the stability of the acoustoelectric current over long time scales. During slow sweeps of the magnetic field, the acoustoelectric current might vary by 20%, resulting in measurement artifacts. The problem might be related to: a) The fabrication of the IDTs, which will impact on the generated surface acoustic waves in terms of collimating of wave path and stability of wavelength and amplitude, b) The attenuation of the coaxial lines that are used as wave guides for the radiofrequency signal. It is an ongoing effort to improve the measurement setup.

Chapter 6

Conclusion and Outlook

6.1 Summary

The scope of this thesis was the study of two-dimensional systems in conventional III-V semiconductor heterostructures and monolayer graphene using high frequency excitations methods.

Standard GaAs quantum well Hall bar structures, GaAs quantum well Hall bars with interdigitated transducers as well as graphene Hall bar structures on insulating GaAs substrates were designed and fabricated. The structures were defined by multiple photolithography and electron beam lithography steps, wet chemically etched and metallized by physical vapor deposition for Ohmic contacts or gating/IDTs. Lift-off after metallization was a crucial step, requiring bilayer photoresist.

I used conventional magnetotransport measurements with low frequency ac currents to characterize the GaAs quantum Well systems and monolayer graphene samples. The carrier densities and mobilities were determined to obtain the magnetic field positions of odd filling factors where electron spin resonance in GaAs was studied. ESR measurements on a standard GaAs quantum well Hall bar sample exhibited large shifts of the electron spin resonance owing to Overhauser fields that were created by dynamically polarized nuclear spins. To manipulate and control the electron spin resonance, two methods were scrutinized: i) a second coil, radiating electromagnetic waves in the frequency range of the nuclei, was implemented, ii) [assuming sufficiently long nuclear spin diffusion times] a controlled rapid change between the two frequency ranges (NMR and ESR). However, both methods did not yield satisfying results since the available sample did not show a reproducible behavior between different cool downs. New samples are currently in preparation for complementary measurements. Tests to release freestanding GaAs membranes were made to lay the groundwork for the combination of surface acoustic wave and electron spin resonance detection schemes.

Acoustoelectric currents, generated by surface acoustic waves on piezoelectric materials, were used as an alternative to conventional constant ac currents. The magnetotransport of monolayer graphene excited by surface acoustic waves was extensively studied. It could be shown that the longitudinal voltage measured with conventional currents and acoustoelectric currents follows the same general trends. However, additional features were observed in the acoustoelectric current measurements. I was able to demonstrate for the first time that it is possible to measure resistively detected electron spin resonance

purely based on an acoustoelectric current, which opens up the venue for new high frequency detection schemes.

6.2 Outlook

This thesis scrutinized various resonance methods to understand the interaction between low dimensional electron systems and acoustic-phonons and microwaves for the use in novel (mass) detection systems. While the results show a promising route for such detection schemes, more work is needed to better understand the underlying physics and to control and enhance the observed effects.

To enhance the effect of the surface acoustic waves in monolayer graphene, LiNbO_3 is a better substrate candidate due to its larger piezoelectric coefficient. I have triggered a collaboration with the THU/Beijing and suitable LiNbO_3 samples have already been prepared which I intend to study.

Mass sensing methods are based on changes of the oscillation (frequency) of membranes. A promising approach is the combination of SAWs and a released membrane of 200 nm to 300 nm thickness with an embedded 2DES as a resonator (as shown in Chapter 3). The membrane should be excited by surface acoustic waves, generated with interdigitated transducers on one side of the membrane. Different principles of detection are shown in figure 6.2.1 below:

- i. An input IDT will pass a surface acoustic wave across a membrane, which is then picked up by a second interdigitated transducer (i.e., the output IDT). The phase change of the waves passing the membrane will be a function of mass attached on the membrane.
- ii. Alternatively, instead of measuring the phase change at the output IDT, an acoustoelectric current can be used. The frequency shift due to mass can be detected by measuring the acoustoelectric current amplitude.
- iii. A simple transport measurement can also be used. The strain of the membrane changes with the mass attachment. In our group, the strain effect on Graphene has already been demonstrated.

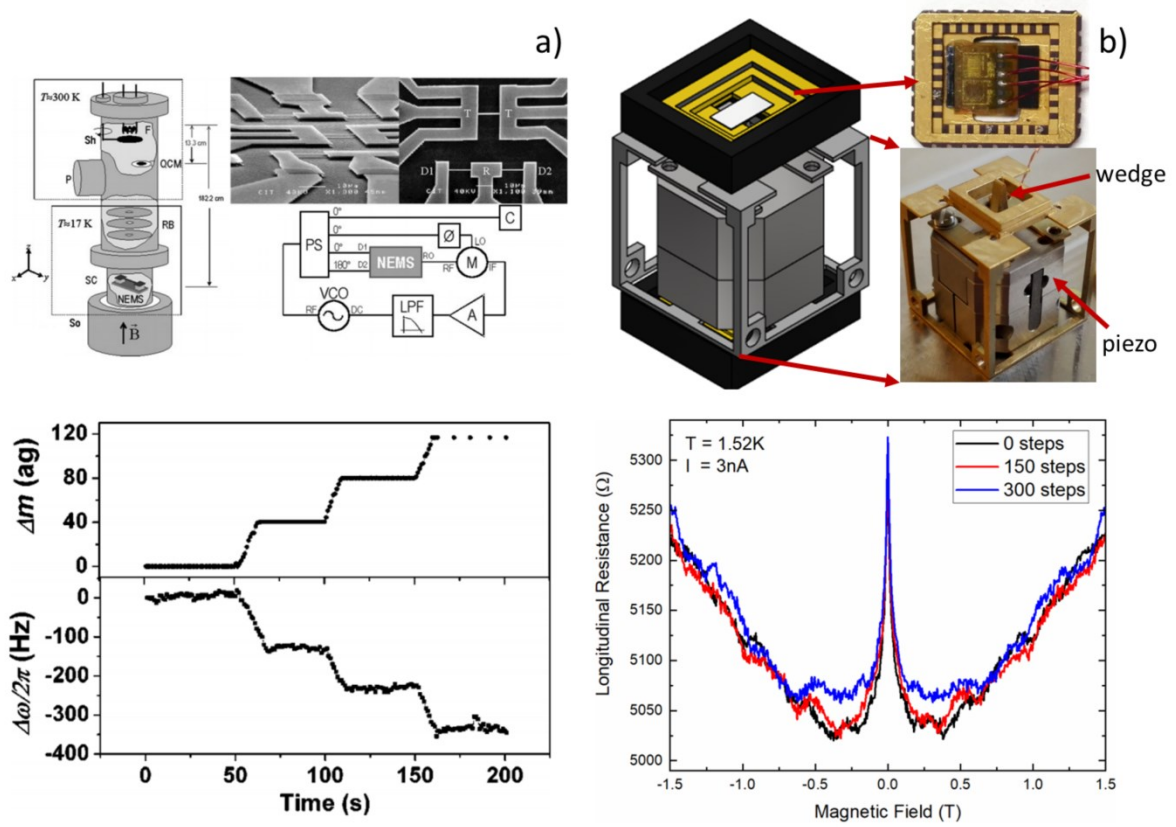


Figure 6.2.1 a) NEMS resonator detecting the mass of 40 ag ($1 \text{ ag} = 10^{-18} \text{ g}$), upper panel: measurement setup and sample configuration. The sample chamber is submerged in a liquid helium bath, inside a 6 Tesla superconducting solenoid. The resonator is shown in "D1-R-D2"; lower panel: frequency shifts of the resonator, induced by sequential 40 ag [K.EK12004], b) Transport measurements on Graphene affected by strain. Upper panel: A nanopositioner pushes a wedge into the sample to induce strain. Lower panel: the strain (shown as steps of the positioner) affects the transport properties [J.RIE2019].

Appendix A

Sample Information

A.1 Growth parameters

A.1.1 Growth parameters sample A

Material	Thickness (nm)
GaAs	5
AlGaAs	10
AlGaAs:Si	δ doping
AlGaAs	125
AlGaAs:Si	δ doping
AlGaAs	20
GaAs	25
AlGaAs	40
AlGaAs	10
AlGaAs:Si	δ doping
AlGaAs	10
Sacrificial Layer	100

A.1.3 Growth parameters sample C

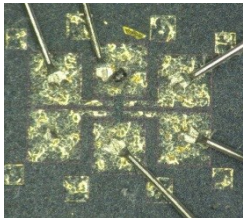
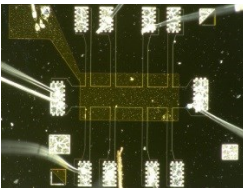
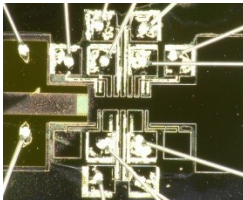
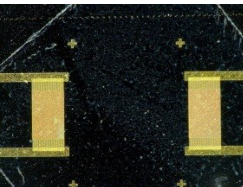
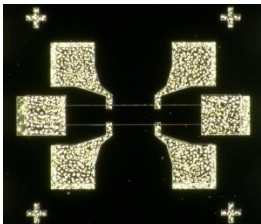
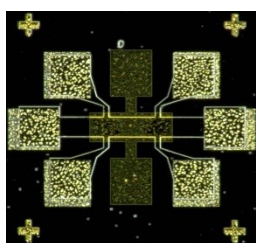
Materials	Thickness (nm)
GaAs	10
AlGaAs	51
AlGaAs:Si	δ doping
AlGaAs	71
GaAs	27
AlGaAs	5.2
GaAs/ AlGaAs Superlattice	60
AlGaAs	11
AlGaAs:Si	δ doping
AlGaAs	56
Sacrificial Layer	200

A.1.4 Growth parameters for unmeasured/uncharacterized samples

Material	Thickness (nm)
GaAs	5
$\text{Al}_{0.33}\text{Ga}_{0.67}\text{As:Si}$	57
$\text{Al}_{0.33}\text{Ga}_{0.67}\text{As}$	25
$\text{Al}_{0.33}\text{Ga}_{0.67}\text{As}$	5
GaAs	1000
GaAs/AlAs	250
Superlattice	

A.2 Sample List

Hall bar samples

Image	Structure and Comment
	<p>Sample A</p> <p>Hall bar $100\text{ }\mu\text{m} \times 50\text{ }\mu\text{m}$, contact distance $50\text{ }\mu\text{m}$ 2DES in GaAs/AlGaAs heterostructure, see Table A.1.1</p>
	<p>Sample B</p> <p>Hall bar $1000\text{ }\mu\text{m} \times 200\text{ }\mu\text{m}$, contact distance $250\text{ }\mu\text{m}$ 2DES in GaAs/AlGaAs heterostructure materials</p>
	<p>Sample C</p> <p>Hall bar $400\text{ }\mu\text{m} \times 100\text{ }\mu\text{m}$, contact distance $50\text{ }\mu\text{m}$, Pitch $8\text{ }\mu\text{m}$ 2DES in GaAs/AlGaAs heterostructure, see Table A.1.2</p>
	<p>Graphene on insulating GaAs substrate The Hall Bar will be processed in the middle of IDTs with size of $1000\text{ }\mu\text{m} \times 250\text{ }\mu\text{m}$. The IDTs are 1.8 mm in distance. Graphene/PMMA stack transferred on GaAs shown here, Hall bars to be made next.</p>
	<p>NOT measured yet, NO gate</p> <p>Hall bar $300\text{ }\mu\text{m} \times 100\text{ }\mu\text{m}$, contact distance $150\text{ }\mu\text{m}$ 2DES in GaAs/AlGaAs heterostructure, see Table A.1.4</p>
	<p>NOT measured yet, WITH gate</p> <p>Hall bar $300\text{ }\mu\text{m} \times 100\text{ }\mu\text{m}$, contact distance $150\text{ }\mu\text{m}$ 2DES in GaAs/AlGaAs heterostructure, see Table A.1.4</p>

LiNbO_3 has a much larger electromechanical coupling coefficient, K^2 , than GaAs which will result in much larger acoustoelectric currents. Interdigitated transducers on LiNbO_3 were cooperatively prepared by Dr. Liang from THU/Beijing as shown in figure A.2.1. The crystal is 128° Y-X which gives K^2 of 5.6 and v of 3986 ms^{-1} . It is planned to transfer graphene on top and pattern a Hall bar structure with metalize contacts between the IDTs.

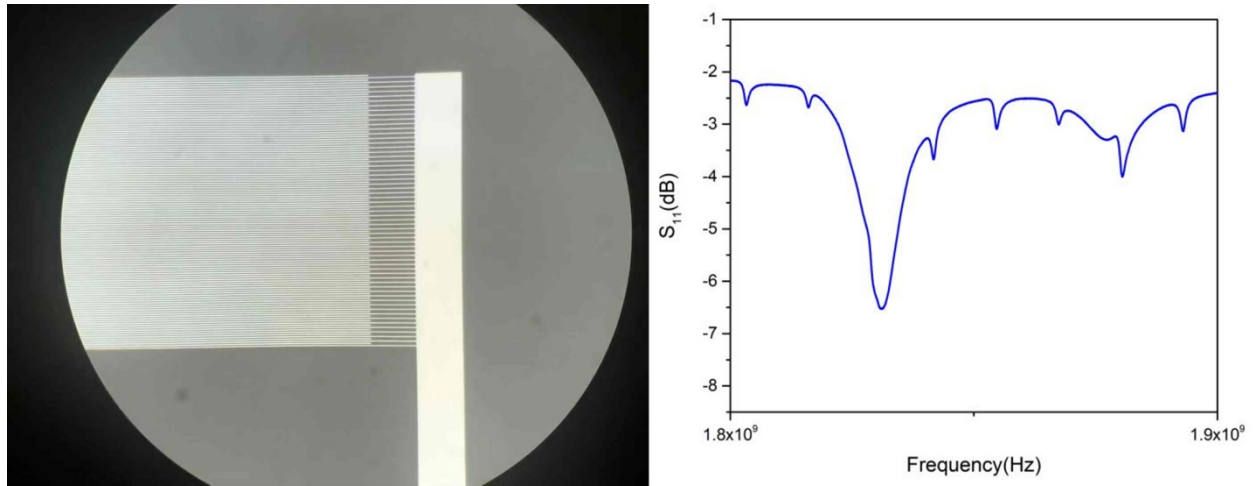


Figure A.2.1 IDTs on LiNbO_3 substrate from Dr. Liang in Tsinghua University. The finger width is 500 nm giving pitch of $2 \mu\text{m}$ and resonance at around 1.8 GHz for the first harmonic as measured on the right-hand.

Appendix B

Sample Preparation and Process Parameters

B.1 Preparation of GaAs 2DES Hall Bar

Table B.1.1 Ohmic contact fabrication

Step	Parameters	
Resist Preparation	Resist 1	LOR 5A
	Spin Speed	6000 rpm
	Acceleration	10, 000 rpm/s
	Time	60 s
	Bake	160 °C, 1 min
	Resist 2	S1805
	Spin Speed	6000 rpm
	Acceleration	10, 000 rpm/s
	Time	60 s
	Bake	115 °C, 1 min
Exposure of Contacts	Exposure Time	2.2 s
	Intensity	13 mW/cm ²
	Wavelength	365 nm
Development of Contacts	Developer	MF319
	Time	45 s
Deposition of Contacts	Method	Physical Vapor Deposition
	Pressure	10 ⁻⁷ mbar
	Materials 1	Germanium, 40 nm
	Materials 2	Gold, 100 nm
Lift Off	Remover 1	Acetone, 5 hours
	Remover 2	1165, 1 hour
	Assistant Treatment	Ultrasound, less than 20 s
Annealing	Temperature	430 °C
	Time	300 s
	Environment	Ar/H ₂ forming gas
Cleaning	Solvents	Acetone/Isopropanol and N ₂ drying
	Assistant Treatment	Ultrasound

Table B.1.2 Gate fabrication

Step	Parameters	
Resist Preparation	Refer to Table B.1.1	
Exposure of Contacts		
Development of Contacts		
Deposition of Contacts	Method	Physical Vapor Deposition
	Pressure	10^{-7} mbar
	Materials 1	Titanium, 10 nm
	Materials 2	Gold, 100 nm
Lift Off	Refer to Table B.1.1	
Cleaning	Solvents	Acetone/Isopropanol and N ₂ drying
	Assistant Treatment	Ultrasound

Table B.1.3 Hall bar fabrication

Step	Parameters	
Resist Preparation	Resist	ma-N1405
	Spin Speed	6000 rpm
	Acceleration	10, 000 rpm/s
	Time	60 s
	Bake	100 °C, 1 min
Exposure of Hall bar	Exposure Time	24.5 s
	Intensity	13 mW/cm ²
	Wavelength	365 nm
Development of Hall bar	Developer	ma-D 533/S
	Time	45 s
Etching of Hall bar	Etchant	H ₃ PO ₄ /H ₂ O ₂ /H ₂ O (10/20/400 mL)
	Time	300 to 600 s
Cleaning	Solvents	Acetone/Isopropanol and N ₂ drying
	Assistant Treatment	Ultrasound

Table B.1.4 IDT electrode fabrication

Step	Parameters	
Resist Preparation	Resist 1	PMMA 600K (669.07)
	Spin Speed	6000 rpm
	Acceleration	10, 000 rpm/s
	Time	60 s
	Bake	150 °C, 3 min
	Resist 2	PMMA 950K (679.04)
	Spin Speed	6000 rpm
	Acceleration	10, 000 rpm/s
	Time	60 s
	Bake	150 °C, 3 min
Exposure of Contacts	Method	Electron beam lithography with 3-point alignment
	Dose	90 – 100 $\mu\text{C}/\text{cm}^2$
	Writing Field	1000 μm
	Aperture	30 μm
Development of Contacts	Developer	AR 600-55
	Time	1 min
	Stopping	Isopropanol, 30 s/ DI water, 30 s
Deposition of Contacts	Refer to Table B.1.2	
Lift off	Remover 1	AR 300-76
	Assistant Treatment	Ultrasound, less than 20 s
Cleaning	Solvents	Acetone/Isopropanol and N_2 drying
	Assistant Treatment	Ultrasound

The fabrication steps for releasing a structure with hydrofluoric acid is similar to the steps in Table B.1.1, however, here I only use photoresist S1805. HF acid concentration of 5% and 40% were tested. The etching time depends on the release size, ranging from tens of minutes to several hours.

B.2 Preparation of Graphene Hall Bar

Table B.2.1 Preparation of Monolayer Graphene

Step	Parameters	
Protecting Resist Preparation	Resist	PMMA 950K, graphene side for protection
	Spin Speed	6000 rpm
	Acceleration	10, 000 rpm/s
	Time	60 s
	Bake	Room temperature for 1 day
	Dicing	4 × 4 mm ²
Copper Removing	Etchant	Fe(NO ₃) ₃ , 0.05gmL ⁻¹
	Time	One night
	Etchant Dilution	3 times DI water wet transferring, at least 20 minutes waiting for each time
Inorganic Contaminates Cleaning	Solvents	HCl/H ₂ O ₂ /H ₂ O (5/5/100mL)
	Solvents Dilution	3 times DI water wet transferring, at least 20 minutes waiting for each time
Organic Contaminates Cleaning	Solvents	NH ₄ OH/H ₂ O ₂ /H ₂ O (1/1/100mL)
	Solvents Dilution	3 times DI water wet transferring, at least 20 minutes waiting for each time

Table B.2.2 Preparation of graphene Hall bar on GaAs

Step	Parameters	
GaAs Substrate Preparation	Dicing	$6 \times 6 \text{ mm}^2$
	Surface Hydrophilic	O ₂ Plasma, 300 W, 300 s
Graphene Transfer	Method	Van der Waals Bonding
	Bake	150 °C, 900 s
PMMA Removing	Remover	Acetone, more than 1800 s
	Solvent	Acetone/Isopropanol and N ₂ drying
Resist Preparation	Refer to Table B.1.3	
Exposure of Hall Bar		
Development of Hall Bar		
Etching of Hall Bar	Etching	O ₂ Plasma, 300 W, 300 s
	Solvent	Acetone/Isopropanol and N ₂ drying
Resist Preparation	Refer to Table B.1.1	
Exposure of Contacts		
Development of Contacts		
Deposition of Contacts	Refer to Table B.1.2, but without ultrasound assistance	
Lift off		
Cleaning		

To produce interdigitated transducers on graphene Hall bar samples, the same steps as in table B.1.4. are used. After finishing a graphene Hall bar sample, I firstly bake the sample in Rapid Thermal Annealing at 130°C for one night. A second bake-out of the sample follows in the MTI Corporate OTF 1200-X Instruments at 130 °C for 48 hours after mounting in the probe. Both annealing processes are performed under vacuum.

Bibliography

- [A.BER1990] A. Berg, M. Dobers, R. R. Gerhardts, and K. v. Klitzing, Magnetoquantum oscillations of a nuclear spin lattice relaxation near a two dimensional electron gas, *Phys. Rev. Lett.* 64, 2563 (1990).
- [A.CLE2002] A. N. Cleland, J. S. Aldridge, D. C. Driscoll and A. C. Gossard, Nanomechanical displacement sensing using a quantum point contact, *Appl. Phys. Lett.* 81, 1699 (2002).
- [A.HUT1962] A. R. Hutson, D. L. White, Elastic wave propagation in piezoelectric semiconductors, *J. Appl. Phys.* 33, 40 (1962).
- [A.NET2009] A. H. Castro Neto, F Guinea, N. M. R. Peres, K. S. Novoselov and A. K. Geim, The electronic properties of graphene, *Rev. Mod. Phys.* 81, 109 (2009)
- [A.OWE2004] Alan Owens and A. Peacock, Compound semiconductor radiation detectors, *Nucl. Instrum. Methods Phys. Res. A* 531, 18 (2004).
- [A.POG2012] A. G. Pogosov, M. V. Budantsev, E. Yu. Zhdanov, D. A. Pokhabov, A. K. Bakarov and A. I. Toropov, Electron transport in suspended semiconductor structures with two dimensional gas, *Appl. Phys. Lett.* 100, 181902 (2012).
- [A.WIX1986] A. Wixforth, J. P. Kotthaus and G. Weimann, Quantum oscillations in the surface acoustic wave attenuation caused by a two dimensional electron system, *Phys. Rev. Lett.* 56, 2104 (1985).
- [A.WIX1989] A. Wixforth, J. Scriba, M. Wassermeier, J. P. Kotthaus, G. Weimann and W. Schlapp, Surface acoustic waves on GaAs/Al_xGa_{1-x}As heterostructures, *Phys. Rev. B* 40, 7874 (1989).
- [ALLRESIST] https://www.allresist.com/wp-content/uploads/sites/2/2015/12/allresist_produkinfos_ar-p630-670_englisch.pdf
- [B.FRI2014] Benedikt Frieß, Spin and charge ordering in the quantum Hall regime, PhD thesis, *Max Planck Institute for Solid State Research, Stuttgart* (2014).

- [C.CAM1989] Colin Campbell, *Surface acoustic wave devices and their signal processing applications*, Academic Press, Inc. (1989).
- [C.CO2005] Claude Cohen-Tannoudji, Bernard Diu and Franck Laloe, *Quantum mechanics, Vol. I*, John Wiley & Sons (2005).
- [C.ENS2005] Christian Enss and Siegfried Hunklinger, *Low temperature physics*, Springer (2005).
- [C.WEI1977] Claude Weisbuch and Claudine Hermann, Optical detection of conduction electron spin resonance in GaAs, $\text{Ga}_{1-x}\text{In}_x\text{As}$, and $\text{Ga}_{1-x}\text{Al}_x\text{As}$, *Phys. Rev. B* 15, 816 (1977).
- [D.BOU2008] D. W. Boukhvalov, M. I. Katsnelson and A. I. Lichtenstein, Hydrogen on graphene: electronic structure, total energy, structure distortions and magnetism from first principles calculations, *Phys. Rev. B* 77, 035427 (2008).
- [D.CHK1992] D. B. Chklovskii, B. I. Shklovskii and L. I. Glazman, Electrostatics of edge channels, *Phys. Rev. B* 46, 4026 (1992).
- [D.CHK1993] D. B. Chklovskii, K. A. Matveev and B. I. Shklovskii, Ballistic conductance of interacting electrons in the quantum Hall regime, *Phys. Rev. B* 47, 12605 (1993).
- [D.KRE2011] Dustin J. Kreft and Robert H. Blick, Surface acoustic waves and nanoelectromechanical systems, in *Acoustic Waves from Microdevices to Helioseismology*, InTech (2011)
- [D.KRE2012T] Dustin J. Kreft, Acoustoelectric current in suspended quantum point contacts, *PhD thesis, University of Wisconsin-Madison* (2012).
- [D.LID2008] D. R. Lide, *Handbook of chemistry and physics* (CRC Press/Taylor & Francis Group, Boca Raton, 2008)
- [D.PAG1977] D. Paget, G. Lampel, B. Sapoval and V. I. Safarov, Low field electron-nuclear spin coupling in gallium arsenide under optical pumping conditions, *Phys. Rev. B* 15, 5780 (1977).
- [D.PAG1982] Daniel Paget, Optical detection of NMR in high purity GaAs direct study of the relaxation of nuclei close to shallow donors, *Phys. Rev. B* 25, 4444 (1982).
- [D.STE1983] D. Stein, K. v. Klitzing and G. Weimann, Electron spin resonance on GaAs- $\text{Al}_x\text{Ga}_{1-x}\text{As}$ heterostructures, *Phys. Rev. Lett.* 51, 130 (1983).

- [D.STE1984] D. Stein, G. Ebert, K. von Klitzing and G. Weimann, Photoconductivity on GaAs-Al_xGa_{1-x}As heterostructures, *Surf. Sci.* 142, 406 (1984).
- [DAN.RUSS] Daniel A. Russell, <https://www.acs.psu.edu/drussell/demos.html>
- [E.CHA2001] E. Y. Chang, Y.-L. Lai, Y. S. Lee, and S. H. Chen. A GaAs/AlAs wet selective etch process for the gate recess of GaAs power metal–semiconductor field-effect transistors. *J. Electrochem. Soc.* 148, G4 (2001).
- [E.HOE2002] E. M. Höhberger, R. H. Blick, F. W. Beil, W. Wescheider, M. Bichler and J. P. Kotthaus, Magnetotransport in freely suspended two dimensional electron systems for integrated nanomechanical resonators, *Phys. E* 12, 487 (2002).
- [E.WEI2003T] Eva Maria Weig, Elektron Phonon Kavitäten Transportuntersuchungen an freitragenden Quantenpunkten, *PhD thesis, Ludwig Maximilians Universität München* (2003).
- [E.YAB1987] Eli Yablonovitch, T Gmitter, J. P. Harbison and R. Bhat, Extreme selectivity in the lift-off of epitaxial GaAs films, *Appl. Phys. Lett.* 51, 2222 (1987).
- [E.YAB1990] E. Yablonovitch, D. M. Hwang, T. J. Gmitter, L. T. Florez and J. P. Harbison, Van der Waals bonding of GaAs epitaxial liftoff films onto arbitrary substrates, *Appl. Phys. Lett.* 56, 2419 (1990).
- [F.BEI2008] Florian W. Beil, Achim Wixforth, Werner Wegscheider, Dieter Schuh, Max Bichler and Robert H. Blick, Shock waves in nanomechanical resonantors, *Phys. Rev. Lett.* 100, 026801 (2008).
- [G.BAU2014] G. J. Bauhuis, P. Mulder and J. J. Schermer, Thin film III-V solar cells using epitaxial lift off, in *High efficiency solar cells*, Springer, pp 623 (2014).
- [G.FAR1978] G. W. Farnell, Types and properties of surface waves, in *Topics in applied physics: acoustic surface waves*, Springer (Berlin), pp. 13 (1978).
- [G.GIU2005] G. F. Giuliani and G. Vignale, *Quantum theory of the electron liquid*, Cambridge University Press (2005).
- [G.MATERIALS] <http://www.g-materials.de/products/photo-maskblanks/>
- [GRAPHEN] <https://www.graphenea.com/collections/graphene-products/products/monolayer-graphene-on-cu-4-inches>
- [GREGO.SNIDE] Gregory Snider, <https://www3.nd.edu/~gsnider/>
- [H.STO1999] Horst L. Stormer, Nobel lecture: the fractional quantum Hall effect, *Rev. Mod. Phys.* 71, 875 (1999).
- [HEIDELBERG] <https://www.himt.de/index.php/dwl66.html>

- [IEEE2007] IEEE Standard for precision coaxial connectors (DC to 110 GHz), *IEEE Instrumentation and Measurement Society*, IEEE Std 287TM-2007 (Revision of IEEE Std 287-1968).
- [J.CHA2012] J. Chaste, A. Eichler, J. Moser, G. Ceballos, R. Rurali and A. Bachtold, A nanomechanical mass sensor with yoctogram resolution, *Nat. Nanotechnol.* 7, 301 (2012).
- [J.DAV1998] John H. Davis, *The physics of low dimensional semiconductors: an introduction*, Cambridge University Press (1998).
- [J.GOE2004T] J. Göres, Correlation effects in 2-dimensional electron systems composite fermions and electron liquid crystals, *PhD thesis, Max-planck Institute for solid state Research, Stuttgart* (2004).
- [J.HEI1984] J. Heil, I. Kouroudis, B. Lüthi and P. Thalmeier, Surface acoustic waves in metals, *J. Phys. C: Solid State Phys.* 17, 2433 (1984).
- [J.KIM1994] Ju H. Kim, I. D. Vagner and L. Xing, Phonon assisted mechanism for quantum nuclear spin relaxation, *Phys. Rev. B* 49, 16777 (1994).
- [J.RIE2019] Jan Leonard Riemann, Influence of symmetry breaking through mechanical deformation on the transport properties of 2D systems, *Master thesis, University Hamburg, Hamburg* (2019).
- [J.SCH2005] J. J. Schermer, P. Mulder, G. J. Bauhuis, M. M. A. J. Voncken, J. Van Deelen, E. Haverkamp, and P. K. Larsen, Epitaxial lift off for large area thin film III-V devices, *Phys. Stat. Sol. (a)* 202, 501 (2005).
- [J.SHI1995] J. M. Shilton, D. R. Mace, V. I. Talyanskii, M. Pepper, M. Y. Simmons, A. C. Churchill and D. A. Ritchie, Effect of spatial dispersion on acoustoelectric current in a high mobility two dimensional electron gas, *Phys. Rev. B* 51, 14770 (1995).
- [J.SHI1996] J. M. Shilton, V. I. Talyanskii, M. Pepper, D. A. Ritchie, J. E. F. Frost, C. J. B. Ford, C. G. Smith and G. A. C. Jones, High frequency single electron transport in a quasi one dimensional GaAs channel induced by surface acoustic waves, *J. Phys. Condens. Matter* 8, L531 (1996).

- [J.SHIL1995] J. M. Shilton, D. R. Mace, V. I. Talyanskii, M. Y. Simmons, M. Pepper, A. C. Churchill and D. A. Ritchie, Experimental study of the acoustoelectric effects in GaAs-AlGaAs heterostructures, *J. Phys.: Condens. Matter* 7, 7675 (1995).
- [J.SIC2015] Jonas Sichau, Mechanically modulated graphene for THz nanoelectronics, *Master thesis, University Hamburg, Hamburg* (2015).
- [J.SIC2019] J. Sichau, M. Prada, T. Anlauf, T. J. Lyon, B. Bosnjak, L. Tiemann and R. H. Blick, Resonance microwave measurements of an intrinsic spin-orbit coupling gap in graphene: a possible indication of a topological state, *Phys. Rev. Lett.* 122, 046403 (2019).
- [K.EKI2004] K. L. Ekinici, X. M. Huang and M. L. Roukes, Ultrasensitive nanoelectromechanical mass detection, *Appl. Phys. Lett.* 84, 4469 (2004).
- [K.HAS2005] Katsushi Hashimoto, Koji Muraki, Norio Kumada, Tadashi Saku and Yoshiro Hirayama, Effects of inversion asymmetry on electron nuclear spin coupling in semiconductor heterostructures: possible role of spin orbit interactions, *Phys. Rev. Lett.* 94, 146601 (2005).
- [K.KLI1980] K. v. Klitzing, G. Dorda and M. Pepper, New method for high accuracy determination of the fine-structure constant based on quantized Hall resistance, *Phys. Rev. Lett.* 45, 494 (1980).
- [K.KLI1986] Klaus von Klitzing, The quantized Hall effect, *Rev. Mod. Phys.* 58, 519 (1986).
- [K.LABY] http://www.kayelaby.npl.co.uk/chemistry/3_8/3_8_1.html
- [K.LIE1994] Karlheinz Lier and Rolf R. Gerhardts, Self consistent calculations of edge channels in laterally confined two dimensional electron systems, *Phys. Rev. B* 50, 7757 (1994).
- [K.NOV2004] K. S. Novoselov, A. K. Geim, S. V. Morozov, D. Jiang, Y. Zhang, S. V. Dubonos, I. V. Grigorieva and A. A. Firsov, Electric field effect in atomically thin carbon films, *Science* 306, 666 (2004).
- [K.NOV2005] K. S. Novoselov, A. K. Geim, S. V. Morozov, D. Jiang, M. I. Katsnelson, I. V. Grigorieva, S. V. Dubonos and A. Firsov, Two dimensional gas of massless Dirac fermions in graphene, *Nature* 438, 197 (2005).
- [K.PET2011] K. Peters, A. Tittel, N. Gayer, A. Graf, V. Paulava, U. Wurstbauer and W. Hansen, Enhancing the visibility of graphene on GaAs, *Appl. Phys. Lett.* 99, 191912 (2011).

- [L.RAY1885] Lord Rayleigh, J. W. S., On waves propagated along the plane surface of an elastic solid, *Proceedings fo the London Mathematical Society*, s1-17, 4 (1885). https://en.wikipedia.org/wiki/Rayleigh_wave
- [L.SON2010] L. Song, S. W. Chen, J. H. He, C. Y. Zhang, C. Lu and J. Cao, The anomalous negative acoustoelectric current in single electron transport devices, *Solid State Commun.* 150, 292 (2010).
- [L.TIE2008] Lars Tiemann, Phase coherence in the regime of bilayer exciton condensation, *PhD thesis, Max-planck Institute for solid state Research, Stuttgart* (2008).
- [L.VEG1921] L.Vegard, Die Konstitution der Mischkristalle und die Baumfüllung der Atome, *Z. Phys.* 5, 17 (1921).

https://en.wikipedia.org/wiki/Vegard%27s_law
- [M.AST2008] Michael Robert Astley, Surface acoustic wave defined dynamic quantum dots, *PhD thesis, University of Cambridge* (2008).
- [M.BUE1988] M. Buettiker, Absence of backscattering in the quantum Hall effect in multiprobe conductors, *Phys. Rev. B* 38, 9375 (1988).
- [M.CAG1985] Marvin E. Cage, Ronald F. Dziuba and Bruce F. Field, A test of the quantum Hall effect as a resistance standard, *IEEE Trans. On Instrum. Meas.* IM-34, 301 (1985).
- [M.DOB1988] M. Dobers, K. v. Klitzing and G. Weimann, Electron-spin resonance in the two dimensional electron gas of GaAs-Al_xGa_{1-x}As heterostructures, *Phys. Rev. B* 38, 5453 (1988).
- [M.DOBE1988] M. Dobers, K. v. Klitzing, J. Schneider, G. Weimann and K. Ploog, Electrical detection of nuclear magnetic resonance in GaAs-Al_xGa_{1-x}As heterostructures, *Phys. Rev. Lett.* 61, 1650 (1988).
- [M.HAN2012] M. S. Hanay, S. Kelber, A. K. Naik, D. Chi, S. Hentz, E. C. Bullard, E. Colinet, L. Duraffourg and M. L. Roukes, Single protein nanomechanical mass spectrometry in real time, *Nat. Nanotechnol.* 7, 602 (2012).
- [M.KEL1995] M. J. Kelly, *Low-dimensional semiconductors, materials, physics, thechnology, devices*, Clarendon Press Oxford (1995).
- [M.RAITH] <https://m.raith.com/products/elphy-plus.html>

- [M.RIE1999] Matthias Rief, Hauke Clausen Schumann and Hermann E. Gaub, Sequence dependent mechanics of single DNA molecules, *Nat. Struct. Biol.* 6, 346 (1999).
- [M.SCH2016] Martin J. A. Schütz, Quantum dots for quantum information processing: controlling and exploiting the quantum dot environment, *PhD thesis, Ludwig-Maximilian University, München* (2016).
- [M.VON2004] M. M. A. J. Voncken, J. J. Schermer, G. J. Bauhuis, P. Mulder and P. K. Larsen, Multiple release layer study of the intrinsic lateral etch rate of the epitaxial lift off process, *Appl. Phys. A* 79, 1801 (2004).
- [MICRO.CHEM] <http://microchem.com/pdf/PMGI-Resists-data-sheetV-rhcredit-102206.pdf>
- [N.GAYE2018T] Nils Gayer, Magnetotransport und Thermoelektrik in zylindrischen GaAs-Halbleiterstrukturen, *PhD thesis, University Hamburg, Hamburg* (2018).
- [O.INS2005] Superconducting magnet system, operator's handbook, *Oxford Instruments* (2005).
- [P.DRU1900I] P. Drude, Zur Elektronentheorie der Metalle (I.), *Ann. Phys.* 306, 566 (1900).
- [P.DRU1900II] P. Drude, Zur Elektronentheorie der Metalle (II.), *Ann. Phys.* 306, 566 (1900).
- [P.THA2010] Peter Thalmeier, Balazs Dora and Klaus Ziegler, Surface acoustic wave propagation in graphene, *Phys. Rev. B* 81, 041409 (2010).
- [P.WAL1947] P. R. Wallace, The band theory of graphite, *Phys. Rev.* 71, 622 (1947).
- [PFEIFFER] <https://www.pfeiffer-vacuum.com/en/know-how/introduction-to-vacuum-technology/fundamentals/types-of-flow/>
- [R.BLI2000] R. H. Blick, F. G. Monzon, W. Wegscheider, M. Bichler, F. Stern and M. L. Roukes, Magnetotransport measurements on freely suspended two dimensional electron gases, *Phys. Rev. B* 62, 17103 (2000).
- [R.COT1997] R. Cote, A. H. MacDonald, Luis Brey, H. A. Fertig, S. M. Girvin and H. T. C. Stoof, Collective excitations, NMR, and phase transitions in skyrme crystals, *Phys. Rev. Lett.* 78, 4825 (1997).
- [R.DEN2016] Richard Dengler, Self inductance of a wire loop as a curve integral, *Adv. Electromagn.* 5, 1 (2016).
- [R.JAF1945] R. I. Jaffee, E. M. Smith, and B. W. Gonser, The constitution of gold-Germanium, *Trans. Met. Soc. AIME*, 161, 366 (1945).

- [R.LAN1987] R. Landauer, Electrical transport in open and closed systems, *Z. Phys. B* 68, 217 (1987).
- [R.LAU1982] R. B. Laughlin, Impurities and edges in the quantum Hall effect, *Surf. Sci.* 113, 22 (1982).
- [R.MCN2011] R. P. G. McNeil, M. Kataoka, C. J. B. Ford, C. H. W. Barnes, D. Anderson, G. A. C. Jones, I. Farrer and D. A. Ritchie, On demand single electron transfer between distant quantum dots, *Nature* 477, 439 (2011).
- [R.MEI2005] Ronald Meisels, Electron spin resonance and related phenomena of low dimensional electronic systems in III-V compounds, *Semicond. Sci. Technology*. 20, R1 (2005).
- [R.NAI2008] Rahul Raveendran Nair, Peter Blake, Alexander N. Grigorenko, Konstantin S. Novoselov, Tim J. Booth, Tobias Stauber, Nuno M.R. Peres, and Andre K. Geim. Fine structure constant defines visual transparency of graphene. *Science*, 320, 1308–1308 (2008).
- [R.WHI1965] R. M. White and F. W. Voltmer, Direct piezoelectric coupling to surface elastic waves, *Appl. Phys. Lett.* 7, 314 (1965).
- [R.WIL1993] R. L. Willett, R. R. Ruel, M. A. Paalanen, K. W. West and L. N. Pfeiffer, Enhanced finite wave vector conductivity at multiple even denominator filling factors in two dimensional electron systems, *Phys. Rev. B* 12, 7344 (1993).
- [R.WIL1994] R. L. Willett, Surface acoustic wave studies of electron correlations in the 2DES, *Surf. Sci.* 305, 76 (1994).
- [S.ADA1985] Sadao Adachi, GaAs, AlAs and $\text{Al}_x\text{Ga}_{1-x}\text{As}$: materials parameters for use in research and device applications, *J. Appl. Phys.* 58, R1 (1985).
- [S.DAT1995] S. Datta, *Electronic transport in mesoscopic systems*, Cambridge University Press (1995).
- [S.ILA2004] S. Ilani, J. Martin, E. Teitelbaum, J. H. Smet, D. Mahalu, V. Umansky and A. Yacoby, The microscopic nature of localization in the quantum Hall effect, *Nature* 427, 328 (2004).
- [SÜSS] <https://www.suss.com/en/products-solutions/mask-aligner/mjb4>

- [S.WIE2011] S. Wiemann, H. J. van Elferen, E. V. Kurganova, M. I. Katsnelson, A. J. M. Giesbers, A. Veligura, B. J. Van Wees, R. V. Gorbachev, K. S. Novoselov, J. C. Maan, and U. Zeitler, Coexistence of electron and hole transport in graphene, *Phys. Rev. B* 84, 115314 (2011).
- [T.GRU1981] T. W. Grudkowski and M. Gilden, Realization of temperature compensated GaAs surface acoustic wave delay lines, *Appl. Phys. Lett.* 38, 412 (1981).
- [T.LYO2017] T. J. Lyon, J. Sichau, A. Dorn, A. Centeno, A. Pesquera, A. Zurutuza, R. H. Blick, Probing electron spin resonance in monolayer graphene, *Phys. Rev. Lett.* 119, 066802 (2017)
- [T.LYO2017T] Timothy J. Lyon, An Investigation of the g-factor of graphene, *PhD thesis, University of Wisconsin-Madison* (2017).
- [T.LYON2017] Timothy J. Lyon, Jonas Sichau, August Dorn, Amaia Zurutuza, Amaia Pesquera, Alba Centeno, and Robert H. Blick, Upscaling high quality CVD graphene devices to 100 micron-scale and beyond, *Appl. Phys. Lett.* 110, 113502 (2017).
- [T.SMI1985] T. P. Smith, B. B. Goldberg, P. J. Stiles and M. Heiblum, Direct measurement of the density of states of a two dimensional electron gas, *Phys. Rev. B* 32, 2696 (1985).
- [V.MIS2012] V. Miseikis, J. E. Cunningham, K. Saeed, R. O'Rorke and A. G. Davies, Acoustically induced current flow in graphene, *Appl. Phys. Lett.* 100, 133105, (2012).
- [V.UMA2009] V. Umansky, M. Heiblum, Y. Levinson, J. Smet, J. Nübler and M. Dolev, MBE growth of ultra-low disorder 2DES with mobility exceeding $35 \times 10^6 \text{cm}^2/\text{Vs}$, *J. Cryst. Growth*, 311, 1658 (2009).
- [W.PAU1925] W. Pauli, Über den Zusammenhang des Abschlusses der Elektronengruppen im Atom mit der Komplexstruktur der Spektren, *Z. Phys.* 31, 765 (1925).
https://en.wikipedia.org/wiki/Pauli_exclusion_principle
- [WIKI.AM] https://en.wikipedia.org/wiki/Amplitude_modulation
- [X.LEE1997] X. Y. Lee, Mark Goertemiller, Misha Boroditsky, Regina Ragan and Eli Yablonovitch, Thin film GaAs solar cells on glass substrates by epitaxial liftoff, *Appl. Phys. Lett.* 394, 719 (1997).

- [X.LIA2011] Xuelei Liang, Brent A. Sperling, Irene Calizo, Guangjun Cheng, Christina Ann Hacker, Qin Zhang, Yaw Obeng, Kai Yan, Hailin Peng, Qiliang Li, Xiaoxiao Zhu, Hu Yuan, Angela R. Hight Walker, Zhongfan Liu, Lian-mao Peng, and Curt A. Richter. Toward clean and crackless transfer of graphene. *ACS Nano*. 5, 9144–9153 (2011).
- [X.WU1985] X. S. Wu, L. A. Coldren and J. L. Merz, Selective etching characteristics of HF for $\text{Al}_x\text{Ga}_{1-x}\text{As}$, *Electron. Lett.* 21, 558 (1985).
- [Y.LI2008] Y. Q. Li and J. H. Smet, Nuclear-electron spin interactions in quantum Hall regime, in *Spin Physics in Semiconductors*, Springer (Berlin), pp. 347 (2008).
- [Z.YA2012S] Zheng Yan, Jian Lin, Zhiwei Peng, Zhengong Sun, Yu Zhu, Lei Li, Changsheng Xiang, E. Loic Samuel, Carter Kittrell and James M. Tour, Toward the synthesis of wafer scale single crystal graphene on copper foils—supporting information, *ACS Nano* 6, 9110 (2012).
- [Z.YAN2012] Zheng Yan, Jian Lin, Zhiwei Peng, Zhengong Sun, Yu Zhu, Lei Li, Changsheng Xiang, E. Loic Samuel, Carter Kittrell and James M. Tour, Toward the synthesis of wafer scale single crystal graphene on copper foils, *ACS Nano*. 6, 9110 (2012).

Publication

- [1] P. Zhao, L. Tiemann, H. K. Trieu and R. H. Blick, Acoustoelectric current investigation on magnetotransport in graphene, *in preparation*.
- [2] L. G. Mourokh, P. Ivanushkin, D. J. Kreft, H. Shin, M. Bichler, W. Wegscheider, P. Zhao, L. Tiemann and R. H. Blick, Effects of electron confinement on the acoustoelectric current in suspended quantum point contacts, *Appl. Phys. Lett.* 110, 223102 (2017).

Acknowledgement

In retrospect to the last several years in my PhD research, I have to acknowledge many people without whom I would hardly get my things done, and I feel really lucky to have been working with them and appreciate their contribution on my experience in Germany.

- Prof. Robert H. Blick for providing me the opportunity to work on a very frontier and challenging project and helping me go through many hard difficulties by guiding and advising me with his wisdom.
- Prof. Hoc. Khiem Trieu for accepting me as a PhD student and always provide insightful ideas on my progress and problems.
- Prof. Matthias Kuhl for organizing my PhD defense as chairman of my doctoral defense committee.
- Dr. Lars Tiemann, with whom I am able to achieve what I have written in the whole thesis. The help I have been getting from Lars is not only on my work in lab, but also on my questions in my life experience in Germany. Working with Lars is also one of the main reasons that I make the determination to start my career in science for some years after finishing my PhD.
- Dr. Jonas Sichau and Bojan Bosnjak for their help on my thesis writing and my experiments in cleaning room and electron-beam lithography, and my contact with liquid helium and cryostat for the first time in my life.
- The group (former) members of my supervisors, Irene, Paul, Andreas, Stefanie, Timothy, Jens, Timo etc., for their helping on my work in lab, for instance, FIB cutting, HF (Hydrofluoric acid) etching, GaAs membrane making, and discussion on my experiments and advice on my thesis.
- Administer and technicians of the group, Katja, Thomas, Matthias, Andrea, Christina, Michael for their support on my paperwork of visa and university, and trainings on the machines in the lab.
- My flatmates, Leo and Pepe (Leo's son, three and half years old), for the joys they bring me at home.

- My lifetime friends back in China for their always keeping in touch with me, which is one of the reasons that I am not homesick for the time being.
-and my family for their infinitely supporting, as always.